Accuracy and Reliability Improvement of Wide-Area Power Grid Monitoring

A Dissertation Presented for the

Doctor of Philosophy

Degree

The University of Tennessee, Knoxville

Lingwei Zhan

August 2015

ACKNOWLEDGEMENTS

I would like to express my deepest gratitude to my advisor, Dr. Yilu Liu for her patient guidance and constant encouragement in my research and personal life throughout the past four years in United States. I would also like to thank Dr. Hairong Qi, Dr. Wei Gao, and Dr. Chien-fei Chen for serving on my committee. I appreciate their suggestions and comments on my research projects.

Then, many thanks to all those graduated and current Power IT Laboratory colleagues, for their consistent friendships and valuable suggestions. I am greatly appreciative of the help and friendship from Dr. Yong Liu, Dr. Ye Zhang, Gefei Kou, Jiahui Guo, Yin Lei, Dao Zhou, Jidong Chai, Wenxuan Yao, Jiecheng Zhao, Haoyang Lu, Hesen Liu, Jerel Culliss, and Hao Liu. I could not have the memorable time during the past four years in Knoxville without your friendship.

I also would like to thank Dr. Shengyou Gao from Tsinghua University, Dr. Jianyang Zhao from Huaiyin Institute of Technology, Allen Goldstein and Gerard Stenbakken from National Institute of Standards and Technology, Erik Johannessen from UrsaNav, Inc., Joe Campione from Southern Marketing Associates Inc., Mike Geggatt from Symmetricom, and Gordon Hoops from Candura Instruments. I could not finish the research without your help.

Last but not least I would like to express my deepest love to my family: my father Yingke Zhan, my mother Baoli Shi, and my fiancée Dan Su, for their endless love and support.

How time flies! I will cherish the four years life in the University of Tennessee as one of my best memories.

ABSTRACT

Phasor Measurement Unit (PMU) is one of the key elements of wide area measurement systems (WAMS) in advanced power system monitoring, protection, and control applications. Frequency Disturbance Recorder (FDR) developed by the Power IT Laboratory at the University of Tennessee, is a low-cost and single-phase PMU used at the distribution level.

Traditional PMUs use GPS as the only timing source. They will stop working when GPS signal is lost or unstable. Two alternative GPS independent timing sources including eLoran and Chip Scale Atomic Clock were tested for long-term reliability and short-term accuracy to study the application of the two methods in synchrophasor measurement area.

Phasor measurement accuracy is of great concern for power grid researchers and operators. The hardware and software measurement algorithm of the FDRs were analyzed to study the error sources. The hardware of the FDRs was upgraded based on the analysis to improve measurement accuracy. Further, two different phasor measurement algorithms that are based on discrete Fourier Transform (DFT) and signal model will be introduced, respectively. The aim is to improve the phasor measurement accuracy under different steady-state and dynamic conditions as well as in a real power grid environment at the distribution level. Moreover, to better evaluate the measurement accuracy of PMUs, a PMU testing system was built. A calibration method that can compensate the time delay of the PMU testing system was proposed, and the testing results were compared to NIST to verify the accuracy of the PMU testing system after calibration.

At last, a concept of "Universal Grid Analyzer" (UGA) was proposed and a prototype was built. The UGA has improved phasor measurement accuracy thanks to the proposed adaptive high-accuracy synchronous sampling algorithm and high-precision ADC. Meanwhile, the UGA can also function as a synchronized power quality analyzer that has harmonics measurement, voltage sag and swell detection functions. Moreover, the noise analysis function of the UGA that can help the analysis of phasor measurement accuracy in a real power grid environment was developed.

TABLE OF CONTENTS

LIST OF TABLES

LIST OF FIGURES

Chapter 1 FNET System Architecture

1.1 Frequency Monitoring Network

Development of the synchronized phasor measurement technique originally began less than twenty years ago. Synchronized phasor measurement is one of the key elements of wide area measurement systems (WAMS) in advanced power system monitoring, protection, and control applications. Synchrophasor measurements can provide a unique capability to monitor system dynamics in wide area and in real-time, as well as the possibility of controlling and protecting the electric power system. GPS time-synchronized phasor measurements were introduced in the mid-1980's, and the first prototype Phasor Measurement Unit (PMU) was developed by a research team at Virginia Tech in 1988 [1]. As a member of the PMU family, the Frequency Monitoring Network (FNET) developed by the Power IT Laboratory at the University of Tennessee, Knoxville is a low-cost, GPS-synchronized wide-area power system voltage, angle and frequency measurement network [2]-[4]. As the synchronized single-phase measurement device of FNET, the Frequency Disturbance Recorder (FDR) uses one phase at the distribution level (120 V electrical outlets) to measure voltage amplitude, phase angle, and frequency. The measurement data are then transmitted via the Internet to the FNET servers. Thus far there are about 200 FDRs installed in the United States and about 50 FDRs installed worldwide. Figure 1.1 shows the map of FDRs location in North America, and Figure 1.2 shows the world map of FDRs [5].

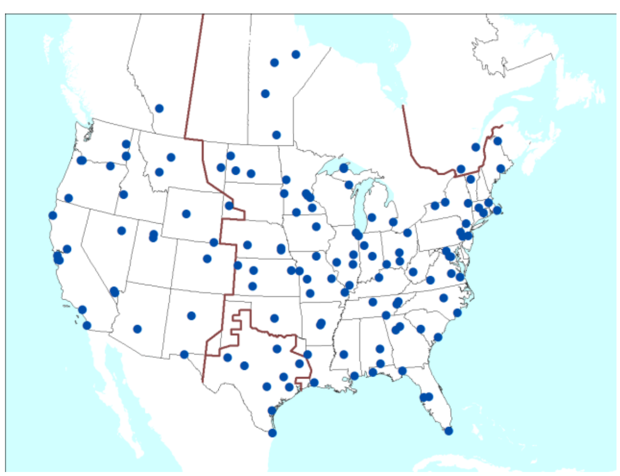

Figure 1.1 Map of FDRs location in North America

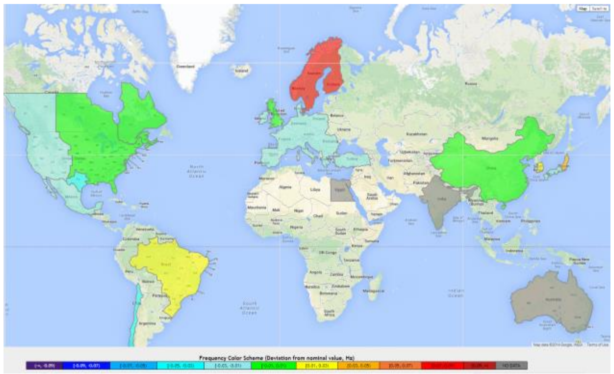

Figure 1.2 World map of FDRs

1.2 Frequency Disturbance Recorders

The first generation of FDRs was built in 2003 based on the work in [6], and FDRs are now in its second generation as shown in Figure 1.3. The FDR framework is shown in Figure 1.4. An FDR mainly consists of a current type voltage transducer, a low pass anti-aliasing filter, an analog to digital converter (ADC), a digital signal processor (DSP), a microcontroller unit (MCU), a GPS receiver, and a network module. The voltage transducer converts the input voltage signal to current signal, and then converts the current signal to a low voltage signal by an operational amplifier (op-amp). The low pass filter has 200 Hz cutoff frequency, and filters the high frequency noise and harmonics. The ADC is started by the pulse per second (PPS) signal from GPS receiver once at the beginning of every second. The ADC samples and converts the analog signal into a digital signal and transmits the digital signal to the DSP. The DSP is used to compute the magnitude, angle, and frequency of the input signal. Then the measurement data are transmitted to MCU, time stamped by GPS, and sent out to FNET servers through the Ethernet transceiver by TCP/IP protocol.

Timing synchronization of the measurement data is important for FDRs. A GPS receiver is used in FDRs to provide PPS to control the conversion of ADC at the beginning of every second and time stamp the measurement data. Generally the PPS error of the GPS receiver is less than 100 ns, which will cause less than 0.0022 degree angle error for 60Hz power grid, and 0.0018 degree angle error for 50Hz power grid.

The DSP of the FDR is the core of the device, and it is used to compute the magnitude, angle, and frequency of the input signal at the distribution level. Discrete Fourier Transform (DFT) is one of the common algorithms used in synchrophasor measurement area, and it is adopted as the basic framework of the FDR algorithm. The angle and frequency error of the FDRs is less than 0.02 degree and 0.0005Hz respectively under ideal 60Hz signal condition. In order to improve the phase angle and frequency measurement accuracy under off-nominal frequency conditions, Qps-DFT method proposed by Tao [7] is used to improve the phase angle measurement accuracy, and resampling method [6] is used to improve the frequency measurement accuracy.

Figure 1.3 Frequency Disturbance Recorder

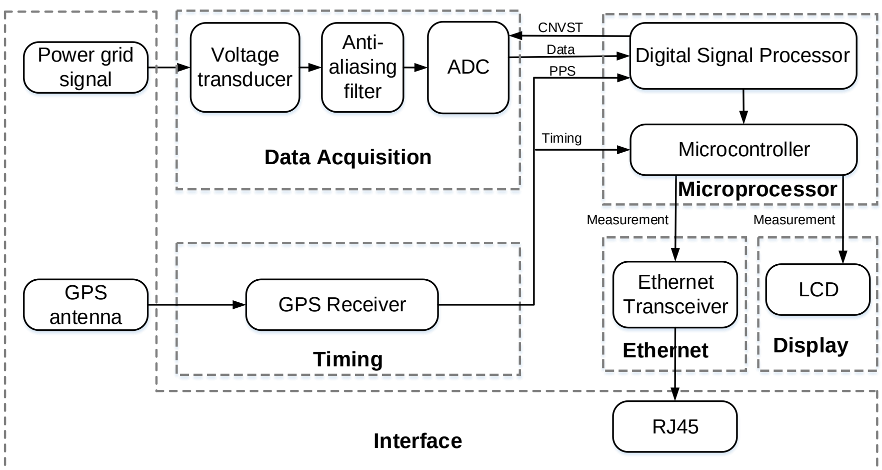

Figure 1.4 Framework of Frequency Disturbance Recorders

1.3 FNET applications

FNET group has developed several non-real-time and real-time applications [8]-[24]. The FNET system defines applications that use the data in the memory cache as real-time applications and those that use any other saved data in database as non-real-time applications. The FNET applications mainly include: Event trigger, Oscillation trigger, Event location detection, Oscillation modal analysis, Event visualization, Web service, and event alerts. The overall architecture of FNET data center is shown in Figure 1.5 [3].

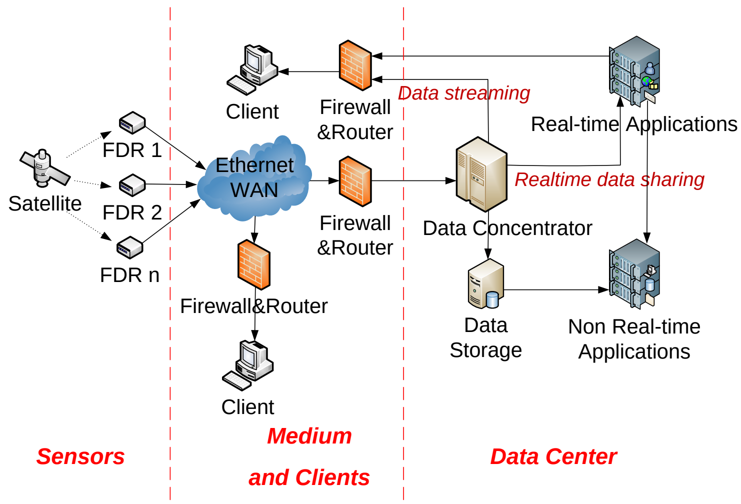

Figure 1.5 Architecture of FNET data center

Chapter 2 Alternative/Backup Timing Source for PMUs/FDRs

2.1 Background and motivation

Availability of global positioning system (GPS) provides the possibility of wide-area deployment of PMUs and FDRs in power system. The reliability of the measurement data is critical to PMU applications, but reliability of measurement data could be easily degraded by unavailability or instability of GPS signal. Since GPS is the only timing source for PMUs and FDRs so far, and they will stop working when GPS signal is lost or unstable. Therefore, it is necessary to study GPS alternative/backup timing source for PMUs and FDRs. Two timing sources including eLoran timing system and Chip Scale Atomic Clock (CSAC) were studied to verify the accuracy and reliability of the two alternative/backup timing sources.

2.2 eLoran timing system testing on FDRs

Working with our industry partner UrsaNav, Inc. that provides eLoran timing technology, we are able to demonstrate that eLoran timing technology can provide accurate and reliable timing for FDRs by integrating eLoran.

2.2.1 Introduction of eLoran timing system

The eLoran is an alternative high-power, low frequency, ground wave based system which can provide UTC timing and PPS [25]. The structure of eLoran system is shown in Figure 2.1. The core eLoran system consists of modernized control centers, transmitting stations, and monitoring sites, and some of the components in this system are shown in Figure 2.2. eLoran transmission is synchronized to the source of Coordinated Universal Time (UTC), wholly independent of Global Navigation Satellite System (GNSS). The UTC timing traceability of eLoran is less than 50ns that can comply with the timing accuracy requirement of IEEE PMU Standard C37.118.1-2011 [26] and C37.118.1a-2014 [27].

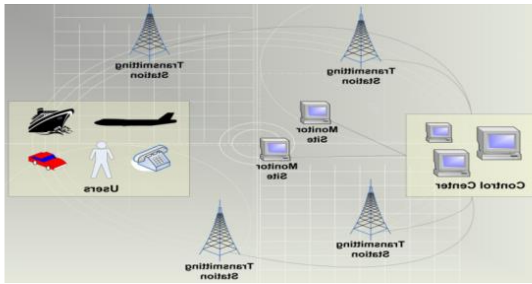

Figure 2.1 Structure of eLoran system

(a). Timing and control center

(b). Transmitter station

(c). Transmitter tower

(d). Antenna

Figure 2.2 Components of eLoran system

2.2.2 System setup

M12 Oncore GPS receiver module is used in the second generation of FDR (GenII-FDR). The interface between the M12 and the PCB board of FDR includes PPS signal and UTC time. In order to apply eLoran system in FDRs, M12 was removed from an FDR, and instead a UN-152A Ursa Mitigator manufactured by UrsaNav was connected to the PCB board of an FDR as the interface between eLoran system and the FDR. The UN-152A is a timing receiver that uses the latest version of UrsaNav's Mitigator™ series Low Frequency (LF) receivers. The UN-152A provides precise time, frequency, and data channel demodulation from Loran-C or eLoran systems. It features a serial port, a GPIO port and both 1PPS and 10MHz inputs and outputs [28].

Figure 2.3 UN-152A

2.2.3 Testing results

In order to assess the timing performance of eLoran system, two FDRs are used. Timing of one FDR is provided by GPS, called "GPS-FDR", and timing of another FDR is provided by eLoran system, called "eLoran-FDR". Figure 2.4 and Figure 2.5 show the system testing block and experimental setup, respectively. Since PPS accuracy is critical to synchronized measurement accuracy, the PPS performance of GPS and eLoran was evaluated during a three-day testing from Apr. 2nd to 4th, 2013. In this test, a Cesium clock that has very high stability to $1\text{x}10^{-7}$ parts per million (ppm) was used as the standard timing source for the comparison, and both PPS signals of GPS-FDR and eLoran-FDR were compared to PPS of the Cesium clock.

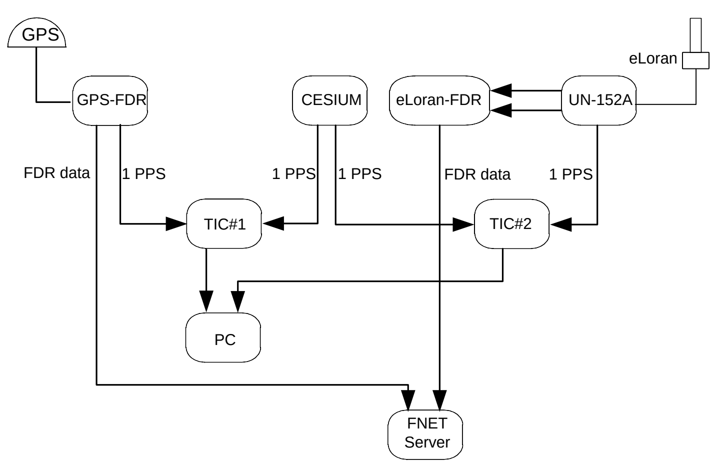

Figure 2.4 System testing block

Figure 2.5 Experimental setup

PPS errors measured by high-precision time interval counters (TIC) are shown in Figure 2.6 and Figure 2.7. Figure 2.6 shows the testing results during the first two days. Both PPS errors of M12 and UN-152A are less than 75ns, and both of them can comply with the PMU Standard. However, if we look into the timing stability of the two PPS errors in short time at second level, the timing stability of UN-152A is less than 10ns while the timing stability of M12 is about 50ns. Moreover, due to the instability of GPS and natural environments at 00:00 on Apr. 4^{th}, the maximum PPS error of M12 exceeds 1 us as shown in Figure 2.7 (a). In fact, the GPS signal was lost during this time. In contrast, Figure 2.7 (b) shows that the timing of eLoran was not affected during the same time period since eLoran is a GPS independent method. At last, it should be noted that eLoran is a ground-based technology, human activity and natural environments could affect the PPS accuracy. According to Figure 2.6 (b) and Figure 2.7 (b) it can be observed that the period of the PPS errors of eLoran is about one day, where it shows some room for improvement.

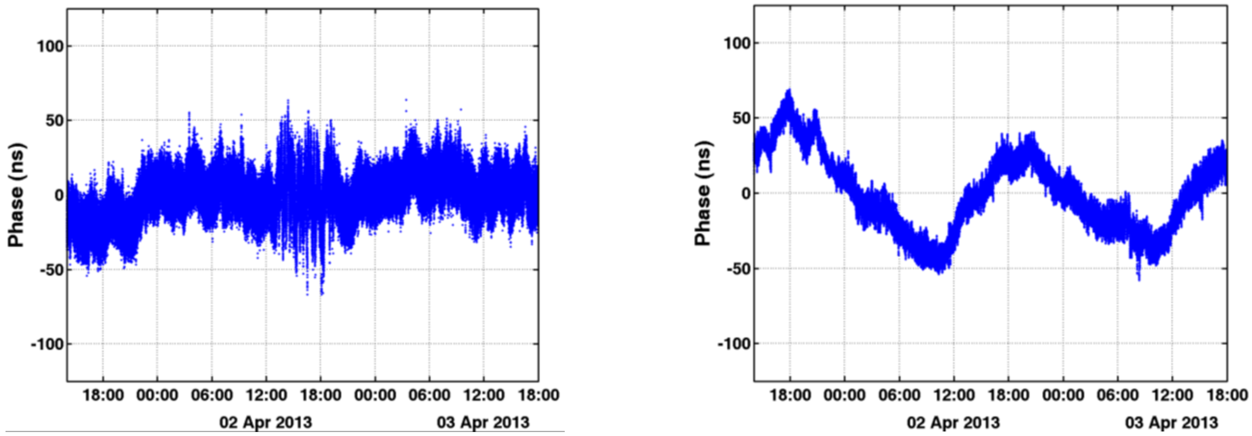

(a). PPS error of M12 (b). PPS error of eLoran UN-152A

Figure 2.6 PPS errors of M12 and eLoran UN-152A in two days

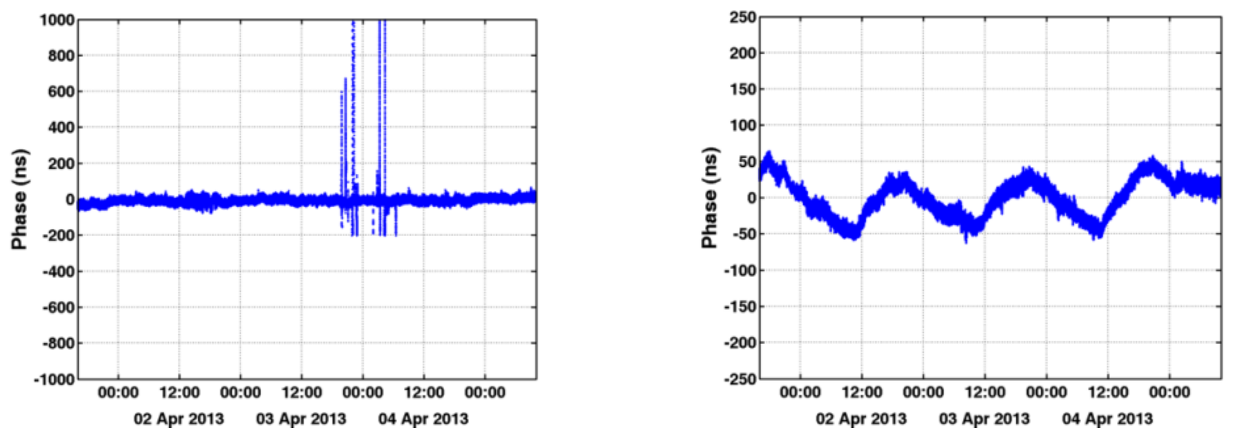

(a). PPS error of M12 (b). PPS error of eLoran UN-152A

Figure 2.7 PPS errors of M12 and eLoran UN-152A in three days

In addition to PPS accuracy, the measurement data of GPS-FDR and eLoran-FDR including frequency and angle are sent to FNET server for measurement accuracy comparison. Both short term accuracy and long term stability were assessed as shown in Figure 2.8 and Figure 2.9. Figure 2.8 (a) shows that the angles of the two FDRs are very close to each other, and Figure 2.8 (b) shows that the angle difference between the two FDRs is less than 0.001 radian. Figure 2.9 (a) shows that the frequency of the two FDRs are also very close to each other, and Figure 2.9 (b) shows that the frequency difference between the two FDRs. The frequency difference is less than 1 mHz. Note that both the angle and frequency differences are within the range of FDRs' accuracy, so the true angle and frequency difference caused by different timing sources can be ignored.

In conclusion, eLoran, as an alternative GPS independent ground-based time synchronized method, has been implemented on FDRs, and eLoran shows its timing accuracy and reliability for synchrophasor measurement.

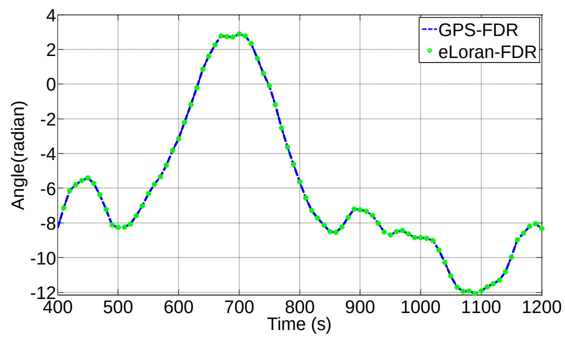

(a). Angle of GPS-FDR and eLoran-FDR

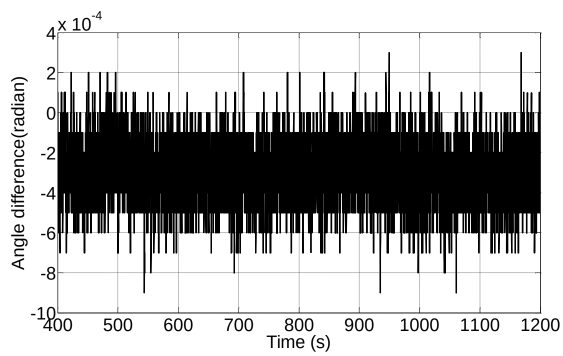

(b). Angle difference between GPS-FDR and eLoran-FDR

Figure 2.8 Angle measurement of GPS-FDR and eLoran-FDR

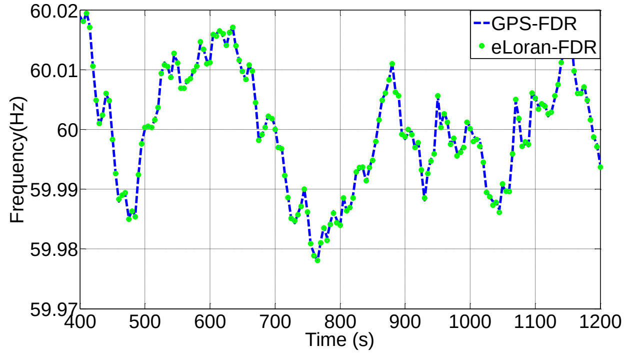

(a). Frequency of GPS-FDR and eLoran-FDR

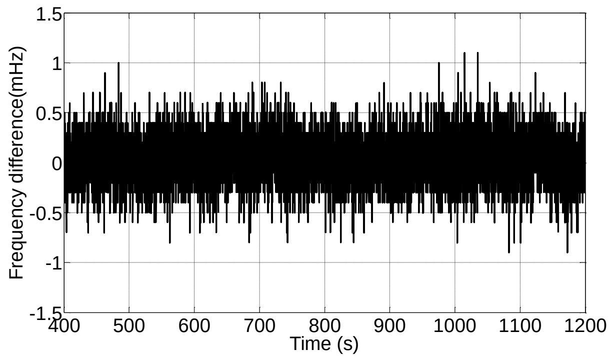

(b). Frequency difference between GPS-FDR and eLoran-FDR

Figure 2.9 Frequency measurement of GPS-FDR and eLoran-FDR

2.3 Chip Scale Atomic Clock (CSAC) testing on FDRs

2.3.1 Introduction of CSAC [29]

As shown in Figure 2.10, the Symmetricom model SA.45s is the world's first commercially available, smallest, lowest power Chip-Scale Atomic Clock (CSAC). CSAC SA. 45s shown in Figure 2.10 provides highly accurate and stable timing while achieving reduced size and weight (<17 cm^3 volume, 35g weight), and low power consumption (<120mW), and this enables CSAC in portable, battery-powered applications. The CSAC is a passive atomic clock, incorporating the interrogation technique of Coherent Population Trapping (CPT) and operating on the D1 optical resonance of atomic cesium. It has 10 MHZ CMOS-compatible output, 1 PPS output, and 1 PPS input for synchronization. The aging is less than 3.0e-10/month, and the short term stability (Allen Deviation) of 2.5e-10 @TAU is equal to 1 second.

Figure 2.10 CSAC SA 45.s

Figure 2.11 shows typical instability (Allan Deviation) of the CSAC, along with the noise floor of the phase meter, and it also shows the instabilities of typical reference timing sources, GPS and a high-performance cesium beam frequency standard [30]. It can be seen that for averaging times less than 5000 seconds, CSAC is better than GPS.

2.3.2 System setup

The setup of the testing system is shown in Figure 2.12. CSAC SA. 45s is used to provide PPS signal instead of the GPS receiver M12 to FDRs to study the accuracy of CSAC for synchrophasor measurement. Since CSAC itself does not have a timing start point, GPS is used to discipline the CSAC, which means the PPS signal of GPS is used to align the PPS signal of CSAC. The time constant of CSAC is configured to 3000 seconds, and it means GPS will discipline CSAC once every 3000 seconds.

2.3.3 Testing results

In order to test the performance of CSAC on FDRs, three scenarios were tested.

1) Short-term timing accuracy of CSAC on FDRs
2) Discipline failure of CSAC by GPS
3) Long-term timing drift of CSAC

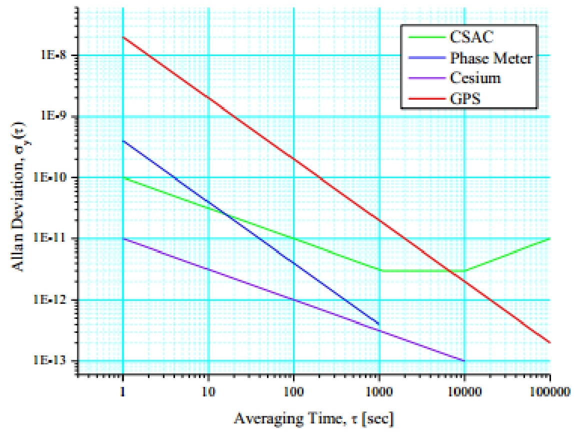

Figure 2.11 Typical instability (Allan Deviation) of CSAC,

Phase meter, GPS, and cesium beam frequency standard

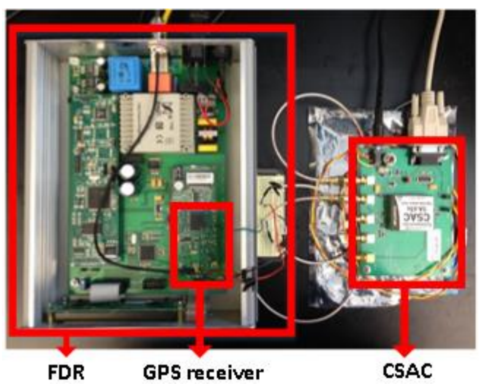

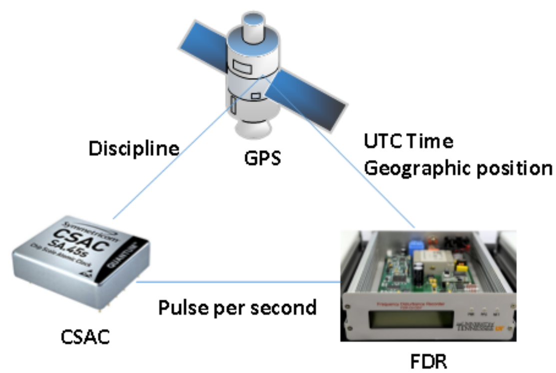

(a). CSAC-FDR experimental setup (b). CSAC-FDR setup block

Figure 2.12 Setup of CSAC testing on FDRs

The first test is to verify whether CSAC is able to provide accurate timing for FDRs. Two FDRs are set up in laboratory. Timing of one FDR is provided by GPS, called “GPS-FDR”, and timing of the other FDR is provided by CSAC, called “CSAC-FDR”. The two FDRs were connected to Doble F6150 that can generate stable and accurate 60 Hz signal. The angle and frequency errors of the two FDRs are shown in Figure 2.13 and Figure 2.14, respectively. We can see that the angle and frequency errors of the two FDRs are less than 0.02 degree and 0.5 mHz, respectively. The STD of angle and frequency errors are summarized in Table 2.1. In brief, the angle and frequency errors of the two FDRs are very close to each other, which means CSAC can provide accurate timing for FDRs in short-term.

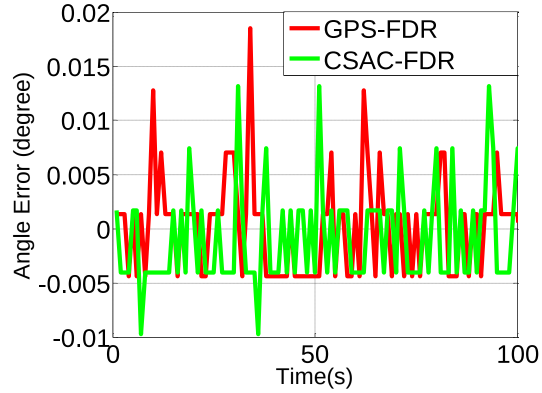

Figure 2.13 Angle errors of GPS-FDR and CSAC-FDR

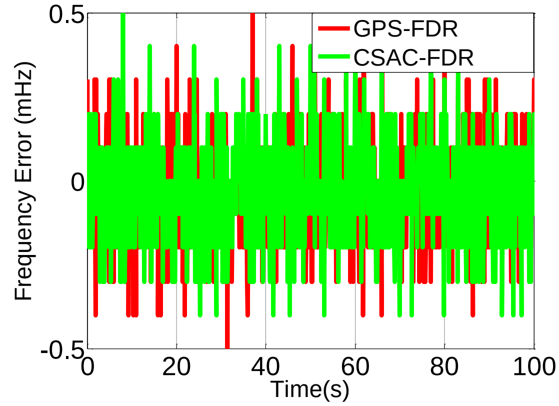

Figure 2.14 Frequency errors of GPS-FDR and CSAC-FDR

Table 2.1 STD of angle and frequency errors of GPS-FDR and CSAC-FDR

Measurement	GPS-FDR	CSAC-FDR
Angle	0.0041	0.0046
Frequency	1.45e-4	1.42e-4

The second test is to test the response of FDRs if GPS is not able to discipline CSAC successfully. First CSAC is disciplined by GPS, and then CSAC is disconnected from GPS. CSAC will require the PPS signal from GPS every 3000 seconds, however CSAC cannot be disciplined again by GPS since GPS is disconnected from CSAC. Figure 2.15 shows the response of the FDR in 4000 seconds. We can see that the angle error of CSAC-FDR starts to drift after 3000 seconds, which is expected because CSAC cannot be disciplined by GPS. However, the drift is very small and is negligible for synchropahsor measurement.

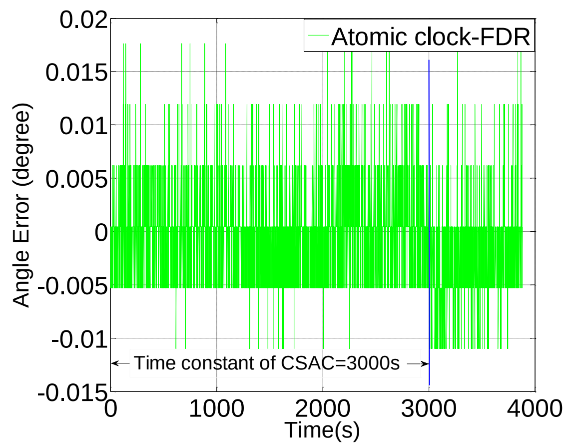

Figure 2.15 Failure of discipline

The last test is to study the timing drift of CSAC in long-term. One interesting question is that if GPS is lost for one day, how much angle error will be caused by CSAC? In order to answer this question, the timing drift of CSAC is tested, and the test procedure is shown in Figure 2.16. First, CSAC is disciplined using highly accurate XLi-GPS, then CSAC is disconnected from XLi-GPS once it is disciplined successfully. Then the PPS from CSAC and GPS are connected to an oscilloscope, and the time difference between the rising edge of the two PPS signals is measured along with time. The timing drift of CSAC in 24 hours is shown in Figure 2.17. We can see that the timing drift of CSAC increases linearly with time, and it drifts about 890 ns in 24 hours. 890 ns causes 0.0192 degree angle error for 60 Hz power grid, and 0.016 degree angle error for 50 Hz power grid, and they are very small for both 60 Hz and 50 Hz power grid. In conclusion, CSAC can provide accurate timing for PMUs when CSAC operates without GPS in one day.

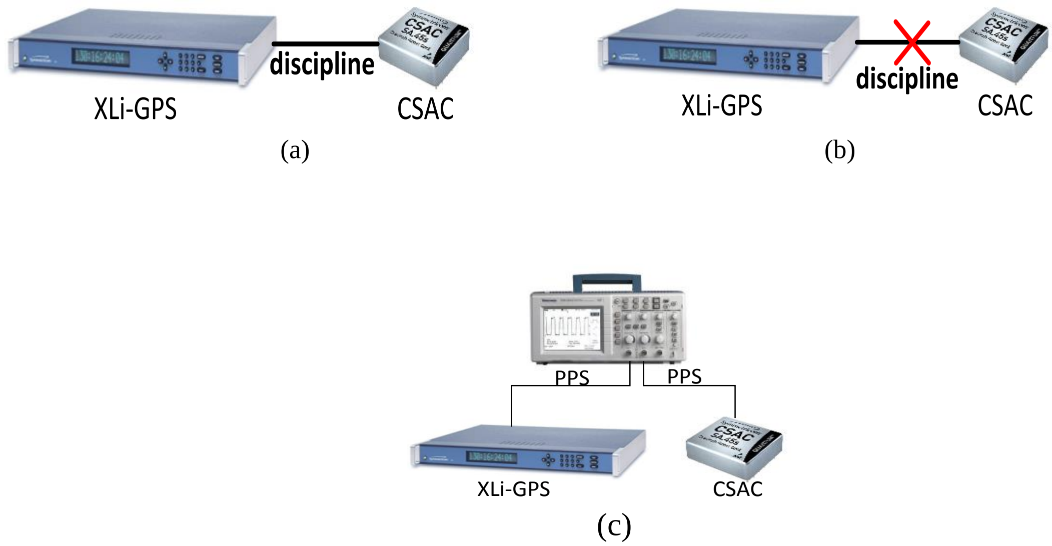

Figure 2.16 Timing drift test of CSAC

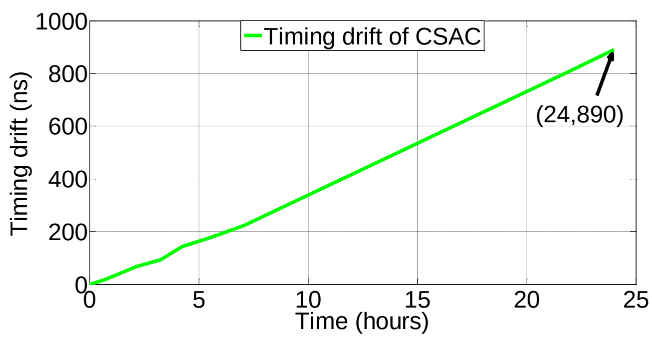

Figure 2.17 Timing drift of CSAC in 24 hours

2.3.4 Conclusion

CSAC was successfully implemented on FDRs. The following conclusions can be drawn:

1) CSAC can be used as a good GPS backup signal for some critical applications in synchrophasor measurement area.
2) Because CSAC itself does not have a timing start point, it requires an external timing source such as a GPS receiver for disciplining.
3) If CSAC cannot be disciplined by an external timing source, timing drift of CSAC is about 0.9 us per day, which is good enough for synchrophasor measurement in one day.

Chapter 3 Accuracy Analysis and Improvement of FDRs

FDR, as a whole measurement device, the error sources generally can be divided into two categories, hardware and algorithm. Since the FDR algorithm does not incur estimation error under 60 Hz condition, the estimation errors of FDRs under this condition are mainly caused by the hardware. As a result, this condition can be used to analyze the estimation errors caused by the hardware. Then according to the analysis, the FDR is upgraded to reduce the estimation errors, and the new FDR will be compared to Generation-II FDR to show the phase angle and frequency estimation accuracy improvement.

Additionally, the measurement accuracy of the FDR algorithm is also evaluated under different steady-state and dynamic conditions according to the IEEE PMU Standard to study the measurement errors cause by the algorithm.

3.1 Analysis of the hardware error sources

3.1.1 Errors caused by PPS

Ideally the time difference between two PPS signals is exactly 1 second, however the exact 1 second time difference cannot be guaranteed in practical applications. According to the analysis from eLoran system testing, the PPS error of M12 is within +/- 100 ns. In current generation FDR, the PPS signal is used to start ADC once at the beginning of each second to sample the first data in one second, so the accuracy of PPS will affect the measurement accuracy. Assuming the PPS error is T_{PPS} ns, the angle estimation error caused by PPS is

$$Ang_{Error_{PPS}} = \frac{T_{PPS} \times 10^{-9}}{T_{nom}} 360 \tag{3.1}$$

where T_{nom} is the period of the power grid signals. Assuming the PPS error is 100 ns and power grid frequency is 60Hz, then the angle error caused by PPS is

$$Ang_{Error_{PPS}} = \frac{100 \times 10^{-9}}{1/60} 360 = 0.0022 \text{ (degree)}$$

We can see the angle error caused by 100 ns PPS error is only about 0.0022 degree.

According to operating principle and measurement algorithm of FDR, the PPS error will only affect the time to sample the data in one second, and it will not affect the time interval between two adjacent samples. As a result, all the measurement angles in each second will have the same dc offset error computed by (3.1). Assuming the frequency of the input signal is constant, and since the frequency is the derivative of angle and the angle errors during one second is constant, PPS error will not induce frequency estimation error, which can be represented as

$$Freq\_Error_{PPS} = \frac{\mathrm{d}(Ang\_Error_{PPS})}{2\pi dt} = 0 \text{ (Hz)} \tag{3.2}$$

We can see that the PPS will cause angle estimation error, but not frequency estimation error if the system frequency is in steady-state. However, the system frequency cannot be always in steady-state. For example, if the frequency of the power grid ramps at a rate of 1Hz/s, the frequency estimation error caused by the PPS error is

$$Freq\_Error_{PPS} = \frac{100 \times 10^{-9}}{1} \times 1 \text{ (Hz)} = 0.1 \text{ (μHz)}$$

The 1 μHz error can be ignored in power system application.

In brief, compared to the frequency, the angle measurement error is more sensitive to the PPS error. However, the angle error caused by the PPS error is still quite small. This can also be concluded from the CSAC testing, in which CSAC has much better PPS accuracy, but there are no angle error difference between GPS-FDR and CSAC-FDR.

3.1.2 Errors caused by Analog to Digital Converter (ADC)

The ADC in current generation FDRs is a 14-bit ADC, and the input voltage range is -10 V to 10 V. For the sake of safety, 120 V signal is converted to 15.6 V (peak to peak) signal as the input signal of the ADC.

According to the datasheet of AD7865 used in FDRs, the INL is about 1.5 LSB. As a result, the maximum data conversion error caused by ADC is

$$Conv\_Error_{ADC} = \pm 1.5 \frac{20}{2^{14}} (V) = \pm 3.66 \text{ (mV)}$$

In order to estimate how much are the angle and frequency estimation errors caused by the ADC, a noise that is randomly distributed between -3.66 mV to 3.66 mV is added to a 15.6 V signal. Figure 3.1 shows the angle and frequency errors in simulation, and Figure 3.2 shows the measurement errors of angle and frequency of FDR under filed test. In addition, the STD of angle and frequency errors is shown in Table 3.1.

Based on the 1.5 LSB assumption, we can see that the angel and frequency estimation errors caused by ADC will account for about 50% of the angle and frequency measurement errors in the field test. This demonstrated that it is necessary to upgrade the ADC in next-generation FDRs.

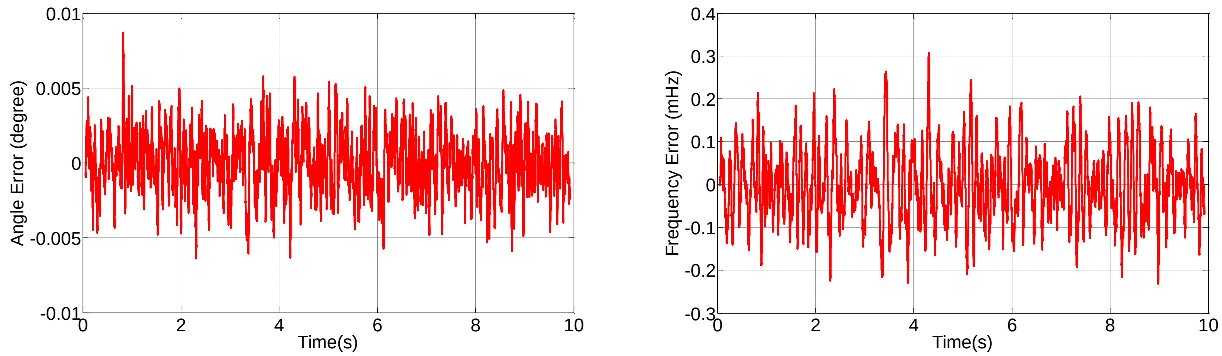

(a). Angle error caused by ADC (b) Frequency error caused by ADC

Figure 3.1 Emulation of angle and frequency errors caused by ADC

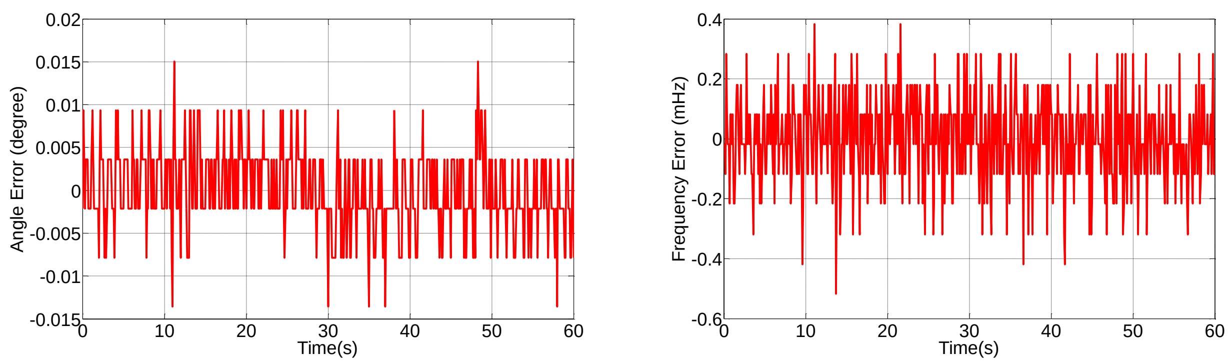

(a). Angle error under filed test (b). Frequency error under field test

Figure 3.2 Angle and frequency errors of FDR under field test

Table 3.1 STD of angle and frequency error in simulation and field test

Measurement	Simulation	Field test
Angle	0.0020	0.0046
Frequency	0.0841	0.1465

3.2 Improvement of FDRs

3.2.1 Hardware improvement of FDRs

Since the ADC will introduce a part of the estimation errors, so a high-precision 16-bit ADC is used in the new FDR. In the new FDR, Analog Devices AD7663 is used. Based on the Pulsarcore, the AD7663 is a bipolar 16-bit, 250 kSPS, charge redistribution SAR Analog-to-Digital Converter that operates from a single 5 V power supply [31]. It contains a high-speed 16-bit sampling ADC, a resistor input scalar that allows various input ranges, an internal conversion clock, error correction circuits, and both serial and parallel system interface ports. It has maximum +/- 3LSB INL (+/- 0.0046% of full scale).

In order to improve the performance of AD7663, instead of using internal voltage reference, an external voltage reference AD780 is used as the voltage reference for AD7663. The AD780 is an ultrahigh precision band gap reference voltage that provides a 2.5 V or 3.0 V output from inputs between 4.0 V and 36 V [32]. Low initial error and temperature drift combined with low output noise and the ability to drive any value of capacitance make the AD780 the ideal choice for enhancing the performance of high resolution ADCs and DACs, and for any general-purpose precision reference application. A 6-1/2 high-precision Multimeter is used to measure the voltage stability of AD780, the voltage STD of AD780 is less than 5 uV, which is accurate enough for ADC.

In addition, DSP model TMS320C6713 is chose as the new computation platform instead of TMS320C2407. In contrast to TMS320LF2407 that is a 16-bit fixed point DSP and has 30-MIPS performance, TMS320C6713 is a 32-bit floating-point digital signal process and has maximum 300-MIPS [33]. The new DSP has higher MIPs that will increase the computation speed; the float-point feature will enhance the dynamic range and precision for the FDR algorithm.

At last, the new FDR also adopts better operational amplifiers, better voltage regulator, integrated EMI filter, and a 50 MHz oscillator instead of 15 MHz crystal. The hardware upgrade will contribute to the estimation accuracy improvement of FDRs, and it will be verified in 3.3.

3.2.2 Digital averaging filter

Since the input power grid signal contains noise and the hardware of FDRs also induces noise to the input signal, it is necessary to study the method to filter noise. Generally a typical band-pass finite impulse response (FIR) filter can be used to filter the noise, however the impulse response time and group delay time of such a filter will increase both dynamic response time and the measurement latency. For example, an $8T_0$ (T_0: period of fundamental frequency cycle) window symmetrical Type I FIR filter has an $8T_0$ response time (0.1333 s) and a $4T_0$ group delay (0.0667 s), which will affect the application of synchrophasor measurements in real-time protection and control. In addition, to reduce the effect of the filter on measurement accuracy under off-nominal frequency condition, the center-frequency of the filter has to be adaptively tuned to the power grid frequency. However, this is very challenging since the frequency is the measurement output and it cannot be measured accurately.

Instead of an FIR band-pass filter, an oversampling method is utilized to reduce the noise. First, the input signal is oversampled by N_s times to $N_s f_{samp}$ sampling rate. Then the input signal is decimated by a factor of N_s by averaging N_s samples. As a result, the decimated signal can be obtained by

$$Avg(i) = \frac{\sum_{i\times Ns-(Ns-1)/2}^{i\times Ns+(Ns-1)/2} Sa(j)}{Ns} \ (i \geq 0) \tag{3.3}$$

where $Avg(i)$ is the sample data of decimated signal, and $Sa(j)$ is the sample data of input signal. $Avg(i)$ is calculated by averaging N_s samples from $Sa(i \times Ns - (Ns-1)/2)$ to$Sa(i \times Ns + (Ns-1)/2)$, so the sampling rate of the decimated signal is still f_{samp}. The illustration of the filter is shown in Figure 3.3. The averaging process is robust since it does not rely on the frequency of input signal. Actually, it may improve the robustness of the measurement algorithm since it smooths the input signal.

Since there are Ns samples in one averaging window, the window length of the filter is

$$T_{Avg} = (Ns - 1)\ \frac{1}{Ns \times f_{samp}} \tag{3.4}$$

The response time of the averaging filter is T_{Avg}, and the group delay is $T_{Avg}/2$. For example, if $f_{samp} = 1440$ and $Ns = 31$, the response time of the filter is about 0.67 ms, and group delay is about 0.336 ms. They can be negligible in synchrophasor measurement applications.

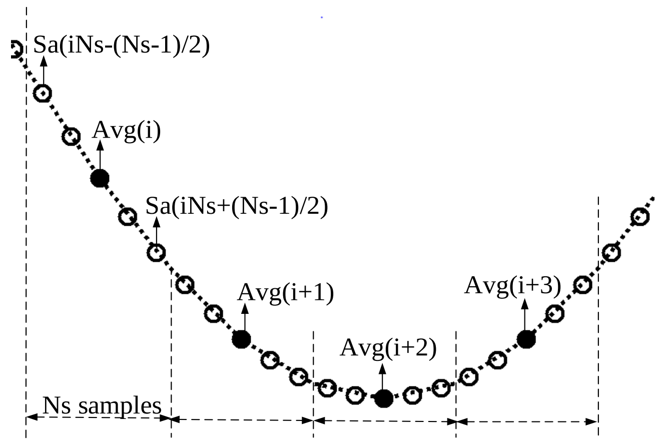

Figure 3.3 Digital averaging filter

Generally, the noise can be better filtered with the increase of Ns. However, a larger Ns requires a higher sampling rate, which increases the hardware computation burden. As a result, a balance needs to be struck between filter performance and hardware burden. Based on the FDR algorithm, different Ns are tested to obtain a suitable number of averaging points (Ns), and STD of frequency errors are show in Figure 3.4. We can see that that 15-points averaging can limit the STD to 0.1×10^{-4} , which is good enough for noise reduction.

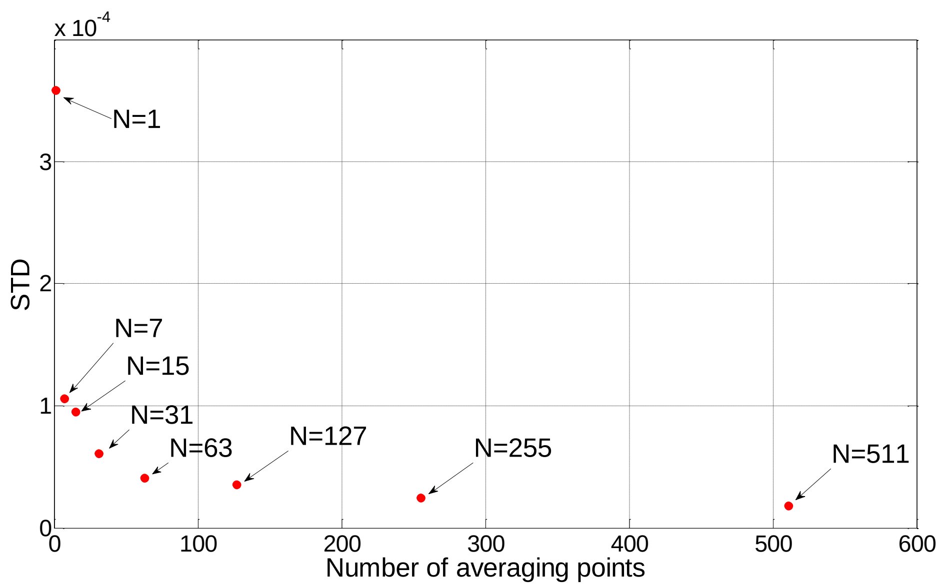

Figure 3.4 STD of frequency estimation errors with respect to Ns

Besides we verify the effect of averaging filter on noise reduction, we need to verify the averaging filter does not affect the angle and frequency estimation accuracy under noise free condition. The averaging filter is assessed under frequency range and frequency ramp condition to evaluate the effect of the averaging filter on estimation accuracy. FDR algorithm is used as the algorithm to test the averaging filter. The algorithm with filter is called "Avg-FDR Algorithm", the algorithm without filter is called "FDR Algorithm". Figure 3.5 and Figure 3.6 show the angle and frequency measurement errors of the two algorithms under frequency range and frequency ramp condition, and we can see that the estimation results of the two algorithms are very close to each other. This demonstrates that the averaging filter does not affect the estimation accuracy under both steady-state and dynamic conditions for noise free signal.

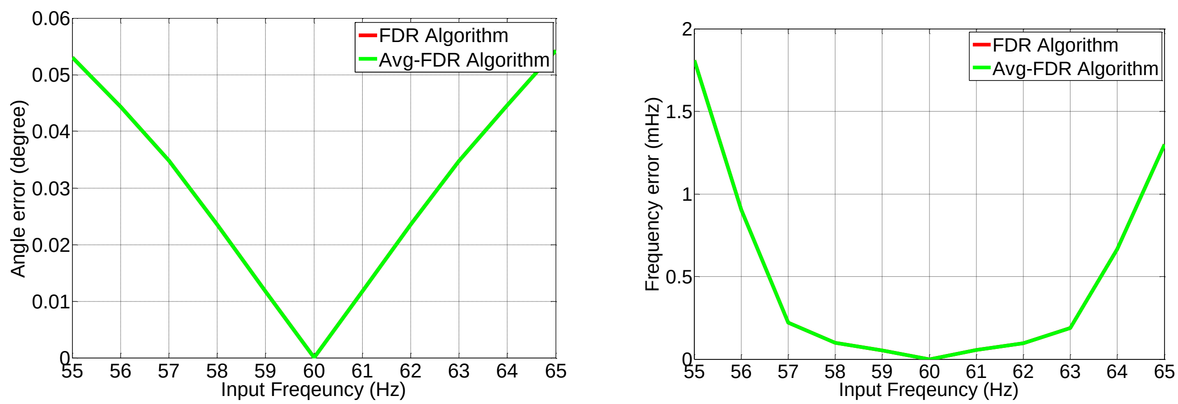

(a). Angle error (b). Frequency error

Figure 3.5 Averaging filter test under frequency range condition without noise

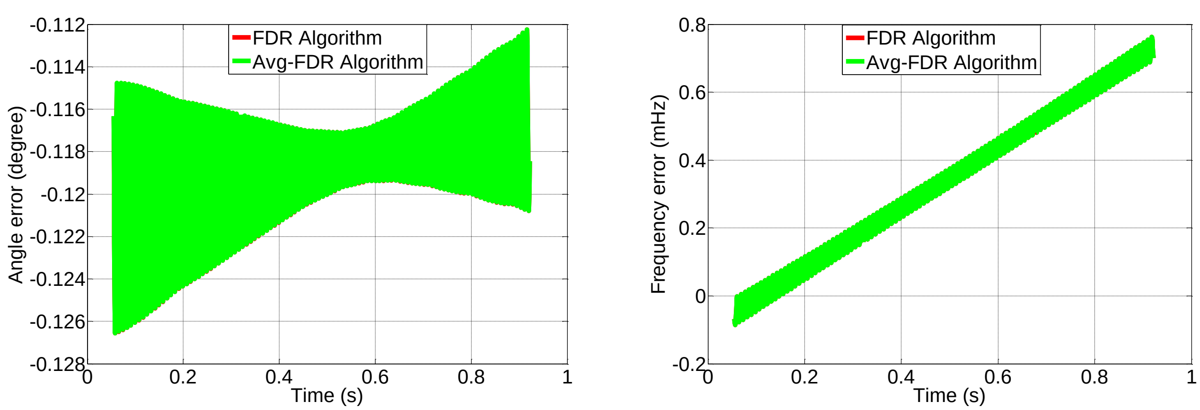

(a). Angle error (b). Frequency error

Figure 3.6 Averaging filter test under frequency ramp condition without noise

Figure 3.7 and Figure 3.8 show the angle and frequency measurement errors of the two algorithms under noise condition. We can see that the digital averaging filter can greatly reduce the measurement errors under different conditions.

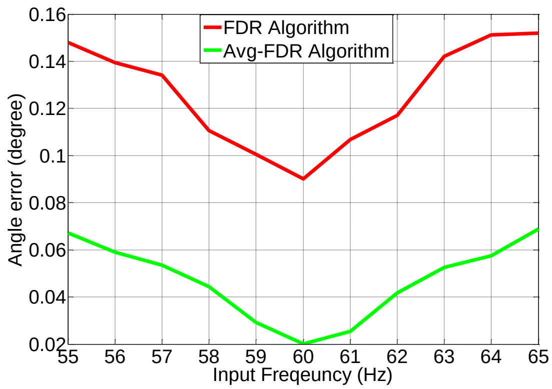

(a). Angle error

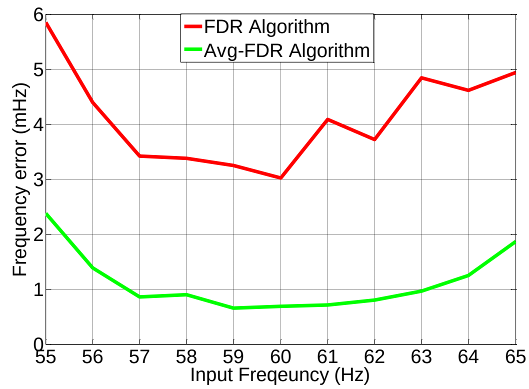

(b). Frequency error

Figure 3.7 Averaging filter test under frequency range condition with noise

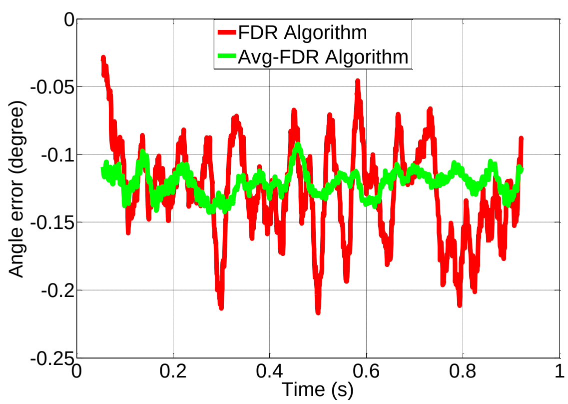

(a). Angle error

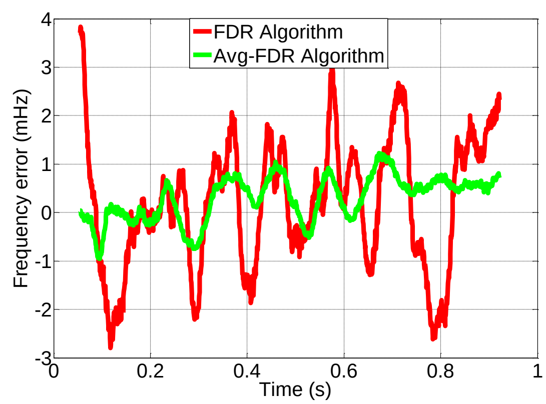

(b). Frequency error

Figure 3.8 Averaging filter test under frequency ramp condition with noise

3.3 Testing of new FDR

In this section, the new FDR is tested under different frequency condition to verify the accuracy improvement. In contrast, the estimation accuracy of GenII-FDR is compared to the new FDR.

The angle and frequency errors of the GenII-FDR and new FDR under 60 Hz test are shown in Figure 3.9 and Figure 3.10. The errors under 59.5 Hz condition are shown in Figure 3.11 and Figure 3.12. The STD of the angle and frequency errors are summarized in Table 3.2.

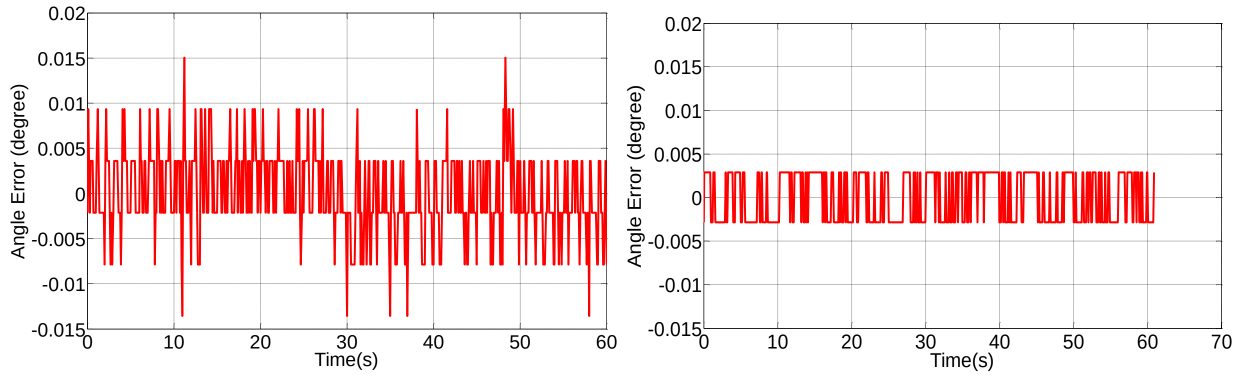

(a). Angle error of GenII-FDR (b). Angle error of new-FDR

Figure 3.9 Angle errors of GenII-FDR and new FDR under 60Hz test

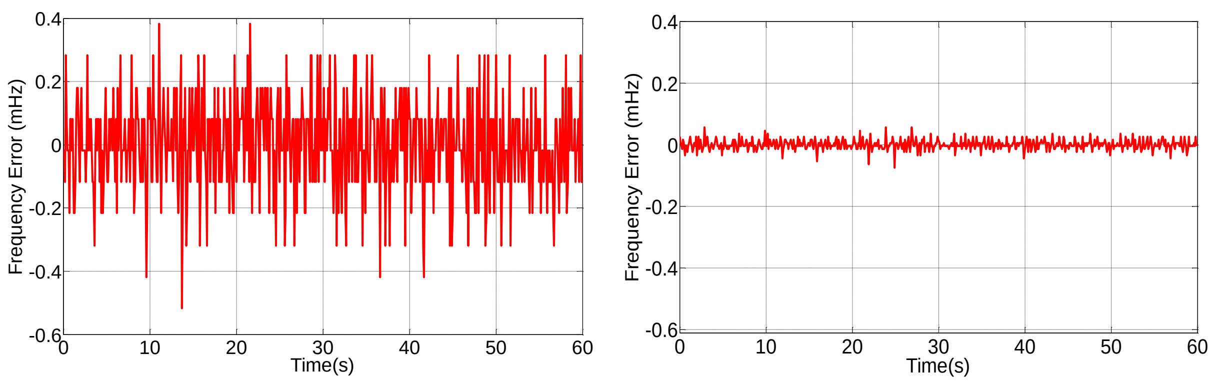

(a). Frequency error of GenII-FDR (b). Frequency error of new-FDR

Figure 3.10 Frequency errors of GenII-FDR and new-FDR under 60Hz test

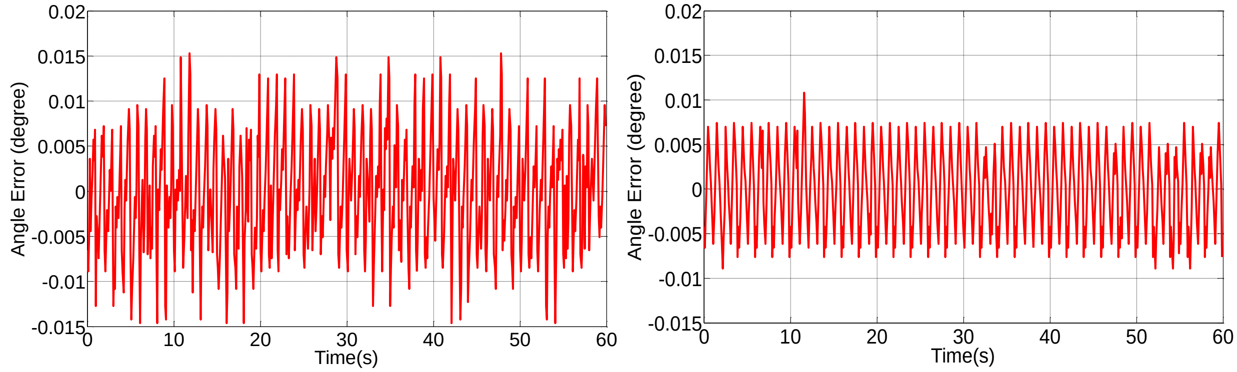

(a). Angle error of GenII-FDR (b). Angle error of new-FDR

Figure 3.11 Angle errors of GenII-FDR and new-FDR under 59.5 Hz test

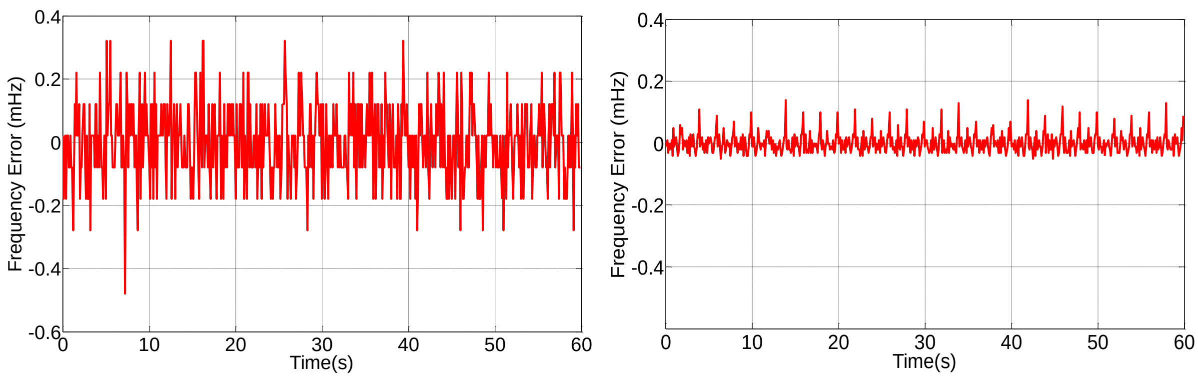

(a). Frequency error of GenII-FDR (b). Frequency error of new-FDR

Figure 3.12 Frequency errors of GenII-FDR and new-FDR under 59.5 Hz test

Table 3.2 STD of angle and frequency errors of GenII-FDR and new-FDR

Measurement	60 Hz		59.5 Hz	
	GenII-FDR	New-FDR	GenII-FDR	New-FDR
Angle	0.0046	0.0029	0.0065	0.0044
Frequency	0.1465	0.0158	0.1193	0.0312

From the testing results under 60Hz condition, the angle error is reduced from 0.015 degree to 0.003 degree, and the frequency error is reduced from about 0.4 mHz to 0.06 mHz. The new-FDR improve the angle and frequency estimation accuracy almost by one order of magnitude. The new FDR also has improved estimation accuracy under off-nominal frequency condition. So we can conclude that the upgrade of the hardware contribute to the estimation accuracy improvement for both angle and frequency.

3.4 Introduction of FDR algorithm

Besides the hardware error sources, the measurement algorithm will also cause measurement errors, particularly under off-nominal frequency conditions. In the following part, the FDR measurement algorithm is introduced first, and then the measurement accuracy of the FDR algorithm will be assessed under different steady-state and dynamic conditions.

3.4.1 Frequency estimation algorithm of FDRs

A sinusoidal signal of a known frequency f is described by its magnitude $\mathrm{X_m}$ and angular position $\emptyset$ with respect to an arbitrary time reference

$$X(t) = \sqrt{2}X_m\cos(2\pi f t + \emptyset) \tag{3.5}$$

The phasor representation of $X(t)$ is given by

$$X(t) = X_m\angle\emptyset \tag{3.6}$$

The magnitude of the phasor is the root mean square (rms) value of the signal, and the frequency does not appear in the phasor representation; but it determines the phasor angle.

DFT is a one of the common algorithms for phasor estimation. Assuming there are N samples $\{x_k\}$, $k \in [1, N]$ per cycle of fundamental frequency, the phasor of fundamental frequency component by classic DFT is

$$\overline{X_1} = \frac{1}{\sqrt{2}}(\frac{2}{N}\sum_{k=1}^{N} x_k\cos\left(\frac{2\pi}{N}k\right) - j\frac{2}{N}\sum_{k=1}^{N} x_k\sin\left(\frac{2\pi}{N}k\right)) \tag{3.7}$$

Denoting $\frac{2}{N}\sum_{k=1}^{N} x_k\cos\left(\frac{2\pi}{N}k\right)$ by $X_c^{(1)}$ and $\frac{2}{N}\sum_{k=1}^{N} x_k\sin\left(\frac{2\pi}{N}k\right)$ by $X_s^{(1)}$ and using the recursive DFT method derived in [6], each successive phasor is calculated as follows:

$$\begin{cases} X_c^{(k+1)} = X_c^{(k)} + \frac{2}{N}(x_{k+1} - x_{k+1-N})\cos(\frac{2\pi}{N}k) \\ X_s^{(k+1)} = X_s^{(k)} + \frac{2}{N}(x_{k+1} - x_{k+1-N})\sin(\frac{2\pi}{N}k) \end{cases} \tag{3.8}$$

Thus, a new phasor is calculated for every new sample data after initialization, and the first sample data is removed. The angle of k-th phasor is given by:

$$\varphi(k) = tan^{-1}\frac{-X_s^{(k)}}{X_c^{(k)}} \tag{3.9}$$

Assuming phasor angle varies as a quadratic polynomial function with respect to the samples. Therefore,

$$\varphi(k) = a_0 + a_1 k + a_2 k^2 \tag{3.10}$$

Consider M angles are obtained from recursive DFT, and the relationship between angles and the coefficients of the polynomial is:

$$\begin{cases} \varphi(1) = a_0 + a_1 1 + a_2 1^2 \\ \varphi(2) = a_0 + a_1 2 + a_2 2^2 \\ \quad\quad\quad\quad . \\ \quad\quad\quad\quad . \\ \quad\quad\quad\quad . \\ \varphi(M) = a_0 + a_1 M + a_2 M^2 \end{cases} \tag{3.11}$$

Rewrite (3.11) in a matrix form:

$$\begin{bmatrix} \varphi(1) \\ \varphi(2) \\ . \\ . \\ . \\ \varphi(M) \end{bmatrix} = \begin{bmatrix} 1 & 1 & 1^2 \\ 1 & 2 & 2^2 \\ . & . & . \\ . & . & . \\ . & . & . \\ 1 & M & M^2 \end{bmatrix} \begin{bmatrix} a_0 \\ a_1 \\ a_2 \end{bmatrix} \tag{3.12}$$

Or,

$$\emptyset = \boldsymbol{Xa} \tag{3.13}$$

The coefficients in matrix $\boldsymbol{a}$ can be estimated by least squares fitting method:

$$\boldsymbol{a} = [\boldsymbol{X^T X}]^{-\boldsymbol{1}} \boldsymbol{X^T} \emptyset \tag{3.14}$$

Then, the frequency deviation of the input signal from the nominal frequency can be calculated by

$$\Delta f \approx \frac{1}{2\pi} N f_0 (a_1 + 2 a_2 N f_0 t) \tag{3.15}$$

where t determines which instant inside the estimation window the computed frequency correspond to. The frequency estimated by (3.15) is already rather accurate. However, in order to improve the accuracy under off-nominal frequency condition, resampling method that resampling the waveform with the estimated frequency is used in FDRs [6]. In brief, since DFT method is accurate when there are integer samples per cycle, resampling method is used to interpolate and reconstruct the input signal to make there are approximately integer samples per cycle, then the frequency is estimated again using the new data [35].

With the resampling method, the final frequency can be computed by

$$f_{Final} = f_0 + \Delta f + \Delta f' \tag{3.16}$$

where $\Delta f'$ is the frequency deviation estimated using the resampled data.

3.4.2 Angle estimation algorithm of FDRs [7]

If the signal is sampled *N* times per cycle of the f_0 waveform, the sample is

$$x_k = \sqrt{2}X\cos\left(\frac{2(f_0 + \Delta f)k\pi}{f_0 N} + \varphi\right) \tag{3.17}$$

The DFT of $\{x_k\}$ for the data window between k=0 and k=N-1 can be calculated as [7]

$$X = Pe^{j\varphi} + Qe^{-j\varphi} \tag{3.18}$$

where

$$\begin{cases} P = \sqrt{2}X\dfrac{\sin(\frac{\pi\Delta f}{f_0})}{Nsin(\frac{\pi\Delta f}{Nf})}e^{j(\frac{(N-1)\pi\Delta f}{Nf_0})} \\ Q = \sqrt{2}X\dfrac{\sin(\frac{\pi\Delta f}{f_0})}{Nsin(\frac{\pi(2f_{0+}\Delta f}{Nf})}e^{-j(\frac{(N-1)\pi(2f_0+\Delta f)}{Nf_0})} \end{cases}$$

In this equation, φ is the angle of the input signal. If Δf is close to 0, which means the system frequency is close to 60Hz, we have

$$\mathrm{X} = \sqrt{2}\mathrm{X}e^{j\varphi} \tag{3.19}$$

Then the angle can be easily estimated by

$$\varphi = \arctan\left(\frac{Imag(X)}{Real(X)}\right) \tag{3.20}$$

However, when the system frequency deviates from 60Hz, Q is not equal to 0, then the angle φ could not be estimated accurately. The error arise when the angle is still estimated using (3.20).

According to the analysis in [7], the angle error under off-nominal frequency condition can be represented as

$$e \approx \frac{\Delta f}{2f_0 + \Delta f}\sin\left(2\varphi + \frac{(N-1)2\pi(f_0+\Delta f)}{Nf_0}\right)$$
$$= \frac{Q}{P}\sin(2\varphi + \frac{(N-1)2\pi(f_0+\Delta f)}{Nf_0}) \tag{3.21}$$

It can be seen that the magnitude of error is $\frac{Q}{P}$ and directly proportional to Δf. If Δf is equal to 0, Q is equal to 0 and error is equal to 0. In GenII-FDR, in order to improve the angle estimation accuracy under off-nominal frequency condition, Qps-DFT method is used [7]. The Qps-DFT method imitates three-phase data using single-phase input and it can reduce the error from

$$e \approx \frac{\Delta f}{2f_0 + \Delta f}\sin\left(2\varphi + \frac{(N-1)2\pi(f_0+\Delta f)}{Nf_0}\right) \tag{3.22}$$

to

$$e_{Qps} \approx \frac{2\sqrt{3}\pi\Delta f}{9f_0}\frac{\Delta f}{2f_0 + \Delta f}\sin\left(2\varphi + \frac{(N-1)2\pi(f_0+\Delta f)}{Nf_0}\right) \tag{3.23}$$

The attenuation effect of the error is $\frac{2\sqrt{3}\pi\Delta f}{9f_0}$.

As a result, the angle estimation accuracy can be improved by modifying the DFT algorithm. In the following part, the FDR algorithm will be tested under different steady-state and dynamic conditions according to the IEEE PMU Standard [26], [27]. However, the tests are not limited by the Standard. The tests also include the harmonic distortion test when the fundamental frequency deviates from the nominal frequency, and noise test.

3.5 Testing of FDR algorithm

3.5.1 Frequency range test

The test signal is $\mathrm{s(t)} = 1\cos(2\pi f t)$, and f increases from 55 Hz to 65 Hz at a step of 1Hz, the angle and frequency errors are shown in Figure 3.13. The maximum angle error is about 0.053 degree, and the maximum frequency error is about 1.8 mHz. Both the frequency and angle accuracy of FDR algorithm is good under frequency range condition.

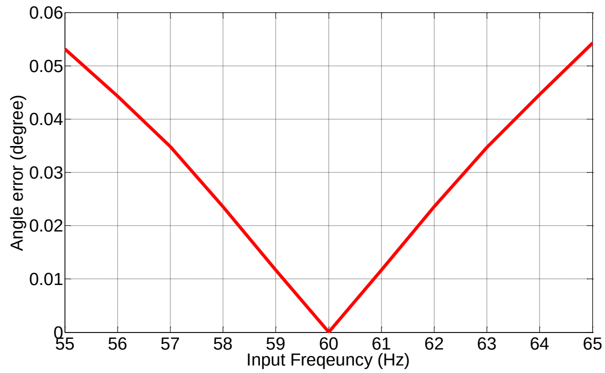

(a). Angle error

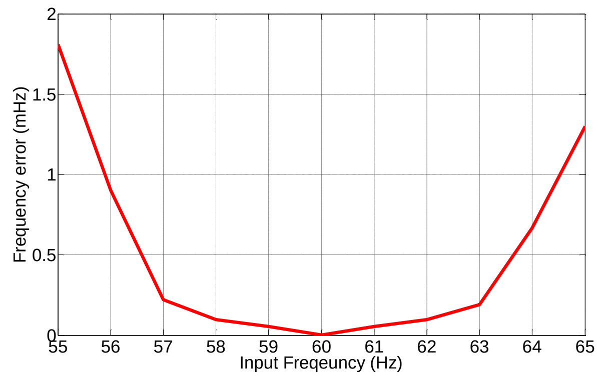

(b). Frequency error

Figure 3.13 Frequency range test of FDR algorithm

3.5.2 Harmonic distortion test

The test signal of FDR algorithm under harmonic distortion test is

$$s(t) = 1\cos(2\pi 60t) + HarMag(i)\cos(2\pi i60t), \qquad i \in [2, \ldots, 50]$$

$HarMag(i)$ is the actual magnitude of the i-th order harmonic component. Assuming the magnitude of i-th order harmonics of input signal is 0.1, since a RC analog filter is used to filter the higher order harmonics in FDRs, the actual magnitude of i-th order harmonic component for FDR algorithm is

$$HarMag(i) = 0.1 * \frac{1}{\sqrt{1^2 + (2\pi i60RC)^2}}$$

where R is equal to 860 Ω, and C is equal to 1 uF.

The angle and frequency errors under this condition are shown in Figure 3.14. It can be seen that the harmonics will not result in estimation errors for both angle and frequency. In brief, the FDR algorithm is immune to harmonics when the power grid frequency is equal to 60Hz. However, it should be noted that the fundamental frequency of power grid signal deviates from 60Hz in most of time, so this test is not enough to test the effect of harmonic distortion on measurement accuracy. In next test, the fundamental frequency is not equal to nominal value.

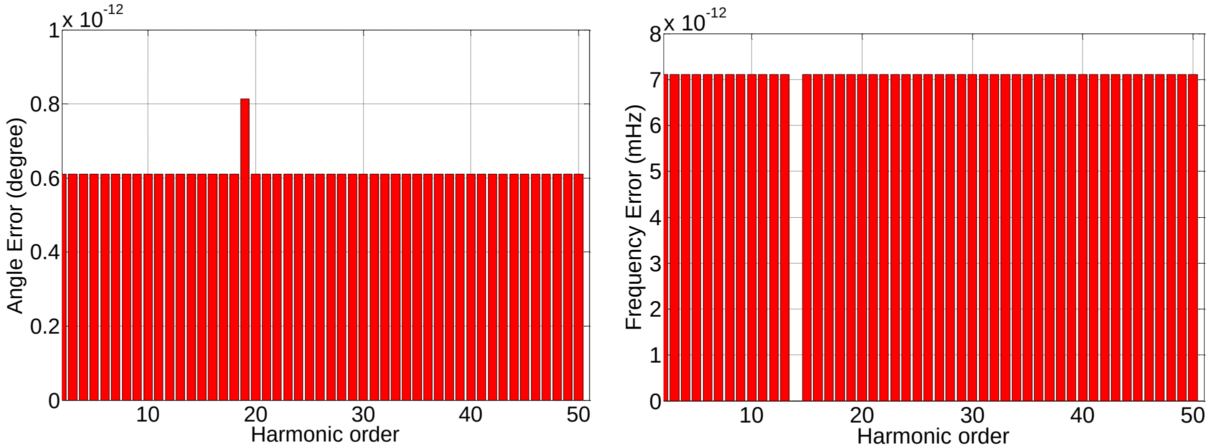

(a). Angle error (b). Frequency error

Figure 3.14 harmonic distortion test

3.5.3 Harmonic distortion test under off-nominal frequency condition

The test signal under this test is

$$s(\mathrm{t}) = 1\cos(2\pi f t) + HarMag(i)\cos(2\pi i f t)$$

Note that this test is not required in PMU Standard, however the test signal in this test exists in a real power grid. In this test, different fundamental frequencies are tested including 59 Hz, 59.5 Hz, 59.95 Hz, 60.05 Hz, 60.5 Hz, and 61 Hz. The angle and frequency errors of FDR algorithm under different fundamental frequency conditions are shown from Figure 3.15 to Figure 3.20, respectively.

We can see under 59.0 fundamental frequency condition, the angle estimation errors are mainly caused by 22nd to 26th, 48th and 50th harmonics, and frequency estimation errors are mainly caused by 48th and 50th harmonics. Both the angle and frequency estimation errors are not negligible since the angle error is larger than 0.5 degree, and frequency error is about 15 mHz.

Under 59.5 Hz fundamental frequency condition, the angle estimation errors are mainly caused by 23rd, 25th, and 47th to 50th order harmonics, and frequency estimation errors are mainly caused by 23th and 25th harmonics. Although the fundamental frequency is closer to 60 Hz compared to 59.0 Hz, the angle and frequency errors are even larger.

Under 59.95 Hz fundamental frequency condition, both the angle and frequency errors are mainly caused by 23th, 25th, 47th and 49th order harmonics. Note that the errors do not decrease although the fundamental frequency is very close to 60 Hz.

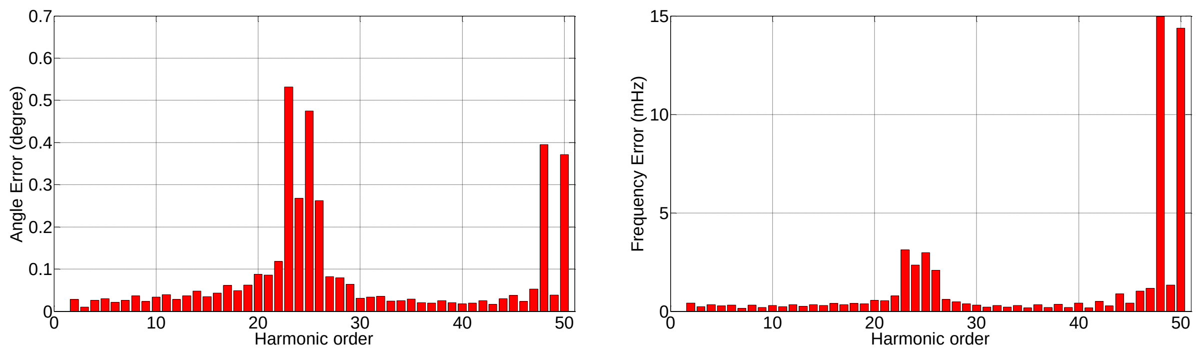

(a). Angle error (b). Frequency error

Figure 3.15 Harmonic distortion test under 59.0 Hz condition

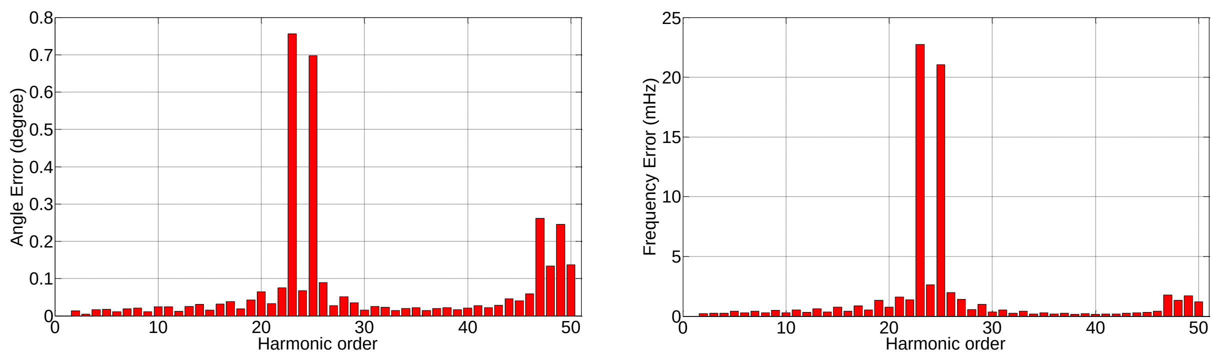

(a). Angle error (b). Frequency error

Figure 3.16 Harmonic distortion test under 59.5 Hz condition

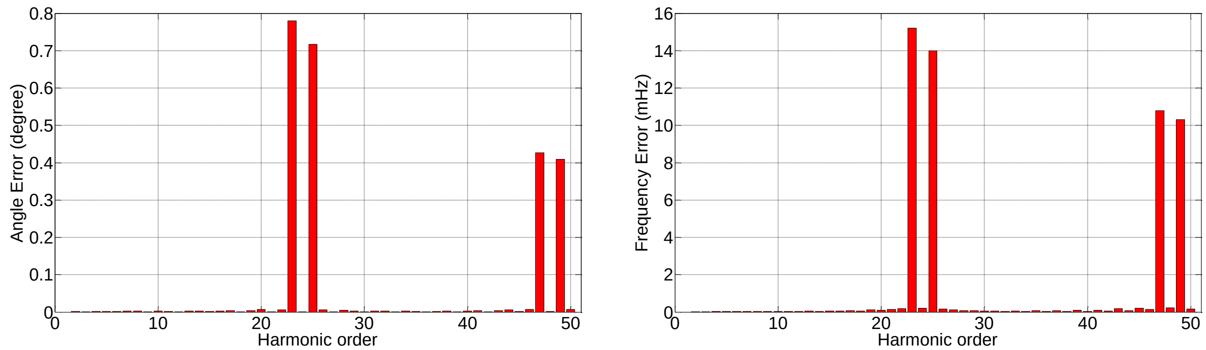

(a). Angle error (b). Frequency error

Figure 3.17 Harmonic distortion test under 59.95 Hz condition

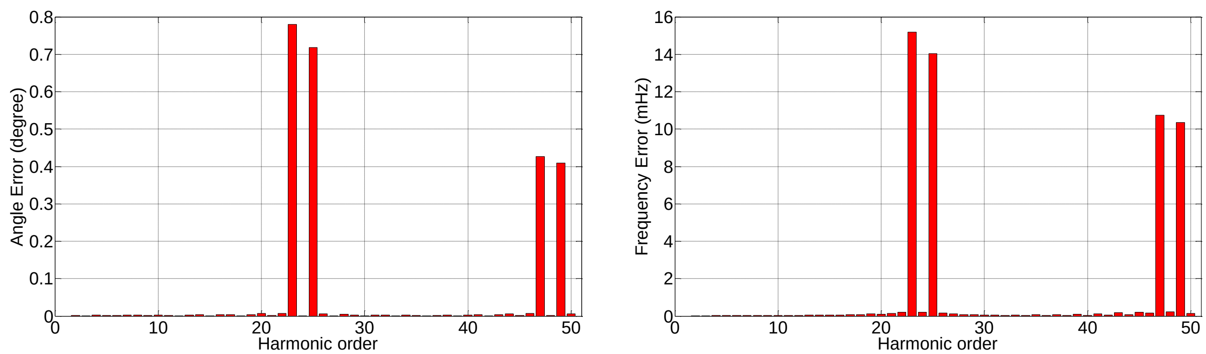

(a). Angle error (b). Frequency error

Figure 3.18 Harmonic distortion test under 60.05 Hz condition

Under 60.05 Hz fundamental frequency condition, the errors are very similar to the errors under 59.95 Hz fundamental frequency condition. Both the angle and frequency errors are mainly caused by 23th, 25th, 47th and 49th order harmonics, and they are not negligible.

Under 60.5 Hz fundamental frequency condition, the angle errors are mainly caused by 23th, 25th, and 46th to 49th order harmonics, and the frequency errors are mainly caused by 23th and 25th order harmonics.

Under 61 Hz fundamental frequency condition, the angle and frequency estimation errors are mainly caused by 22nd to 25th, 46th and 48th order harmonics. Although the errors are less than the errors under other fundamental frequency conditions, they are still rather large.

The errors under different order of harmonics are added together and shown in Table 3.3. Note that if there are multiple harmonics existing at the same time, the total angle and frequency errors should be smaller than the number shown in the Table since the errors caused by different order of harmonics could cancel with each other.

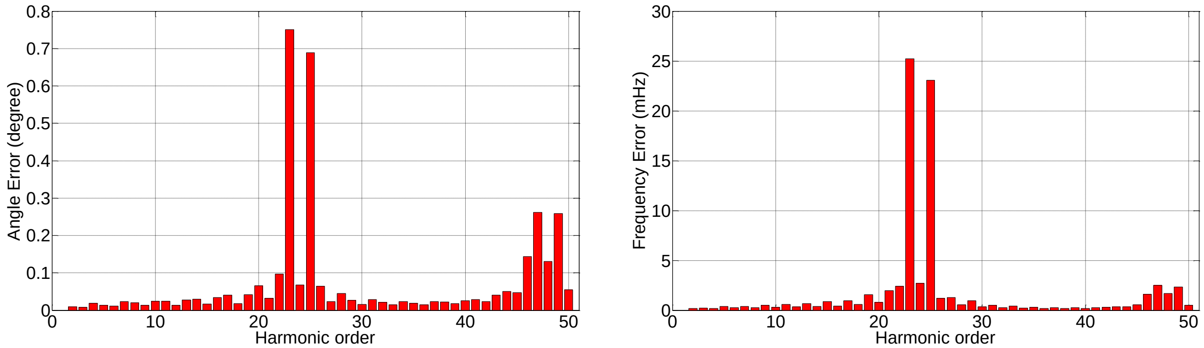

(a). Angle error (b). Frequency error

Figure 3.19 Harmonic distortion test under 60.5 Hz condition

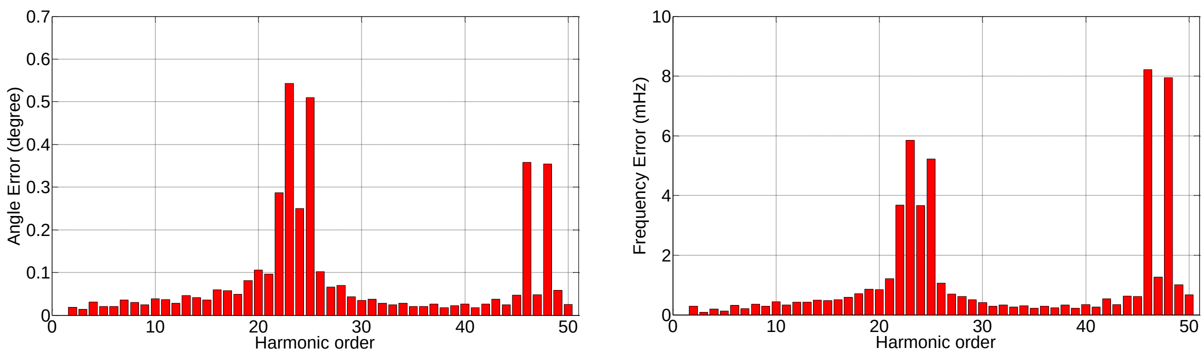

(a). Angle error (b). Frequency error

Figure 3.20 Harmonic distortion test under 61 Hz condition

Table 3.3 Additions of angle and frequency errors under 10% harmonic distortion condition

Input frequency	59	59.5	59.95	60.05	60.5	61
Angle (degree)	3.9795	3.4979	2.4522	2.4546	3.5172	4.0174
Frequency (Hz)	0.057	0.074	0.053	0.053	0.083	0.055

The errors under 1% harmonies condition are shown in Table 3.4.

Table 3.4 Additions of angle and frequency errors under 1% harmonic distortion condition

Input frequency	59	59.5	59.95	60.05	60.5	61
Angle (degree)	0.8901	0.5895	0.2694	0.2696	0.5911	0.8947
Frequency (Hz)	0.008	0.008	0.005	0.005	0.009	0.008

According to the test, we can see that the FDR algorithm is not immune to harmonics when the fundamental frequency deviates from nominal frequency, although the resampling method can help reduce the estimation errors. More importantly, the errors increase dramatically when the order of the harmonics is close to 25^{th} or 50^{th} order of harmonic components. The reason is that the frequency of those harmonic components are close to integer times of the sampling rate, which is 1440 Hz/s. From the single processing point of view, those harmonic components will be converted to quasi-dc components after the sampling. As a result, the quasi-dc components cause large estimation errors.

3.5.4 Frequency ramp test

The reference signal is $\mathrm{s(t)} = 1\cos(2\pi(59.5 + 0.5t)t)$, in which the frequency ramps from 59.5 Hz to 60.5 Hz at a rate of 1Hz/s. The testing results are shown in Figure 3.21, and it can be seen that the frequency estimation error is less than 1 mHz. The angle error is interesting, and we can see the angle error has a dc component that is about 0.12 degree. Unfortunately, the dc offset error is unwanted and it is not easy to compensate.

3.5.5 Magnitude modulation test

The reference signal is $\mathrm{s(t)} = (1 + k_m \cos(2\pi f_m t)) * \cos(2\pi 60t)$, where k_m is modulation index, and f_m is modulation frequency. k_m is equal to 0.1 in this test, and $f_m$increases from 1 to 5 Hz at a step of 1Hz. The testing results are shown in Figure 3.22, we can see the FDR algorithm has good accuracy under this condition. The maximum angle error is about 0.025 degree, and the maximum frequency error is about 0.6 mHz.

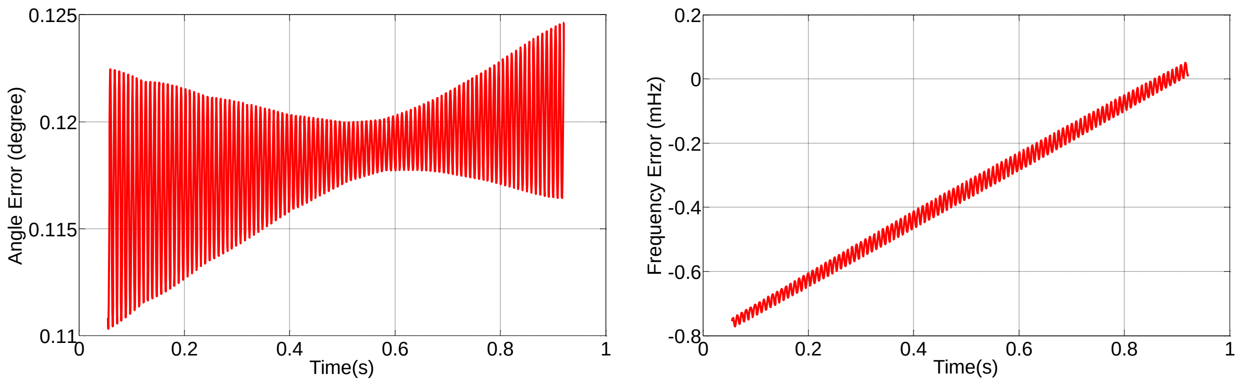

(a). Angle error (b). Frequency error

Figure 3.21 Frequency ramp test

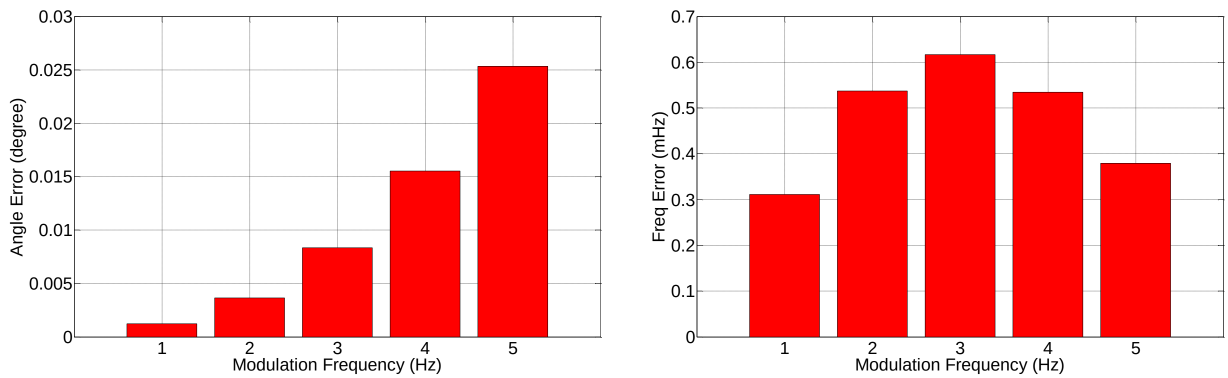

(a). Angle error (b). Frequency error

Figure 3.22 Magnitude modulation test

3.5.6 Phase modulation test

The reference signal is $s(t) = 1\cos(2\pi 60t + k_a \cos(2\pi f_a t - \pi))$, where k_a is modulation index, and f_a is modulation frequency. k_a is equal to 0.1, and f_a increases from 1 to 5 Hz at a step of 1Hz in this test. The testing results are shown in Figure 3.23. Compared to magnitude modulation test, the angle and frequency errors under this condition are much larger. The maximum angle error is about 1.6 degree, and the maximum frequency error is about 120 mHz when the modulation frequency is 5 Hz. Considering 5 Hz modulation frequency is not very common in large-scale power grid and most of modulation frequencies are less than 2 Hz. The FDR algorithm under 2 Hz modulation frequency has 0.3 degree angle error and 8 mHz frequency error, which are still rather large.

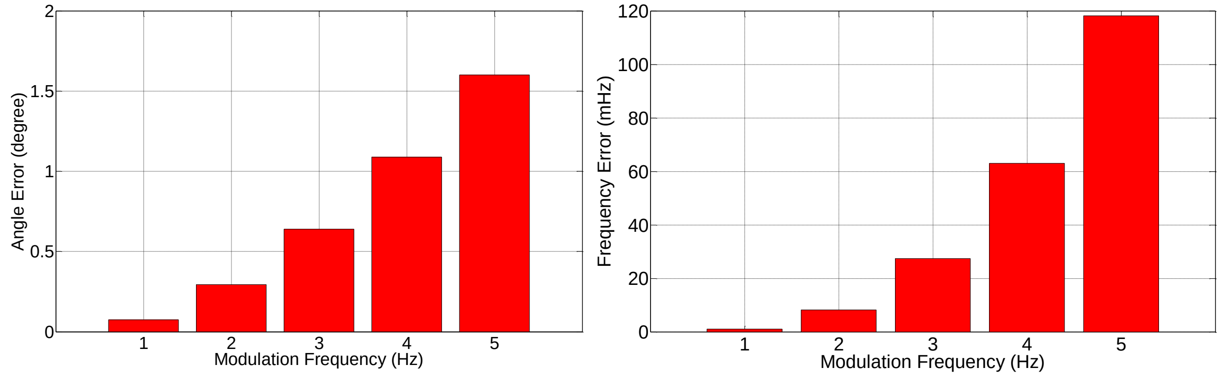

(a). Angle error (b). Frequency error

Figure 3.23 Phase modulation test

3.6 Conclusion

In this chapter, the error sources of FDRs including GPS and ADC were analyzed. According to the discussion, the hardware of the FDRs was upgraded to achieve better sampling accuracy by using a 16-bit ADC instead of 14-bit ADC. Additionally, the effect of the noise on estimation accuracy was analyzed, and a digital averaging filter was proposed to filter the noise in the power grid signal. The test shows that the effect of noise on frequency and angle estimation error can be greatly reduced by the digital filter.

Next, the angle and frequency estimation accuracy of the FDR algorithm were evaluated under different steady-state and dynamic conditions following PMU Standard including frequency range condition, harmonic distortion condition, frequency ramp condition, magnitude modulation, and phase modulation condition. In addition, harmonic distortion under off-nominal frequency condition, which is beyond the PMU Standard is also tested on FDR algorithm. We can draw the following conclusions based on the tests:

1) The FDR algorithm has good accuracy under frequency range, harmonics under nominal frequency condition, and magnitude modulation conditions.
2) Under 1Hz/s frequency ramp condition, the frequency estimation is rather accurate, but there is dc offset error for angle, and it is not easy to compensate.
3) For harmonic distortion under off-nominal frequency condition,
    a) Overall, the FDR algorithm is not immune to the harmonics, and the errors increase with the increase of magnitude of harmonics.

b) The FDR algorithm is especially sensitive to the harmonics of order around 25i (i=1, 2,…) due to aliasing issue.

4) Under phase modulation condition, the FDR algorithm performs well if the modulation frequency is less than 1 Hz, and the estimation errors increase dramatically with the increase of modulation frequency, so it is necessary to reduce the estimation errors under this condition.

Chapter 4 A New DFT-based Angle and Frequency Estimation Algorithm

According to the analysis in Chapter 3, the FDR algorithm is not accurate enough under some conditions. A new method to estimate phase angle and frequency at distribution level under both steady state and dynamic conditions is presented in this chapter. The discrete Fourier transform (DFT)-based method is widely used for phasor and frequency estimation thanks to its low computational burden. However, errors arise when the power system is operating at the following conditions:

1) Off-nominal frequency condition: the fundamental frequency deviates from nominal frequency (60 Hz for U.S. power grid).
2) Harmonic distortion condition when the fundamental frequency deviates from nominal frequency.
3) Dynamic conditions: frequency ramp, magnitude modulation, and phase modulation.

In this chapter, the distortion of the power grid signals at the distribution level will be analyzed in frequency domain first. Then, based on the distortion analysis, Phasor estimation model in the PMU Standard [26] is employed to study the effect of the distortion on phasor measurement accuracy. Next, to improve phasor measurement accuracy at the distribution level, a new phasor estimation algorithm that is based on the phasor model in the Standard is proposed. Moreover, the proposed algorithm will be assessed under various tests in the PMU Standard to verify its performance.

4.1 Distortion analysis of power grid signals at the distribution level

4.1.1 Distortion of power grid signals at the distribution level

IEEE PMU Standards (C37.118.1-2011, C37.118.1a-2014) have been used for PMU design and testing, and different steady-state and dynamic tests are required in the Standard [26], [27]. However the PMU standard is for transmission level power systems, so the application of PMU standard at the distribution level must be examined closely.

In order to study this, the power grid waveforms at the distribution level are collected. Figure 4.1 shows the power spectral density of a real power grid waveform collected at the distribution level and an ideal power grid waveform, respectively. We can see that both the waveforms have the fundamental frequency component, which is close to 60 Hz. However for the real power grid waveform, it is distorted by harmonics as expected. More importantly, the real power waveform is also distorted by noise.

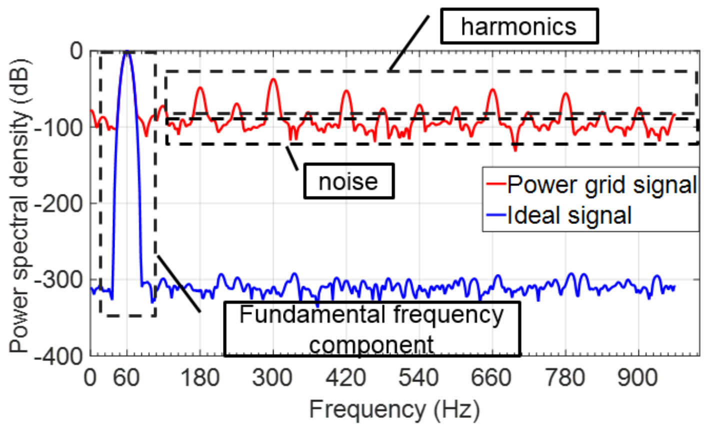

Figure 4.1 Power spectral density of a real and an ideal power grid waveform

4.1.2 Noise and harmonics analysis

A 16-bit angle-to-digital converter (ADC), which theoretically has 98.08 dB signal to noise (SNR), is used to collect power grid signals at the distribution level with 61.44 kHz/s sampling rate. Considering the power grid frequency may deviate from nominal frequency, the modified periodogram method is adopted to calculate power spectral density (PSD) of the power grid signal. The equation used to calculate PSD is

$$P_{xx}\left(\frac{k}{N}\right) = \frac{1}{N}\left|\sum_{N=0}^{N-1} h(n)x(n)e^{-j2\pi nk/N}\right|^2, \quad k = 0, 1, \dots, N-1 \tag{4.1}$$

where $P_{xx}\left(\frac{k}{N}\right)$ is the power of the signal component at bin $\frac{k}{N}$; N is the window size of the modified periodogram method; $x(n)$ is the sample of the power grid signal; $h(n)$ is the coefficient of the window, and Kaiser window where $\beta = 38$ is used. $h(n)$ can be computed by

$$h(n) \triangleq \begin{cases} \dfrac{I_0\left(\beta\sqrt{1-\left(\dfrac{n}{\frac{N}{2}}\right)^2}\right)}{I_0(\beta)}, & -\dfrac{N-1}{2} \leq n \leq \dfrac{N-1}{2} \\ 0 & \end{cases} \tag{4.2}$$

where I_0 is the zeroth order Modified Bessel function of the first kind. The frequency resolution of the modified periodogram is f_s/N.

Figure 4.2 (a) shows the PSD of the measured signal from 0 Hz to 3 kHz. The power of fundamental frequency component is normalized to 0 dB; then, the power of other frequency components becomes negative in dB. We can see that the measured signal contains harmonics as expected. More importantly, the measured signal also contains noise. The signal-to-noise ratio of the power grid signal is defined by

$$SNR = \frac{P_{signal}}{P_{noise}} \tag{4.3}$$

where P_{signal} is the power of the fundamental frequency component in the measured signal, and P_{noise} is the power of the noise, which includes all the frequency components except the fundamental frequency component and harmonic components. According to the definition, the SNR of the measured signal can be calculated, which is 62.4 dB.

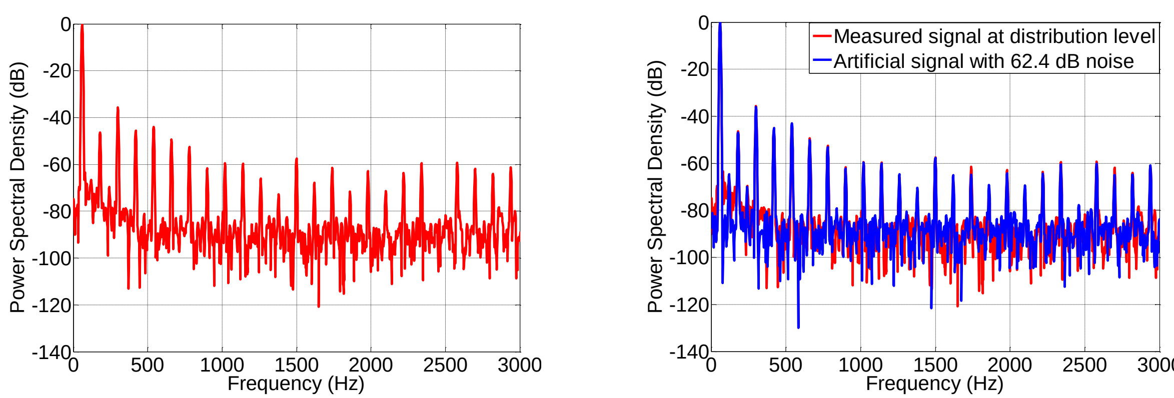

(a). Measured signal (b) Measured signal and artificial signal

Figure 4.2 PSD of measured signal and artificial signal

To further verify the estimation accuracy of SNR, an artificial signal consisting of a 0 dB fundamental frequency component, a 62.4 dB noise, and the same amount of harmonics as the measured signal is generated. Figure 4.2 (b) shows the PSD of the artificial signal and the measured signal together, and we can see that the PSD of the two signals match each other. This verified the estimation accuracy of the measured signal's SNR.

According to the PSD analysis of the measured power grid signal at the distribution level, we can see that this signal contains noise and harmonics. However, the PMU Standard has no requirements under noise condition. Additionally, although the Standard has harmonic distortion test, it assumes that the fundamental frequency is equal to nominal frequency, which is not true for practical applications. Therefore, to measure the phasor at the distribution level accurately, considering only the test conditions in the PMU Standard is not enough.

4.1.3 Distribution probability of frequency of U.S. power grid

Using the frequency measurement data collected by FDRs deployed in the U.S. power grid, the distribution probabilities of frequency of the US power grid from 2005-2013 are plotted for the Eastern Interconnection (EI) and the Western Interconnection (WECC) in Figure 4.3 [34]. It shows that the power system frequency is mainly distributed from 59.95 Hz to 60.05 Hz. Since the fundamental frequency deviates from 60 Hz in most of the time, frequency of the harmonic components is not equal to integer multiples of 60, but integer multiples of this frequency range.

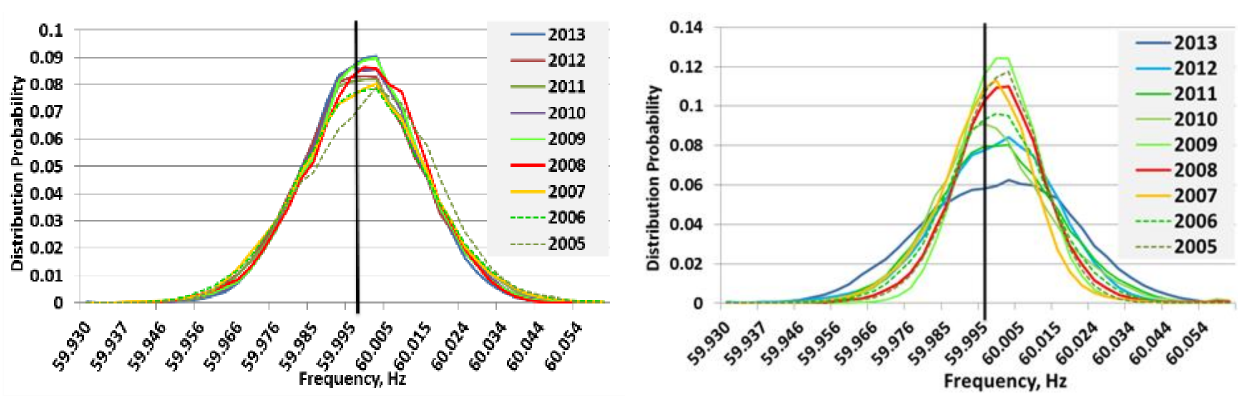

(a) EI (b) WECC

Figure 4.3 Frequency probability distribution for EI and WECC, 2005 to 2013

4.1.4 Summary

Based on the analysis, we can see that the power grid signals at the distribution level are distorted by both harmonics and noise, and the fundamental frequency deviates from nominal value in most of the time. Unfortunately, the PMU Standard has no requirements for the measurement accuracy when the power grid waveforms are distorted by noise. As a result, it could lead to unexpected phasor measurement errors due to noise.

Additionally, although PMU Standard has requirement for harmonic distortion test, but it assumes that the fundamental frequency is equal to 50/60Hz, which is not true for practical applications. Moreover, only one order of harmonic component is required in the PMU Standard. In contrast, the real power grid waveforms are distorted by multiple harmonic components. Therefore, to better evaluate the measurement accuracy of a PMU algorithm in a real power grid environment, the measurement accuracy needs to be tested under multiple harmonic components condition. In next section, the phasor model in the PMU Standard will be evaluated under those conditions [26].

4.2 Testing of phasor model in the PMU Standard

4.2.1 Phasor model in the PMU Standard

The phasor model for M-class PMUs described in Annex C in PMU Standard [26] is used for testing, which is given by

$$X(i) = \frac{\sqrt{2}}{Gain} \times \sum_{k=-\frac{N}{2}}^{\frac{N}{2}} x_{(i+k)} \times W_{(k)} \times exp(-j(i+k)\Delta t \omega_0 \tag{4.4}$$

where $W_{(k)}$ is the coefficient of the low-pass filter and can be calculated by the following equation,

$$W_{(k)} = \frac{sin\left(2\pi \times \frac{2F_r}{F_s} \times k\right)}{2\pi \times \frac{2F_r}{F_s} \times k} \times h(k) \tag{4.5}$$

The number samples for phasor estimation, which is N, and the low pass filter $W_{(k)}$ is different for different reporting rates. Therefore, the measurement accuracy under different reporting rates need to be tested.

4.2.2 Noise test

Figure 4.4 (a) shows the angle errors under different noise level conditions. The horizontal axis represents the reporting rates, and the vertical axis represents the angle error in degree. We can see that the errors increase with the increase of noise level. The maximum angle error is 0.15 degree under 50dB noise condition. Additionally, we can see that the errors increase with the increase of reporting rate. The errors are much lower for low reporting rates. However, if we see Table 4.1, which shows the response time and number of fundamental cycles for phasor estimation under different reporting rate Fps, we can see that response time is much higher for low reporting rate. Taking 10Hz reporting rate as an example, the phasor estimation window is about 60.6 cycles, which is longer than 1 second, and the response time is about 0.7 second. Therefore, we can see that the measurement accuracy under noise condition is at the expense of response time. Figure 4.4 (b) shows the magnitude errors, and we can draw the same conclusion. The maximum magnitude error is about 0.3% under 50 dB noise condition.

Table 4.1 Response time and estimation windows for different reporting rates

Fps	10	12	15	20	30	60	120
Response time	0.7s	0.58	0.47	0.35	0.23	0.12	0.06
No. of cycles	60.6	51.1	41.4	31.4	19.2	10.3	4.4

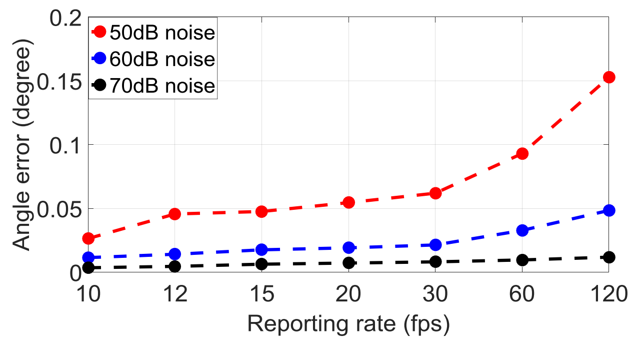

(a). Angle error

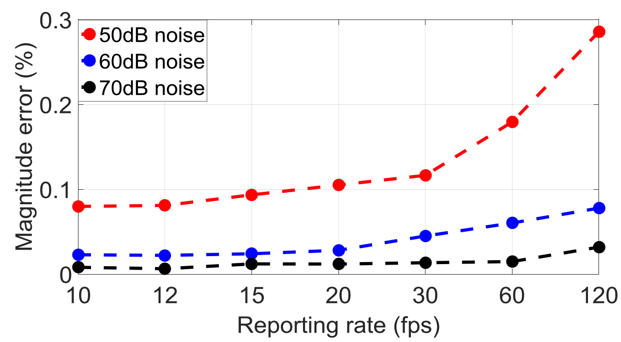

(b). Magnitude error

Figure 4.4 Noise rejection test of PMU phasor model in the Standard

In order to explain this, we need to look into the phasor estimation equation (4.4), $W_{(k)}$ is the low-pass filter, and it is different for different reporting rates. Figure 4.5 shows the frequency response of $W_{(k)}$ for different reporting rates. We can see that they are different for different reporting rates, particularly in the low frequency range, which is usually called "main lobe". As shown in Figure 4.5 (b), the main lobe width increase with the increase of reporting rate. From the signal processing point of view, higher main lobe width means less reduction of noise. This is the reason that the noise rejection performance is worse with the increase of reporting rate.

Besides the low-pass filter used in the PMU Standard, other windows are also tested and compared with the low-pass filter window used in equation (4.4). Figure 4.6 shows the angle and magnitude errors for different types of filter windows under 60dB noise condition, it is interesting that the filter window in the PMU Standard has worst noise rejection performance, and the rectangular window has the best noise rejection performance. The reason can also be explained by looking into the frequency response of different windows, which is shown in Figure 4.7. We can see that the rectangular window has narrowest main lobe width, and the filter window in the PMU Standard has widest main lobe width. As a result, rectangular window has best noise rejection performance, and the filter window in the PMU Standard has worst noise rejection performance.

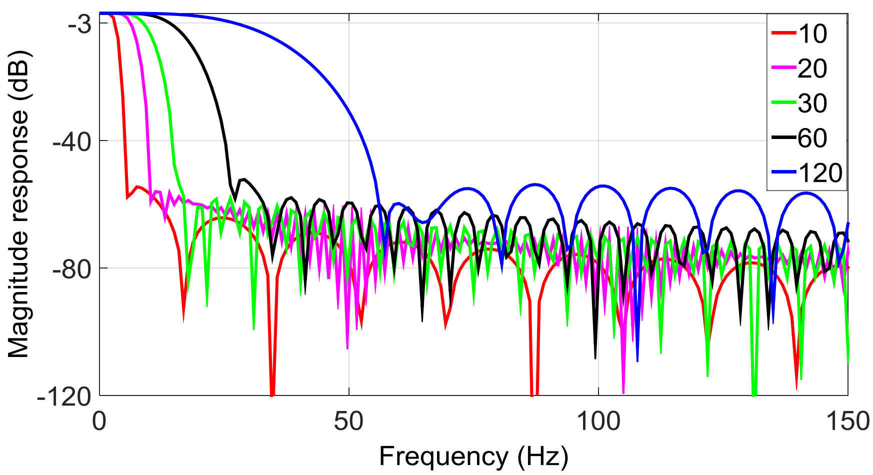

(a). Frequency response

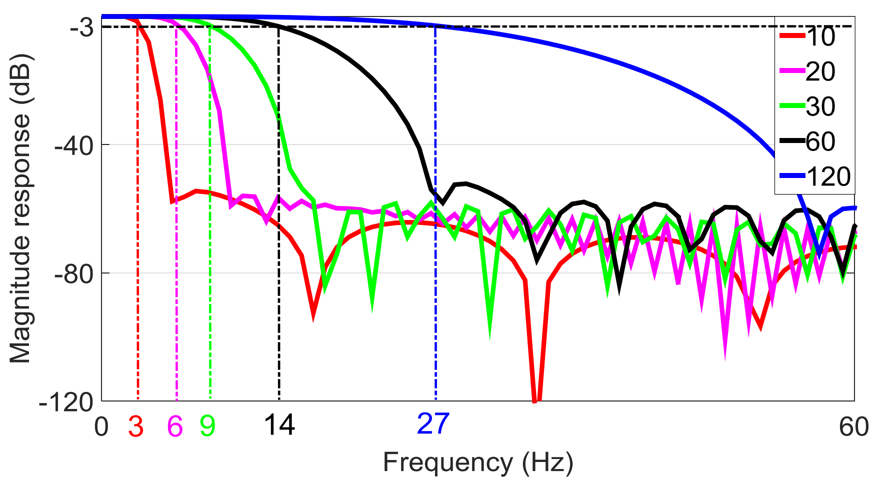

(b). Main lobe

Figure 4.5 Frequency response of $W_{(k)}$

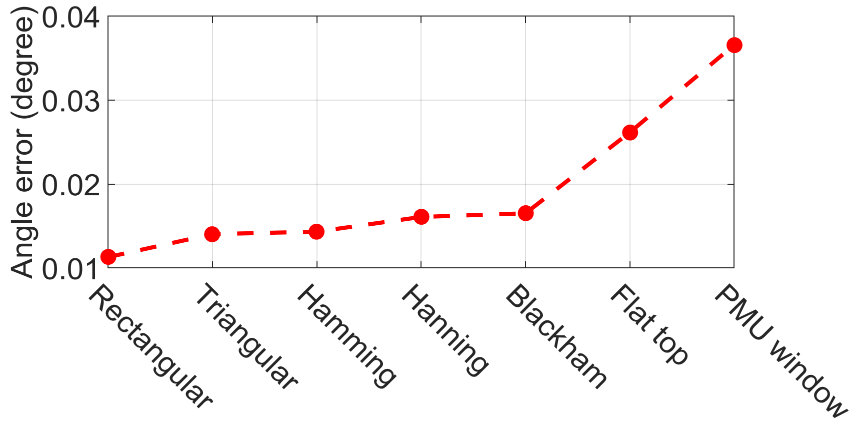

(a). Angle error

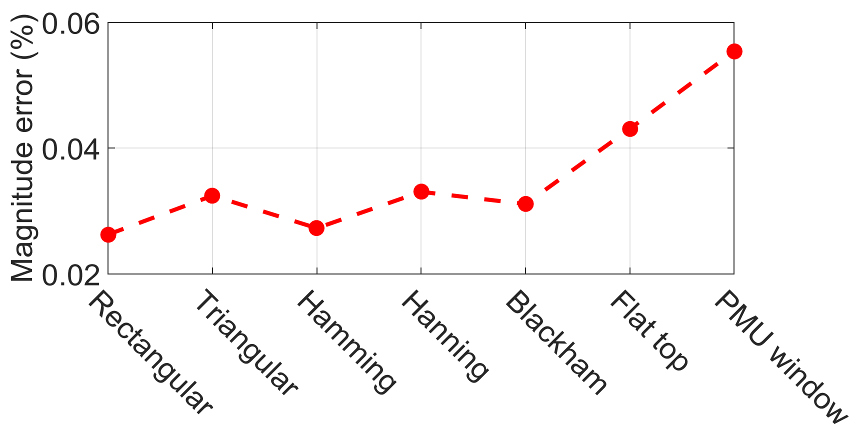

(b). Magnitude error

Figure 4.6 Filter window in the PMU Standard v.s. other windows

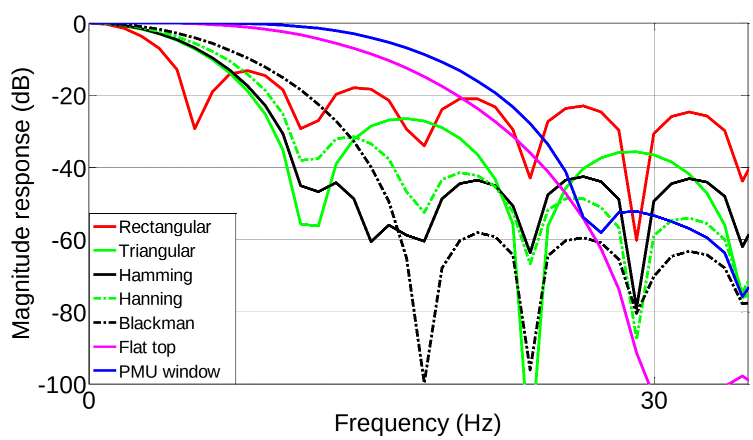

Figure 4.7 Frequency response of different filters

4.2.3 Harmonic distortion test

Besides the noise test, the effect of harmonics on measurement accuracy was also studied. The harmonic distortion test is different from the harmonic distortion test in the PMU Standard in terms of:

1) Fundamental frequency is not equal to nominal frequency;

2) Multiple harmonic components are added, not only individual harmonic component;

3) Harmonics levels are determined by field measurements.

Figure 4.8 shows the angle and magnitude errors. First, we can see that the errors increase with the increase of order of harmonics. The maximum angle and magnitude error is about 0.15 degree and 0.3%, respectively. Additionally, we can see that the errors are close to each other for different reporting rates.

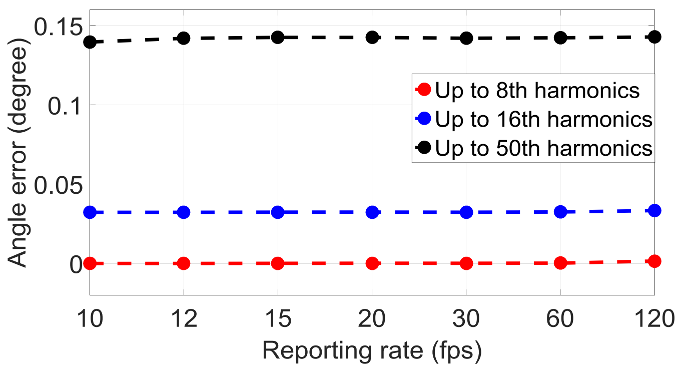

(a). Angle error

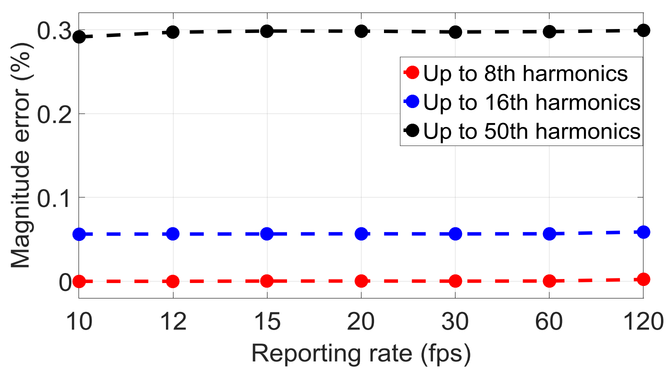

(b). Magnitude error

Figure 4.8 Harmonic distortion test

The results can also be explained by looking into the frequency response of the low-pass filters. Since we are concerned about harmonics rejection performance now, we need look into the frequency response in high frequency range, which is called “side lobe”. As shown in Figure 4.9, we can see that filter for different reporting rates have similar side lobe shape. This can explain that the errors for different reporting rate are close to each other. Moreover, the attenuation of one filter to different harmonic component is close to each other, so the errors increase with the increase of order of harmonics.

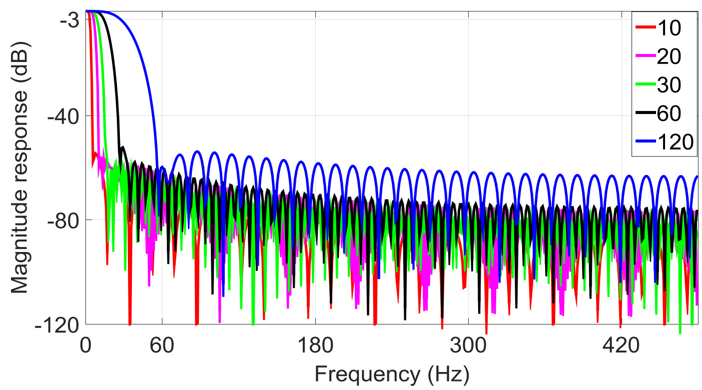

Figure 4.9 Frequency response of the filters in the PMU Standard

4.2.4 Summary

According to the analysis, real power grid waveforms are distorted by noise and harmonics. However, the PMU Standard does not have accuracy requirement under noise condition, and it leads to the worse noise rejection performance of the phasor model in the PMU Standard. This can also be concluded from the comparison between the filter in the PMU Standard and other filters. Therefore, the measurement accuracy of phasor model in the Standard under noise condition needs to be further improved. Moreover, for the harmonic distortion test, we can also see the effect of harmonics on the measurement accuracy cannot be ignored, and further error mitigation method is necessary to improve the harmonics rejection performance. In the following section, a new DFT based phasor estimation method is presented and tested in different conditions to verify it performance.

4.3 Avg_Avg2Comp DFT algorithm

4.3.1 Introduction and background

The DFT-based method is one of the most common algorithms for phasor and frequency estimation. The classic DFT-based synchrophasor measurement algorithm has a low computational burden, but the accuracy of this method degrades at the presence of frequency offsets and under dynamic conditions such as phase modulation [36]-[38]. Alternative DFT-based methods have been proposed to improve the measurement accuracy under steady-state and dynamic conditions [7], [39]-[44]. The quasipositive-sequence DFT (Qps-DFT) method, utilized by FDRs, synthesizes virtual *abc* three-phase data using one-phase data to improve accuracy under off-nominal frequency condition [7]. An adaptive complex band-pass filter derived from the exponentially modulated filter bank theory has been proposed for wide frequency range measurement [39], [40]. A finite-difference equation of multiple one-cycle DFTs for estimating the first- and second-order derivatives of the phasor to reduce the error under modulation conditions has also been proposed [41]. Accuracy analysis of different methods including Finite Impulse Response (FIR) band-pass filtering, extended Kalman filtering, and DFT demodulation with FIR low pass smoothing has been discussed [42]. Aside from DFT-based methods, some dynamic signal models have been proposed to improve the accuracy under dynamic conditions [45]-[47]. According to the analysis in [48], [49], the algorithm in [47] outperforms those presented in [45]-[46] under dynamic conditions. However, the performance of signal model-based methods have not been well assessed under noise or harmonic conditions and where they have shown some room for improvement in the area of synchrophasor measurement.

It should be noted that previous algorithms focused on the synchrophasor measurement at the transmission level rather than the distribution level. The signals at the distribution level generally contain more noise and harmonics, and are generally single phase. Therefore, as discussed in 4.2, the IEEE PMU Standard cannot be easily applied to the distribution level synchrophasor measurements. Since the Standard does not have a measurement accuracy requirement under noise condition, and this could be a challenge for synchrophasor measurement algorithms because improvement of noise rejection performance of synchrophasor measurement algorithms is generally at the expense of worse dynamic performance. The Qps-DFT algorithm [7] is used to estimate phasor and frequency of single phase signals in FDRs at the distribution level. However, the Qps-DFT algorithm assumes the power grid signal is a steady-state signal, so its accuracy has not been well discussed under different dynamic conditions specified in the PMU Standard.

Therefore it is necessary to develop a synchrophasor measurement algorithm that is suitable for use at the distribution level. Based on the noise and harmonics analysis results and the PMU Standard, a new DFT-based algorithm is proposed to estimate phase and frequency under noise, harmonics, and other conditions in the PMU Standard. The proposed algorithm is then compared to the Qps-DFT algorithm following different test conditions. The measurement accuracy of the proposed synchrophasor measurement algorithm will not only be assessed according to the PMU Standard, but also under noise and harmonic conditions in the presence of frequency offsets.

4.3.2 Proposed phase and frequency measurement algorithm

NOMENCLATURE

f_0	Nominal power system frequency (in hertz)
f	Actual power system frequency (in hertz)
T_0	Nominal frequency cycle ($T_0 = 1/f_0$)
f_{samp}	Sampling rate
N_s	Oversampling ratio of averaging filter

The flowchart of the proposed algorithm is shown Figure 4.10. The proposed algorithm consists of six modules: Noise Reduction Module (NRM); Phase Estimation Module (PEM); Even Multiples of Fundamental Frequency Error Reduction Module (EFFERM); Odd Multiples of Fundamental Frequency Error Reduction Module (OFFERM); Phase Modulation Error Reduction Module (PMERM); and Frequency Estimation Module (FEM).

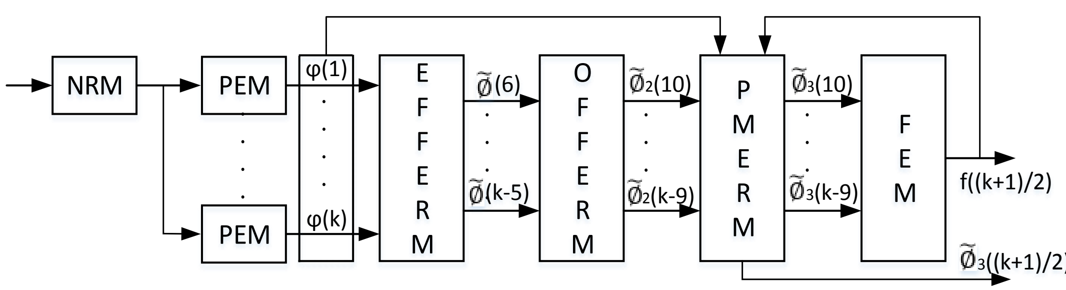

Figure 4.10 Flowchart of Avg_Avg2Comp DFT algorithm

Since NRM, EFFERM, and OFFERM use an averaging method to reduce the errors, and PMERM uses the coefficient of a polynomial function to compensate phase errors, the proposed algorithm is called "Avg_Avg2Comp DFT".

A. NRM

The NRM employs the digital averaging filter presented in 3.2.2. The filter can reduce the noise while it does not affect the measurement accuracy under noise free condition.

B. PEM

The basic phase estimation model for M-class PMUs, as described in Annex C in PMU Standard, is used in PEM and is given in Annex C.2 in the PMU Standard [26],

$$X(i) = \frac{\sqrt{2}}{\sum_{k=-N/2}^{N/2} W_{(k)}} \times \sum_{k=-\frac{N}{2}}^{\frac{N}{2}} x_{(i+k)} \times W_{(k)} \times exp(-j(i+k)\Delta t\omega_0) \qquad (4.6)$$

where $x(i)$ is the sample of the waveform at time $= i\Delta t$; $exp(-j(i+k)\Delta t\omega_0)$ is Euler's equation; and $W_{(k)}$ are the low-pass filter coefficients and can be calculated by the equation (C.7) in the Standard [26].

The low-pass filter in (4.6) can improve phasor estimation accuracy under off-nominal frequency condition by increasing the main lobe width of the DFT window, and can reject out-of-band signals more effectively by lowering the side lobe levels. However, the improvement is at the expense of longer latency and worse estimation accuracy under noise and nominal-frequency conditions. The input signal in this model is convolved with quadrature waveforms at nominal frequency f_0. The ideal output of (4.6) is a fundamental phasor, which has a magnitude proportional to the voltage, and a phase angle, which rotates at a rate of $2\pi(f - f_0)$. Since the power grid signals always contain harmonics and may contain dynamic components when the power grid suffers events, this model has two problems. First, the output of (4.6) not only contains a wanted phasor component that rotates at a rate of $2\pi(f - f_0)$, but also contains an unwanted phasor component that rotates a rate of $2\pi(f + f_0)$ for the fundamental frequency component, $2\pi(if - f_0)$ and $2\pi(if + f_0)$ components for i-th order of harmonic component [50]. For example, the phase angle of an artificial signal that has a 59.5 Hz fundamental frequency component and the same amount of harmonics as the measured signal in Figure 4.2 is calculated by (4.6). Figure 4.11 (a) shows the phase angle estimation errors and Figure 4.11(b) shows the frequency spectrum of the errors. We can see the frequencies of the main errors are close to 60 Hz, 120 Hz, 180Hz, 240 Hz, etc. As a result, the main errors can be divided into two categories: even multiples of fundamental frequency errors with a frequency close or equal to $2if_0$ $(i = 1, 2, \ldots,)$; odd multiples of fundamental frequency errors with a frequency close or equal to $(2i + 1)f_0$ $(i = 0,1, 2, \ldots,)$.

Second, the power grid signals may contain dynamic components such as phase modulation. Figure 4.12 (a) and (b) show the angle errors under 5 Hz modulation condition in time domain and frequency domain, respectively. According to Figure 4.12(b), we can see two errors. The frequency of one error is 5 Hz, which is equal to modulation frequency. The frequency of the other error is close to 120 Hz because the fundamental frequency deviates from 60 Hz under phase modulation condition.

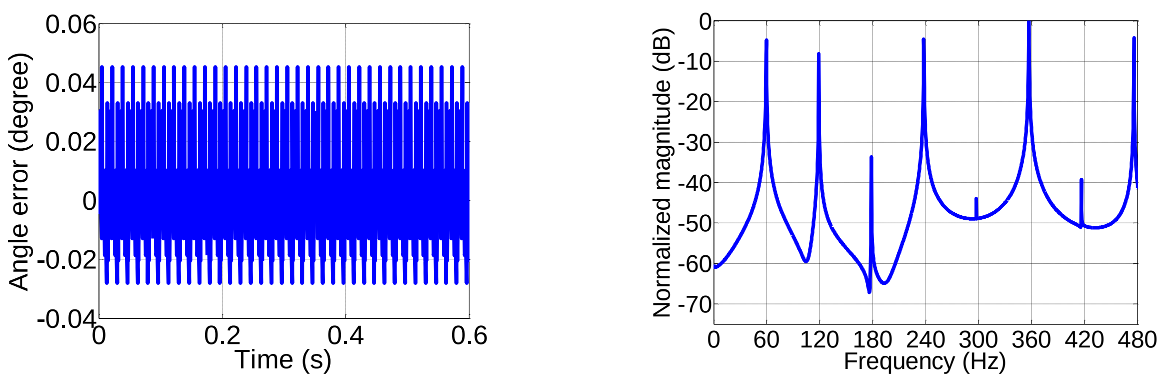

(a). Angle error in time domain (b). Angle error in frequency domain

Figure 4.11 Angle errors under off-nominal frequency and harmonic conditions

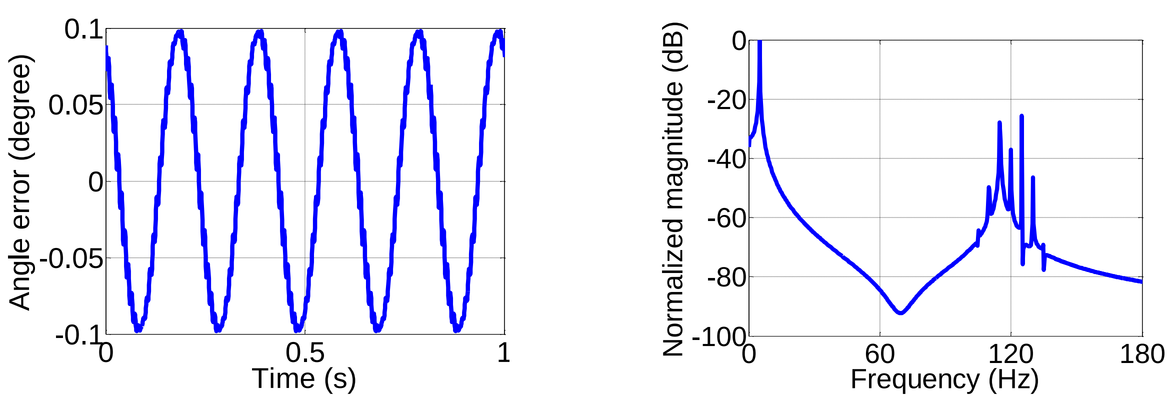

(a). Angle error in time domain (b). Angle error in frequency domain

Figure 4.12 Angle errors under phase modulation condition

Based on the analysis, the main errors are divided into three groups according to the frequency of the errors.

1) Even multiples of fundamental frequency errors: The frequency of the errors is close or equal to $2if_0,\ i = 1, 2, \ldots$
2) Odd multiples of fundamental frequency errors: The frequency of the errors is close or equal to $(2i + 1)f_0,\ i = 0, 1, 2, \ldots$.
3) Low frequency errors: Under phase modulation condition, the frequency of the main errors is equal to modulation frequency.

The first two errors can be reduced by increasing the main lobe width of the DFT window [51], but is at the expense of worse noise rejection. To reduce the two errors, the ideal low-pass filter should have notches at corresponding frequencies and have a flat top response from 0 to $|f - f_0|$ Hz. However, it is impossible to implement such a filter because f cannot be estimated precisely. Some adaptive filters have been proposed to adjust the filter coefficients using f as the feedback for filter coefficient calculations [39], [52], [53], and some commercialized PMUs have tried to implement adaptive filters. Although the adaptive filter offers a good performance under off-nominal frequency condition, the algorithm complexity is high since the filter coefficients need to be calculated in real time. More importantly, the adaptive filters have been rarely tested under various dynamic conditions such as frequency ramp and amplitude/phase modulation. As revealed in the NIST PMU Inter Laboratory Comparison (ILC) project, a commercial PMU was tested under frequency ramp condition, and the adaptive filter caused frequency oscillation [54]. Additionally, the effect of adaptive filters on the third type of errors was rarely discussed. Therefore, the robustness and accuracy of adaptive filters under dynamic conditions needs further assessment.

Instead of the adaptive filters method, the three errors are reduced by EFFERM, OFFERM, and PMERM, respectively. The basic idea is to reduce the first two errors by applying digital filters to a series of angles calculated by PEM, then to reduce the third type of errors by PMERM.

C. EFFERM

EFFERM is used to reduce the first errors. Assuming angle measurement error is $\delta(t)$. Since the frequency of the errors is close or equal to $2if_0$, $i = 1, 2, \ldots$, so we have

$$\begin{cases} \delta(t) \cong \delta(t + \frac{1}{2if_0}) \\ \delta(t) \cong -\delta(t + \frac{1}{4if_0}) \end{cases} \tag{4.7}$$

In practical implementation, the angles have to be calculated in discrete domain. Because the minimum frequency of the angle errors is about $2f_0$, the minimum angle estimation rate should be $4f_0$ in order to apply any filter to reduce the errors. In the proposed algorithm, $8f_0$ angle estimation rate is used to achieve better filter performance. As a result, the angles are calculated as follows:

$$\varphi(k) = PEM(\frac{\mathrm{T}_0}{8}(k-1), \frac{\mathrm{T}_0}{8}(k-1) + 2\mathrm{T}_0) \tag{4.8}$$

where $\varphi(k)$ is the kth angle estimated by the PEM module. The first angle $\varphi(1)$ is estimated using the first two fundamental frequency cycle data [0, $2\mathrm{T}_0$], and the following angles are estimated by sliding the PEM window by 1/8 fundamental frequency cycle ($\mathrm{T}_0/8$). Assuming the estimation error of $\varphi(k)$ is $\delta(k)$ and the true value of $\varphi(k)$ is $\emptyset(k)$, then we obtain

$$\varphi(k) = \emptyset(k) + \delta(k) \tag{4.9}$$

A series of angles $\varphi(k)$ is used to approximate $\emptyset(k)$,

$$\widetilde{\emptyset}(k) = \sum_{i=1}^{N_1} E_i \varphi\left(i + (k - \frac{N_1}{2})\right), \qquad k \geq \frac{N_1}{2} \tag{4.10}$$

where N_1 is the number of angles used for estimating $\emptyset(k)$ and E_i is the coefficient of the filter. The derivation of the filter coefficients is presented in Appendix A. Since the minimum frequency of the errors is close or equal to $2f_0$ and the angle estimation rate is $8f_0$, N_1 is equal to 12 if a three cycle-filter is used to estimate $\emptyset(k)$.

The frequency response of the filter is shown in Figure 4.13. We see the filter has notches at $2if_0$ Hz, which means that the errors at these frequencies can be greatly reduced. The filter is actually a flat top window filter since the window is a partially negative-valued window as indicated in Appendix A. This type of filter is beneficial for measuring phasor since the wanted signal components are in low-frequency range, and the unwanted signal components are in high frequency range and close to the even multiples of fundamental frequency.

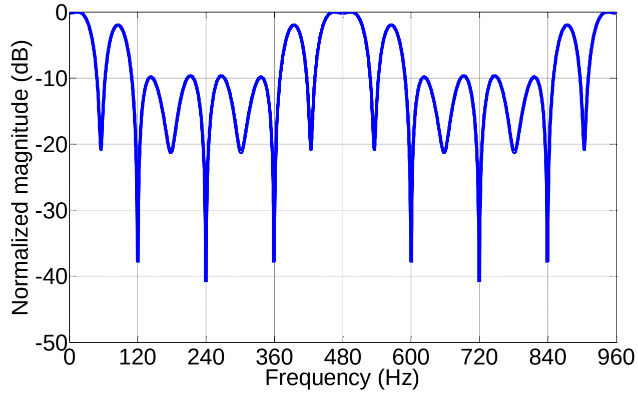

Figure 4.13 Frequency response of EFFERM filter

Note that the filter does not have notches at $8if_0$, $i \geq 1$. The reason is that the angle estimation sliding window is $T_0/8$, which means that angles are "sampled" from the continuous angles at a rate of $8f_0$ Hz. According to Nyquist-Shannon sampling theorem, if the frequency of the errors is integer multiples of $8f_0$, then the errors are transferred to DC component. As a result, the magnitude response of the filter at $8if_0$ is 0 dB. That is the reason why the angle measurement errors of the proposed algorithm under 7th and 9th harmonic condition are more obvious than other harmonic conditions as shown in Figure 4.18. However, the errors are still very small and less than Qps-DFT algorithm.

D. *OFFERM*

Figure 4.13 shows that the filter in EFFERM has good attenuation at $2if_0$ Hz, but does not have enough attenuation at $(2i{+}1)f_0$ Hz. Therefore, OFFERM is designed to reduce those $(2i{+}1)f_0$ Hz errors in the output angles from EFFERM. We assume

$$\widetilde{\emptyset}(k) = \sum_{i=1}^{N_1} E_i \varphi\left(i + (k - \frac{N_1}{2})\right), \qquad k \geq \frac{N_1}{2} \tag{4.11}$$

where $\varepsilon(k)$ is the error of $\widetilde{\emptyset}(k)$. For sake of simplicity, assuming $\widetilde{\emptyset}(k)$ does not have the first type of errors and the frequency of the errors is close or equal to $(2i{+}1)f_0$, we obtain

$$\varepsilon(k) \cong -\varepsilon(k+4) \cong \varepsilon(k+8) \tag{4.12}$$

As a result, the error of $\widetilde{\emptyset}(k+4)$ can be further reduced by using $\widetilde{\emptyset}(k)$, $\widetilde{\emptyset}(k+4)$, and $\widetilde{\emptyset}(k+8)$

$$\widetilde{\emptyset}_2(k+4) = \sum_{i=0}^{2} F_i \widetilde{\emptyset}(k+4i)\,, k \geq \frac{N_1}{2}k \tag{4.13}$$

where $\widetilde{\emptyset}_2(k+4)$ is a further estimation of $\emptyset(k+4)$ and F_i is the coefficient of the filter, which is derived in Appendix A.

The frequency response of the filter is shown in Figure 4.14, and we can see the filter has notches at $(2i{+}1)f_0$ Hz, which means that those errors can be reduced by this filter.

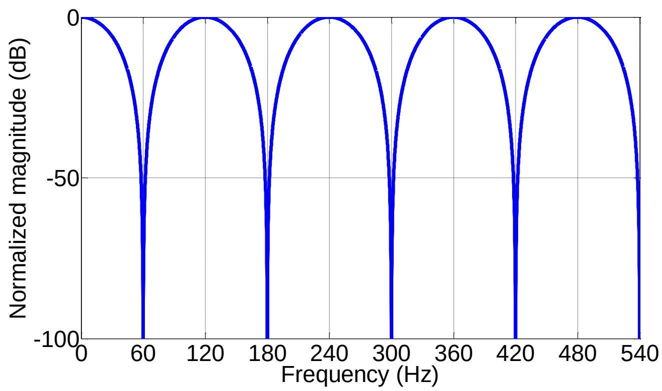

Figure 4.14 Frequency response of OFFERM filter

E. PMERM

Figure 4.15 shows the output angles $\widetilde{\emptyset}_2(k+4)$ from OFFERM and the true angle $\emptyset(k+4)$ under phase modulation condition. The differences between $\widetilde{\emptyset}_2(k+4)$ and $\emptyset(k+4)$ are the measurement errors and they are shown in Figure 4.15(b). We can see that the errors are in phase with $\widetilde{\emptyset}_2(k+4)$ and this provides a way to compensate for the errors by using measured angles. Since the low frequency modulation signal can be approximated by a quadratic polynomial in a short time, and the second order coefficient of the polynomial indicates the curvature of the modulated signal, so should there be a relationship between the angle errors and the coefficient.

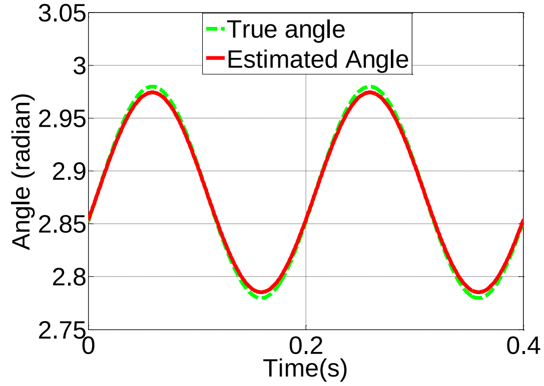

(a). Estimated angle $\widetilde{\emptyset}_2(k+4)$ and true angle $\emptyset(k+4)$

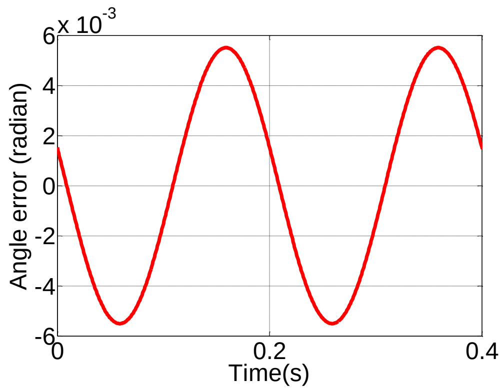

(b). Angle error

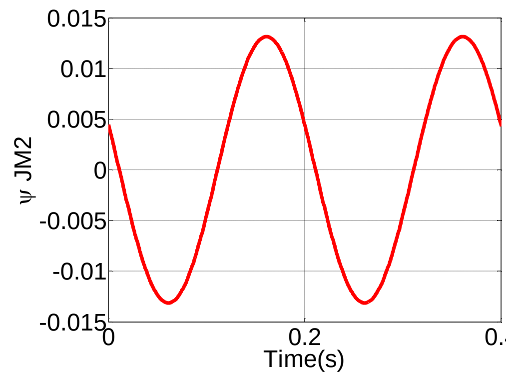

(c). φ_{JM2}

Figure 4.15 Illustration of angle error under phase modulation condition

To verify this, $\varphi(t-T_0)$, $\varphi(t)$, and $\varphi(t+T_0)$ are fitted to a quadratic polynomial, giving us

$$\begin{cases} \varphi(t-T_0) = \varphi_{JM0} + \varphi_{JM1}(t-T_0) + \varphi_{JM2}(t-T_0)^2 \\ \varphi(t) = \varphi_{JM0} + \varphi_{JM1}t + \varphi_{JM2}t^2 \\ \varphi(t+T_0) = \varphi_{JM0} + \varphi_{JM1}(t+T_0) + \varphi_{JM2}(t+T_0)^2 \end{cases} \tag{4.14}$$

where φ_{J0}, φ_{JM1}, and φ_{JM2} are the coefficient of the quadratic polynomial. φ_{JM2} is the second-order coefficient and can be calculated using the least square method. As a result,

$$\varphi_{JM2} = \frac{\varphi(t-T_0) - \varphi(t) + \varphi(t+T_0)}{2} \tag{4.15}$$

φ_{JM2} is shown in Figure 4.15(c). We see that the angle errors are in phase with φ_{JM2}. Meanwhile, the ratio of the angle errors to φ_{JM2} under different modulation frequencies M_F and the modulation index M_I is calculated and summarized in Table 4.2.

Table 4.2 Ratio of the errors to φ_{JM2}

M_I \ M_F	0.5	1	2	3	4	5
0.01	0.4118	0.4120	0.4128	0.4187	0.4296	0.4481
0.02	0.4118	0.4120	0.4128	0.4187	0.4296	0.4480
0.04	0.4118	0.4120	0.4128	0.4188	0.4297	0.4480
0.06	0.4118	0.4120	0.4129	0.4188	0.4298	0.4479
0.08	0.4118	0.4120	0.4129	0.4188	0.4299	0.4479
0.1	0.4118	0.4120	0.4129	0.4188	0.4299	0.4478

We can see the ratios are almost constant under different conditions and this indicates that the angle errors can be compensated with φ_{MJ2} multiplied by a ratio $\boldsymbol{\alpha}$. 0.4478 is used as the ratio, which is the value under 5 Hz modulation frequency and 0.1 modulation index. Then the angles can be compensated by

$$\widetilde{\emptyset}_3(k+4) = \widetilde{\emptyset}_2(k+4) - 0.4478\varphi_{MJ2}, k \geq \frac{N_1}{2} \tag{4.16}$$

where $\widetilde{\emptyset}_3(k+4)$ are the output angles from PMERM.

Note that under off-nominal frequency condition, φ_{MJ2} should be equal to zero since modulation does not exist. However, since the angles from PEM are used to estimate φ_{MJ2}, and those angles have errors under off-nominal frequency condition, φ_{MJ2} is not exactly equal to zero, which will increase the angle and frequency measurement errors under off-nominal frequency condition. To solve this problem, as shown in Figure 4.10, the frequency measurement result is used as a feedback to enable or disable PMERM. According to the PMU Standard C37.118.1-2011, the frequency of the power grid signal under phase modulation condition is within $[f_0 - 0.2, f_0 + 0.2]$. To leave a margin, when the frequency is within $[f_0 - 1, f_0 + 1]$, PMERM is enabled to reduce the estimation errors under phase modulation condition. Otherwise it is disabled to improve the measurement accuracy under off-nominal frequency condition.

F. FEM

Since frequency is the derivative of angle, the output angles from PMERM are fitted to a quadratic polynomial to estimate frequency, which is given by

$$\theta(t) = \varphi_{F0} + \varphi_{F1}t + \varphi_{F2}t^2 \tag{4.17}$$

Then the frequency at $t = 0$ can be calculated by

$$f = \frac{\varphi_{F1}}{2\pi} \tag{4.18}$$

The number of angles used to fit the quadratic polynomial is a tradeoff between measurement accuracy under noise condition and measurement accuracy under dynamic conditions like phase modulation. Generally, more angles will result in better measurement accuracy under noise condition because a longer estimation window can help reduce the noise. However, a longer estimation window will decrease the measurement accuracy under phase modulation condition. Figure 4.16 shows the relationship between the frequency estimation errors and the number of angles used for the frequency estimation under noise condition, and under phase modulation condition, respectively. The reference signal under noise condition is a 60 Hz signal distorted by 60 dB noise, and the reference signal under phase modulation condition is given by

$$s(t) = 1\cos(2\pi f_0 t + k_a \cos(2\pi f_a t - \pi)) \tag{4.19}$$

where k_a is the modulation index, and f_a is the modulation frequency. k_a is equal to 0.1 and f_a is equal to 5.

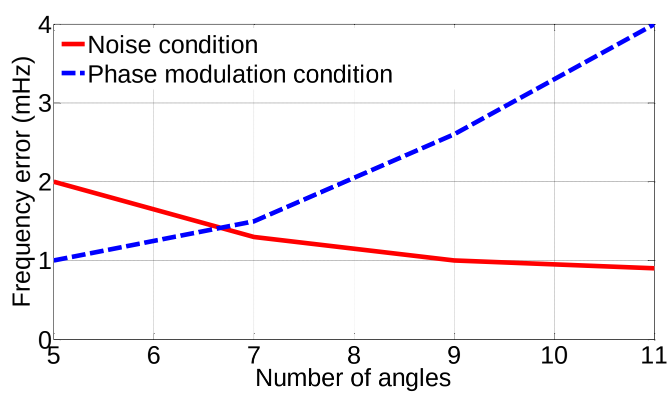

Figure 4.16 Frequency measurement errors relative to number of angles used for frequency estimation

According to Figure 4.16, we can see that when the number of angles is seven, the frequency measurement errors under the two conditions are close to each other. As a result, seven angles are determined in this module to strike a balance between the measurement accuracy under the two conditions. Then, according to Figure 4.10, if seven angles are used, the total number of angles calculated by PEM is 26.

Next, φ_{F1}can be estimated by

$$\varphi_{F1} = \sum_{i=1}^{7} a_i \widetilde{\emptyset}_3(k+4)\,, \qquad k \geq \frac{N_1}{2} \tag{4.20}$$

where a_i is the coefficient. Assuming $f_{samp} = 1.44\ \mathrm{kHz/s}$, then using the least square fitting method to estimate the coefficient. We can obtain: $a_1 = -51.4286$, $a_2 = -34.2857$, $a_3 = -17.1429$, $a_4 = 0$, $a_5 = 17.1429$, $a_6 = 34.2857$, $a_7 = 51.4286$.

The final frequency can be calculated by substituting (4.20) in to (4.18).

4.3.3 Discussion of algorithm complexity

The number multiplications and additions within the proposed algorithm is used to assess its complexity. Assuming f_{samp}=1.44 kHz/s, $N_s = 31$, then number of multiplications and additions are shown in Table 4.3.

Table 4.3 Number of multiplications and additions within the proposed algorithm

Module	Number of multiplications	Number of additions
NRM	123	3690
PEM	2496	1222
EFFERM	180	165
OFFERM	14	14
PMERM	14	21
FEM	7	6
Total	2834	5118

Depending on the reporting rate F_r of phase angle and frequency measurements per second, the total number of multiplications and additions in one second is $2834 \times F_r$ and $5118 \times F_r$, respectively. Most digital signal processors (DSP) have a hardware multiplier, so they can execute multiplication and accumulation in a single cycle. For example, a Texas Instruments floating-point digital signal processor TMS320C6713 with 200 MHz clock rate has two multipliers (Floating and Fixed-Point) and a pipeline architecture. It can deliver up to 1200 million float-point operations per second (MFLOPS) meaning that the number of full word-size float point multiplication operations that can be performed per second is 1200 million. Assuming the phase angle and frequency reporting rate is 120 Hz/s, which is the highest rate in PMUs, then the number of multiplications and additions in one second is about 0.34 million and 0.61 million, respectively. Compared to the 1200 million MFLOPS of the DSP, the algorithm complexity of the proposed algorithm is very low. Figure 4.17 shows the distribution of multiplications and additions in different modules. We can see that NRM, EFFERM, OFFERM, PMERM, and FEM account for only about 12% percent of total multiplications. As for additions, since some ADC has oversampling function like AD7606 from Analog Devices, Inc, the number of additions can be greatly reduced by implementing NRM on ADC.

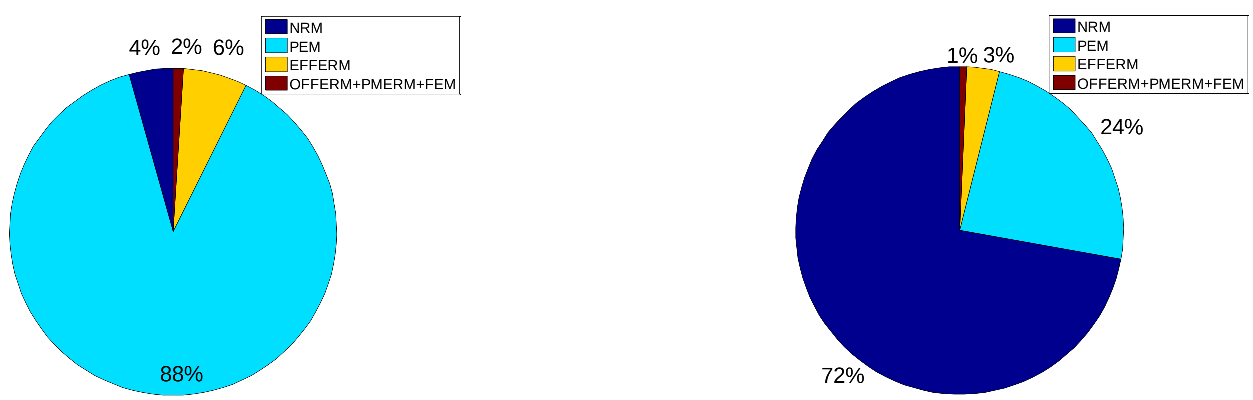

(a). Multiplications distribution (b). Additions distribution

Figure 4.17 Distribution of multiplications and additions in different modules

4.4 Angle and frequency measurement accuracy assessment

Results in this section refer to simulations performed in a MATLAB® environment. Software routines have been implemented to generate reference signals and to estimate angle and frequency using the Avg_Avg2Comp DFT algorithm and the Qps-DFT algorithm. To analyze the results in detail, every algorithm has been implemented in a "sliding window" approach (an overlapping computation window), continuously shifting the phasor and frequency estimation window by a single sample. The angle measurement errors are converted to total vector error (TVE) used in the PMU Standard. Because this paper does not introduce the magnitude estimation and phase angle error has a greater effect on TVE compared to magnitude error, thus the magnitude error is assumed to be zero for TVE calculation. As a result, the TVE calculated in the following tests is called "approximate TVE (aTVE)". Table 4.4 shows all the testing conditions and measurement errors of the two algorithms compared to the measurement accuracy requirement under 120Hz reporting rate in the PMU Standard. "NA" is used in the column "PMU Standard C37.118.1 (a)" if the corresponding test does not exist in the Standard.

4.4.1 Noise distortion test

According to the PSD analysis of the power grid signals at distribution level, the SNR is about 60 dB. Therefore, a 60 Hz signal distorted with 60dB noise is used as the reference signal to test the measurement accuracy of the two algorithms. As shown in Table 4.4, we can see that the angle accuracy of Avg_Avg2Comp DFT is better than the Qps-DFT algorithm. The frequency measurement errors of the two algorithms are close to each other. Since the PMU Standard has no TVE or frequency measurement accuracy requirement under noise condition. Using the 1% TVE and 5m Hz accuracy requirement under frequency range test as a reference, the estimation errors of the proposed algorithm are much less than the maximum errors allowed, particularly for angle measurement accuracy.

4.4.2 Harmonic distortion test

In PMUs and FDRs, a low-pass filter is used before the analog-to-digital (ADC) for anti-aliasing and harmonics reduction. The two algorithms adopts the same low-pass filter for a fair comparison. The filter is fourth-order Butterworth filter and the cutoff frequency is 300 Hz. Different from the harmonic test in the PMU Standard, where only $i \times f_0$ ($i \geq 2, f_0 = 60$) Hz harmonics is considered, the proposed algorithm is tested under different fundamental frequency conditions as shown in Table 4.4. 10% (20 dB), each harmonics up to 50^{th} is added to the fundamental frequency signal for the test. We can see that both algorithms have a very good measurement accuracy under 60 Hz condition. The advantage of the proposed algorithm can be seen under off-nominal frequency condition. For example, the testing results under 59.5Hz fundamental frequency condition are shown in Figure 4.18. We see that the proposed algorithm has better measurement accuracy under most harmonic conditions.

Table 4.4 Testing of the proposed algorithm compared to Qps-DFT algorithm

Test	Reference signal	Qps-DFT algorithm		Avg_Avg2Comp DFT algorithm		PMU Standard C37.118.1(a)	
		Angle error in degree/aTVE	Frequency error in mHz	Angle error in degree/aTVE	Frequency error in mHz	TVE	Frequency in mHz
Noise	$1\cos(2\pi f_0 t)$+ 60dB noise	0.033/0.06%	1.1	0.005/0.009%	1.3	NA	NA
Frequency range	$1\cos(2\pi f t)$ $55 \leq f \leq 65$	0.05/0.09%	1.8	0.04/0.07%	0.25	1%	5
Harmonics	$\cos(2\pi 59.5t) + 0.1\cos(2\pi i 59.5t)$ $2 \leq i \leq 50$	0.023/0.04%	0.528	0.004/0.007%	0.315	NA	NA
	$\cos(2\pi 60t) + 0.1\cos(2\pi i 60t)$ $2 \leq i \leq 50$	6.1×10^{-13}/0%	7.1×10^{-12}	0.003/0.005%	2.8×10^{-11}	1%	25
	$\cos(2\pi 60.5t) + 0.1\cos(2\pi i 60.5t)$ $2 \leq i \leq 50$	0.025/0.04%	0.485	0.003/0.005%	0.184	NA	NA
Frequency ramp	$1\cos(2\pi(55 + 0.5t)t)$ $0 \leq t \leq 10$	0.19/0.33%	7.4	0.022/0.04%	0.268	1%	10
Magnitude modulation	$(1 + 0.1\cos(2\pi f_m t)) * \cos(2\pi f_0 t)$ $f_m = 1,2,3,4,5$	0.026/0.05%	0.38	3.6×10^{-3}/0.006%	0.35	3%	300
Phase modulation	$1\cos(2\pi f_0 t + 0.1\cos(2\pi f_a t - \pi))$ $f_a = 1,2,3,4,5$	1.58/2.76%	116	2×10^{-3}/0.004%	1.5	3%	300
Artificial signal	$1\cos(2\pi 59.95t)$+$\sum_{i=2}^{50} v_h \cos(2\pi \times i \times 59.95t + \theta(i))$+60dB noise	0.04	1.27	0.005	1.49	NA	NA

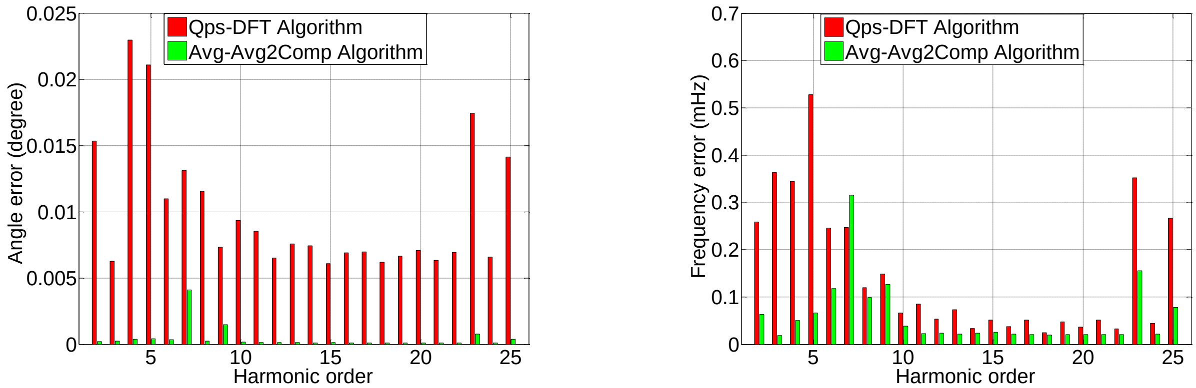

(a). Angle error (b). Frequency error

Figure 4.18 Harmonic distortion test under 59.5 Hz

4.4.3 Frequency ramp test

Under the frequency ramp test, we see that the angle and frequency measurement errors of the new algorithm are much less than the Qps-DFT algorithm. The frequency measurement error of Qps-DFT algorithm is close to accuracy requirement limit. In contrast, the maximum frequency measurement error of the proposed algorithm is only 0.268 mHz, which is much less than the 10 mHz requirement.

4.4.4 Magnitude modulation test

Compared to Qps-DFT algorithm, the proposed algorithm also has better measurement accuracy, particularly for angle measurement. Note that the aTVE of the new algorithm is 0.006% and frequency measurement error is about 0.35 mHz, which far exceeds the PMU Standard.

4.4.5 Phase modulation test

The angle and frequency errors of Qps-DFT are very large and cannot comply with the PMU Standard. In contrast, thanks to PMERM, both the angle and frequency measurement accuracy are greatly improved. A 0.004% aTVE, 1.5 mHz frequency measurement error far exceeds the PMU Standard, which is 3% TVE and 300 mHz.

4.4.6 Artificial signal test

In this test, an artificial signal is generated as follows:

$$1\cos(2\pi 59.95t)+\sum_{i=2}^{50} v_i \cos(2\pi \times i \times 59.95t + \theta(i))+60\text{dB noise}$$

where the fundamental frequency is 59.95 Hz; v_i is the magnitude of i-th order harmonics; $\theta(i)$ is angle of i-th order harmonics. v_i is obtained from the PSD analysis of power grid signal at distribution level as shown in Figure 4.2. 60dB noise is added to the artificial signal. As shown in Table 4.4, the proposed algorithm has much higher angle measurement accuracy. As for the frequency measurement errors, we see that both of the algorithms have high measurement accuracy, even though the proposed algorithm is a little worse than the Qps-DFT algorithm. Note that since the artificial signal emulates the noise and harmonics in a real power grid environment, this test can verify that effectiveness of the tested algorithms in a real power grid environment.

4.5 Conclusion

In this chapter, the power grid signals at the distribution level were collected. By analyzing the data using modified periodogram method, we can conclude that the power grid signals at the distribution level are mainly distorted by noise and harmonics. The phasor model in the PMU Standard was used to evaluate the effect of noise and harmonics on the phasor measurement accuracy. As a result, we can find both the noise and harmonics can cause large phasor measurement errors. To improve the phasor measurement algorithm under those conditions, a new DFT based phasor estimation algorithm suitable for distribution level measurement was proposed in this chapter. The algorithm consists of six modules: NRM; PEM; EFFERM; OFFERM; PMERM; and FEM. NRM can filter the noise and improve the measurement accuracy under noise distortion condition. EFFERM and OFFERM can reduce the measurement errors when the power grid signal contains harmonics and deviates from nominal frequency. PMERM can greatly improve the measurement accuracy under phase modulation condition. The proposed algorithm has been tested under noise conditions, harmonic conditions, and different steady-state and dynamic conditions required in the PMU Standard. The testing results demonstrated that the proposed algorithm has high measurement accuracy and far exceeds the PMU Standard. Beyond the PMU Standard, the parameters of the new algorithm are optimized using the power grid signal sampled at the distribution level to achieve high measurement accuracy in a real power grid environment. The algorithm complexity is also discussed. Since the coefficient of all the filters is constant and can be calculated offline, the algorithm complexity is low and can be implemented on a modern digital signal processor.

Chapter 5 Dynamic Phasor Model for Synchrophasor Measurement

5.1 Introduction

Both the FDR algorithm and Avg_Avg2Comp DFT algorithm are based on DFT. With a better understanding of power grid waveforms, another synchrophasor measurement method that are gaining more attention is the signal model based phasor measurement method. In this chapter, a signal model based synchrophasor measurement method is presented, and the performance of this method will be tested under different conditions and compared to FDR algorithm.

Aside from DFT-based methods, some dynamic signal models have been proposed to improve the accuracy under dynamic conditions [45]-[47]. A dynamic phasor model is proposed in [45], the dynamic phasor can be estimated by least squares Taylor expansion Fourier (LS-TF) method or weighted least squares Taylor expansion Fourier (WLS-TF) method [47]. However, because these methods assume the input signal is a band-pass signal, the methods under harmonics condition are not accurate, and cannot comply with the PMU Standard under harmonic conditions. In this chapter, based on the WLS-TF method in [47], the dynamic model is extended to include harmonics. The extended dynamic model will improve phasor estimation accuracy. The improved method will be compared with the FDR algorithm under different scenarios according but not limited to PMU Standard.

5.2 Extended dynamic phasor model

A narrowband band-pass signal model is assumed in the WLS-TF method [47], which is

$$s(t) = a(t)\,cos(2\pi f_0 t + \varphi(t)) \tag{5.1}$$

As for the angle estimation, the accuracy is high when the input signal can be represented by the signal model. However, the waveforms of power system are distorted by harmonics, which will cause estimation error. This error is particularly produced by 2^{nd} order harmonic due to its minimal spectral distance from the fundamental frequency component. In order to improve the estimation accuracy under harmonic condition, harmonic signal model can be added to the signal model. The effect of harmonics distortion on angle estimation will be assessed first to determine the highest order of harmonic component that needs to be added to the fundamental frequency signal model.

The reference signals for this test is

$$s(t) = 1\,cos(2\pi f_0 t) + 0.1\,cos(2\pi M f_0 t) \tag{5.2}$$

where f_0 is the fundamental frequency, and M is the order of harmonic. 10% harmonics is added to the fundamental frequency signal.

Table 5.1 shows the angle errors in degree regard to different harmonic orders under different fundamental frequency conditions.

Table 5.1 Angle errors under different order of harmonics

M	Angle error (degree)	
	$\boldsymbol{f_0 = 60}$	$\boldsymbol{f_0 = 59.5}$
2	6.99×10^{-2}	7.19×10^{-2}
3	1.20×10^{-3}	9.67×10^{-4}
4	1.66×10^{-4}	1.22×10^{-4}
5	3.79×10^{-5}	3.23×10^{-5}
6	1.49×10^{-5}	1.19×10^{-5}
7	5.82×10^{-6}	5.04×10^{-6}
8	2.52×10^{-6}	2.80×10^{-6}
9	9.08×10^{-7}	1.66×10^{-6}
10	3.85×10^{-7}	1.01×10^{-6}

According to Table 5.1, the effect of harmonics on angle estimation decreases as the order of harmonics increase. First, we can see that the angle errors under 59.5 Hz and 60 Hz fundamental frequency condition are close to each other. This feature is favorable compared to DFT based method, in which the angle error is close to zero but increase dramatically when the frequency deviates from 60Hz. More importantly, the effect of harmonics on angle estimation accuracy is negligible when the order is greater than 3. As a result, the dynamic phasor is extended to include 2^{nd} and 3^{rd} order harmonics to improve the estimation accuracy under harmonics condition, and the new signal model including 2^{nd} and 3^{rd} order harmonic can be represented as

$$s(t) = A_0(t)\,cos(2\pi f_0 t + \varphi_0(t)) + \sum_{i=2}^{3} A_i(t)\,cos(2\pi i f_0 t + \varphi_i(t)) \tag{5.3}$$

It can be rewritten in terms of complex exponential function as

$$s(t) = \frac{1}{2}\left(P(t)e^{j2\pi f_0 t} + \bar{P}(t)e^{-j2\pi f_0 t}\right)$$
$$+ \sum_{\mathrm{i}=2}^{3} \frac{1}{2}\left(Q_i(t)e^{j2\pi i f_0 t} + \bar{Q}_i(t)e^{-j2\pi i f_0 t}\right) \tag{5.4}$$

where $P(t) = A_0(t)e^{j\varphi_0(t)}$, $Q_i(t) = A_i(t)e^{j\varphi_i(t)}$; f_0 is the nominal frequency; $\overline{\mathrm{P}}(\mathrm{t})$ and $\bar{Q}_i$ are complex conjugates of P(t) and Q_i(t), respectively.

Using quadratic polynomial to approximate$P(t)$, and linear polynomial to approximate Q_i(t)

$$\begin{cases} P(t) \approx p_0 + p_1 t + p_2 t^2 \\ Q_i(t) \approx q_{i0} + q_{i1} t \end{cases} \tag{5.5}$$

The quadratic polynomial can improve the accuracy of the model under off-nominal frequency condition and dynamic condition, especially for phase modulation condition. The linear polynomial can improve the model accuracy under harmonic condition when the power grid frequency deviates from nominal frequency.

5.3 Angle and frequency estimator

5.3.1 Angle estimation

The angle of the input signal is $\varphi_0(t)$ which is included in $P(t)$, and if the purpose is to estimate the angle at $t = 0$, then we can obtain the angle by

$$\varphi_0(t)|_{t=0} = \angle p_0 \tag{5.6}$$

So the angle can be estimated through p_0.

In order to estimate p_0, WLS fitting method is used. Assuming $(2N_h + 1)$ samples are used for angle estimation, and these samples are fitted to the signal model, then we have

$$\mathbf{S} = \mathbf{BM} \tag{5.7}$$

where

$$\mathbf{S} = [s(-N_h), \dots, s(0), \dots, s(N_h)]'$$

s(j) ($\mathrm{j} = -N_h, \dots, N_h$) is the value of jth sample.

$$\boldsymbol{M} = [\overline{p_2},\ \overline{p_1},\ \overline{p_0}, \overline{q_{21}},\ \overline{q_{20}},\ \overline{q_{31}},\ \overline{q_{30}}, q_{30}, q_{31},\ q_{20}, q_{21}, p_0, p_1, p_2\ \ ]'$$

M is a matrix constructed with the coefficients of the quadratic polynomial and linear polynomial

B corresponds to the relationship between $\boldsymbol{S}$ and $\boldsymbol{M}$.

$$\boldsymbol{M} = (\boldsymbol{M_1}, \boldsymbol{M_2}, \boldsymbol{M_3}, \boldsymbol{M_4}, \boldsymbol{M_5}, \boldsymbol{M_6})$$

$$\boldsymbol{M_1} = \begin{pmatrix} (-N_h)^2 e^{jN_h\omega_1} & (-N_h)^1 e^{jN_h\omega_1} & (-N_h)^0 e^{jN_h\omega_1} \\ \dots & \dots & \dots \\ (-n)^2 e^{jn\omega_1} & (-n)^1 e^{jn\omega_1} & (-n)^0 e^{jn\omega_1} \\ \dots & \dots & \dots \\ 0 & 0 & 1 \\ \dots & \dots & \dots \\ (n)^2 e^{-jn\omega_1} & (n)^1 e^{-jn\omega_1} & (n)^0 e^{-jn\omega_1} \\ \dots & \dots & \dots \\ (N_h)^2 e^{-jN_h\omega_1} & (N_h)^1 e^{-jN_h\omega_1} & (N_h)^0 e^{-jN_h\omega_1} \end{pmatrix} \quad \boldsymbol{M_6} = \begin{pmatrix} (-N_h)^0 e^{-jN_h\omega_1} & (-N_h)^1 e^{-jN_h\omega_1} & (-N_h)^2 e^{-jN_h\omega_1} \\ \dots & \dots & \dots \\ (-n)^0 e^{-jn\omega_1} & (-n)^1 e^{-jn\omega_1} & (-n)^2 e^{-jn\omega_1} \\ \dots & \dots & \dots \\ 1 & 0 & 0 \\ \dots & \dots & \dots \\ (n)^0 e^{jn\omega_1} & (n)^1 e^{jn\omega_1} & (n)^2 e^{jn\omega_1} \\ \dots & \dots & \dots \\ (N_h)^0 e^{jN_h\omega_1} & (N_h)^1 e^{jN_h\omega_1} & (N_h)^2 e^{jN_h\omega_1} \end{pmatrix}$$

$$\boldsymbol{M_2} = \begin{pmatrix} (-N_h)^1 e^{jN_h 2\omega_1} & (-N_h)^0 e^{jN_h 2\omega_1} \\ \dots & \dots \\ (-n)^1 e^{jn2\omega_1} & (-n)^0 e^{jn2\omega_1} \\ \dots & \dots \\ 0 & 1 \\ \dots & \dots \\ (n)^1 e^{-jn2\omega_1} & (n)^0 e^{-jn2\omega_1} \\ \dots & \dots \\ (N_h)^1 e^{-jN_h 2\omega_1} & (N_h)^0 e^{-jN_h 2\omega_1} \end{pmatrix} \quad \boldsymbol{M_5} = \begin{pmatrix} (-N_h)^0 e^{-jN_h 2\omega_1} & (-N_h)^1 e^{-jN_h 2\omega_1} \\ \dots & \dots \\ (-n)^0 e^{-jn2\omega_1} & (-n)^1 e^{-jn2\omega_1} \\ \dots & \dots \\ 1 & 0 \\ \dots & \dots \\ (n)^0 e^{jn2\omega_1} & (n)^1 e^{jn2\omega_1} \\ \dots & \dots \\ (N_h)^0 e^{jN_{h2}\omega_1} & (N_h)^1 e^{jN_h 3\omega_1} \end{pmatrix}$$

$$\boldsymbol{M_2} = \begin{pmatrix} (-N_h)^1 e^{jN_h 3\omega_1} & (-N_h)^0 e^{jN_h 3\omega_1} \\ \dots & \dots \\ (-n)^1 e^{jn3\omega_1} & (-n)^0 e^{jn3\omega_1} \\ \dots & \dots \\ 0 & 1 \\ \dots & \dots \\ (n)^1 e^{-jn3\omega_1} & (n)^0 e^{-jn3\omega_1} \\ \dots & \dots \\ (N_h)^1 e^{-jN_h 3\omega_1} & (N_h)^0 e^{-jN_h 3\omega_1} \end{pmatrix} \quad \boldsymbol{M_5} = \begin{pmatrix} (-N_h)^0 e^{-jN_h 3\omega_1} & (-N_h)^1 e^{-jN_h 3\omega_1} \\ \dots & \dots \\ (-n)^0 e^{-jn3\omega_1} & (-n)^1 e^{-jn3\omega_1} \\ \dots & \dots \\ 1 & 0 \\ \dots & \dots \\ (n)^0 e^{jn3\omega_1} & (n)^1 e^{jn3\omega_1} \\ \dots & \dots \\ (N_h)^0 e^{jN_{h2} 3\omega_1} & (N_h)^1 e^{jN_{h2} 3\omega_1} \end{pmatrix}$$

where $\omega_1 = 2\pi f_0$.

The best estimate of **M** in WLS sense is given by

$$\widehat{\boldsymbol{M}}_{WLS} = (\mathbf{B}'\boldsymbol{W}'\boldsymbol{W}\mathbf{B})^{-1}\mathbf{B}'\mathbf{W}'\boldsymbol{W}\boldsymbol{S} \tag{5.8}$$

where $\boldsymbol{W}$ is weights of the window, and hanning widow is used in this method.

Once $\widehat{\boldsymbol{M}}_{WLS}$ is estimated in WLS sense, angle can be computed through p_0.

5.3.2 Frequency estimation

Since the frequency is the derivative of angle, a sequence of angles are used to estimate the frequency. The angles can be represented by a quadratic polynomial

$$\varphi(i) = \varphi_{F0} + \varphi_{F1}\left(i - \frac{(N+1)}{2}\right) + \varphi_{F2}\left(i - \frac{(N+1)}{2}\right)^2 \tag{5.9}$$

where N is the number of angles used to estimate frequency, 9 angles are in this method.

Least squares fitting method is used to estimate the coefficients of the quadratic polynomial, and we can obtain

$$\boldsymbol{\varphi_{coef}} = \left(\boldsymbol{M_f}'\boldsymbol{M_f}\right)^{-1}\boldsymbol{M_f}'\boldsymbol{\varphi} \tag{5.10}$$

where $\varphi_{coef} = [\varphi_{F0}, \varphi_{F1}, \varphi_{F2}]'$.

M_f is a 9×3 matrix, and

$$M_f(i,j) = (i - \tfrac{(N+1)}{2})^{(j-1)} \; (i = 1, \dots, N, j = 1, 2, 3)$$
$$\varphi = [\varphi(1), \dots, \varphi(N)]'$$

The frequency at $\mathrm{t} = 0$ can be computed by

$$f_F(i)|_{i=0} = \frac{f_0 N_s}{2\pi M_{samp}} \varphi(i)'|_{i=0} = \frac{f_0 N_s}{2\pi M_{samp}} \varphi_{F1} \tag{5.11}$$

N_s is the number of samples per fundamental cycle, and N_s is equal to 24 in this method. M_{samp} is the number of samples slid by angle estimation window. In order to eliminate the effect of odd order harmonics on frequency estimation, a 1/2 fundamental cycle shift is used in the method, so M_{samp} is equal to 12. Note that the number of samples slid between windows is very important for frequency estimation under harmonics condition. A 1/2 fundamental cycle shift will not cause frequency estimation error under odd order harmonics condition since the frequency of the angle error caused by kth odd order harmonic satisfies

$$f_{oh} = (k-1)f_0 \;\; (k = 3, 5, \dots) \tag{5.12}$$

where f_{oh} is the frequency of the angle error.

A 1/2 fundamental cycle window shift can assure

$$\delta(1) = \delta(2) = \cdots = \delta(M) \tag{5.13}$$

where $\delta(i)$ is the estimation error of $\varphi(i)$.

It is worth noticing that the equivalent errors will not incur frequency estimation error using a quadratic polynomial since frequency is the derivative of angle.

5.4 Angle and frequency performance assessment

In order to improve the noise rejection performance of the new algorithm, the digital averaging filter is used for the new algorithm. The testing conditions for the algorithm assessment are similar as 4.4, and FDR algorithm is used for comparison.

5.4.1 Noise distortion test

50 dB noisy signal is generated under different fundamental frequency conditions, and the angle and frequency errors are shown in Figure 5.1 and Figure 5.2. We can see both the angle and frequency estimation accuracy are improved by the new algorithm.

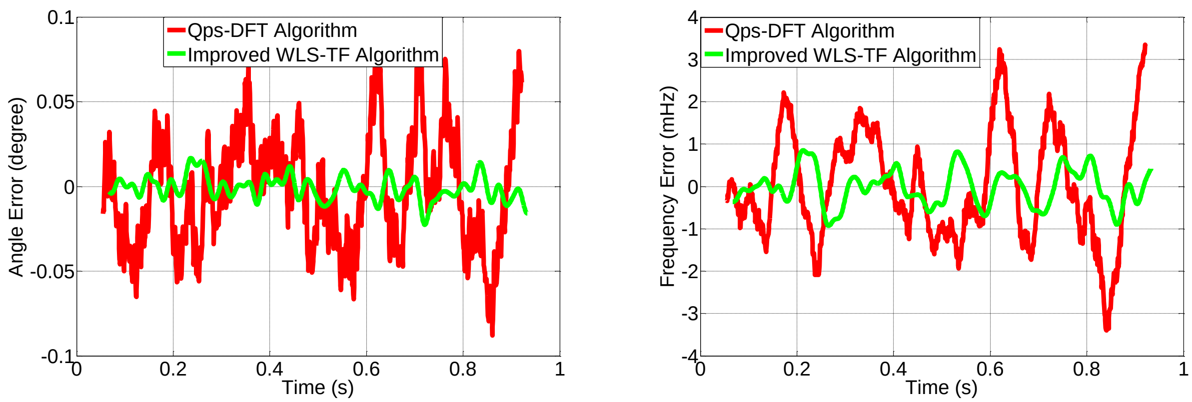

(a). Angle error (b). Frequency error

Figure 5.1 Noise test under 59 Hz condition

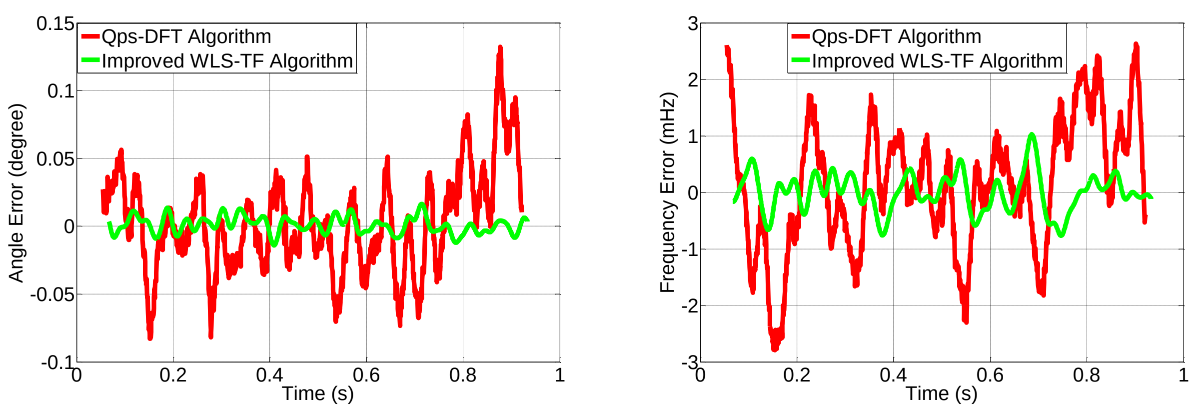

(a). Angle error (b). Frequency error

Figure 5.2 Noise test under 60 Hz condition

5.4.2 Frequency range test

As shown the testing results in Figure 5.3, the new algorithm has very good performance under a wide frequency range.

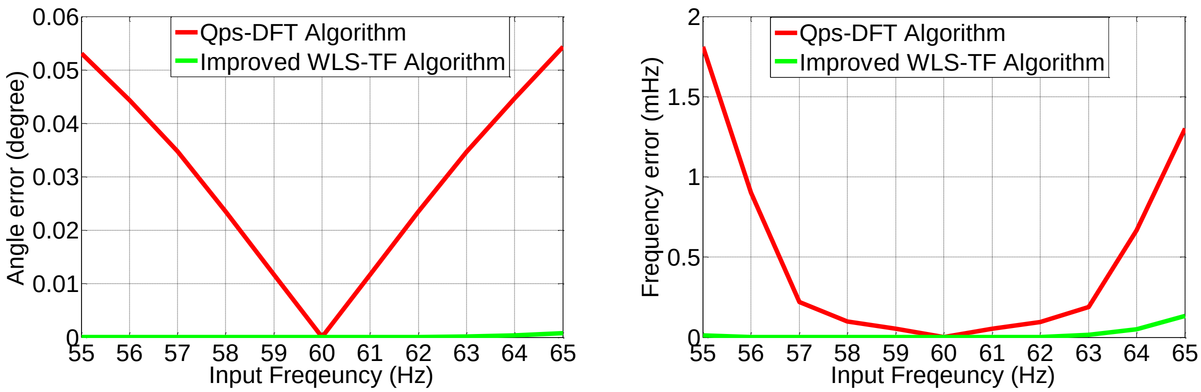

(a). Angle error (b). Frequency error

Figure 5.3 Frequency range test

5.4.3 Harmonic distortion test

As shown in Figure 5.4, the angle measurement of the new algorithm is not immune to harmonics, however the angle errors are very small which are less than 0.005 degree.

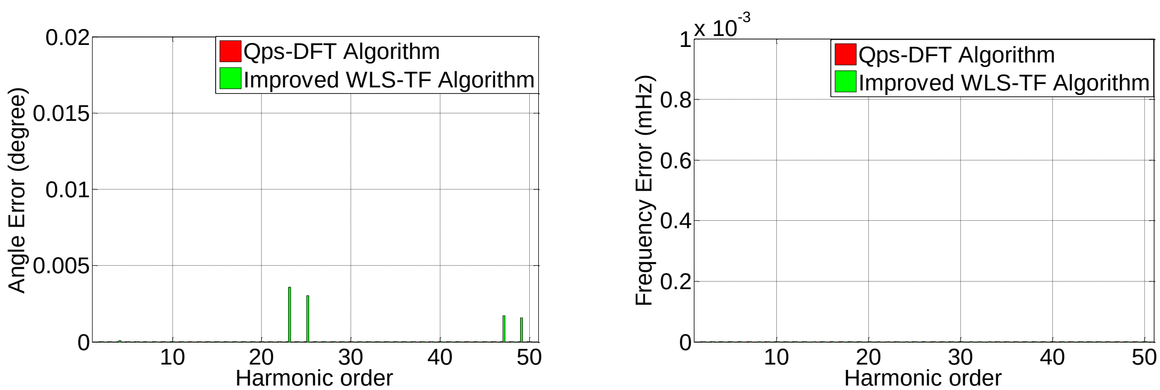

(a). Angle error (b). Frequency error

Figure 5.4 Harmonics test under 60 Hz fundamental frequency condition

5.4.4 Harmonic distortion test under off-nominal frequency condition

The testing results of FDR algorithm and new algorithm are shown from Figure 5.5 to Figure 5.10. We can see that the new algorithm has good angle and frequency estimation accuracy under different fundamental frequency conditions. In brief, the angle error of the new algorithm is less than 0.1 degree and frequency error is less than 5 mHz. Note that the real power grid signals do not have so much harmonic in the simulation, the angle and frequency errors under field condition are less than this number.

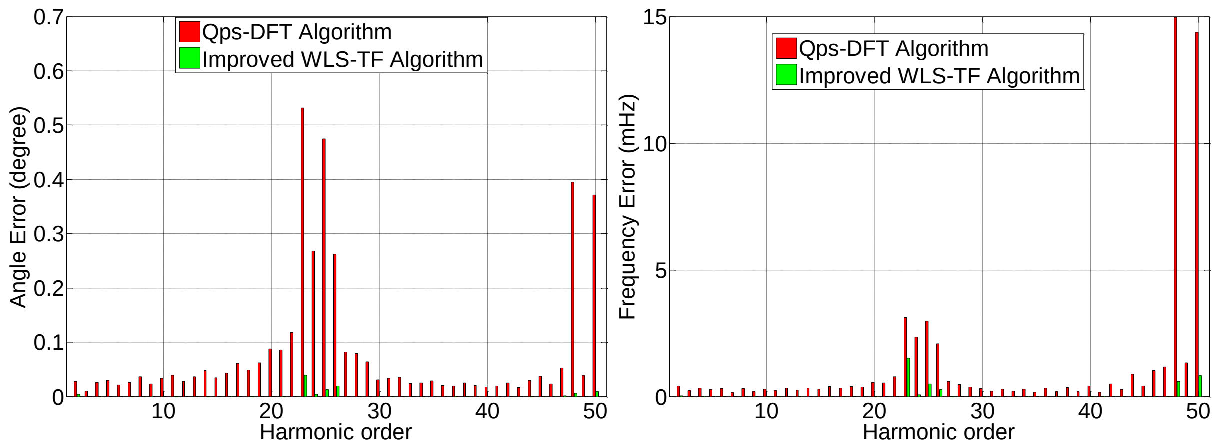

(a). Angle error (b). Frequency error

Figure 5.5 Harmonics test under 59 Hz fundamental frequency condition

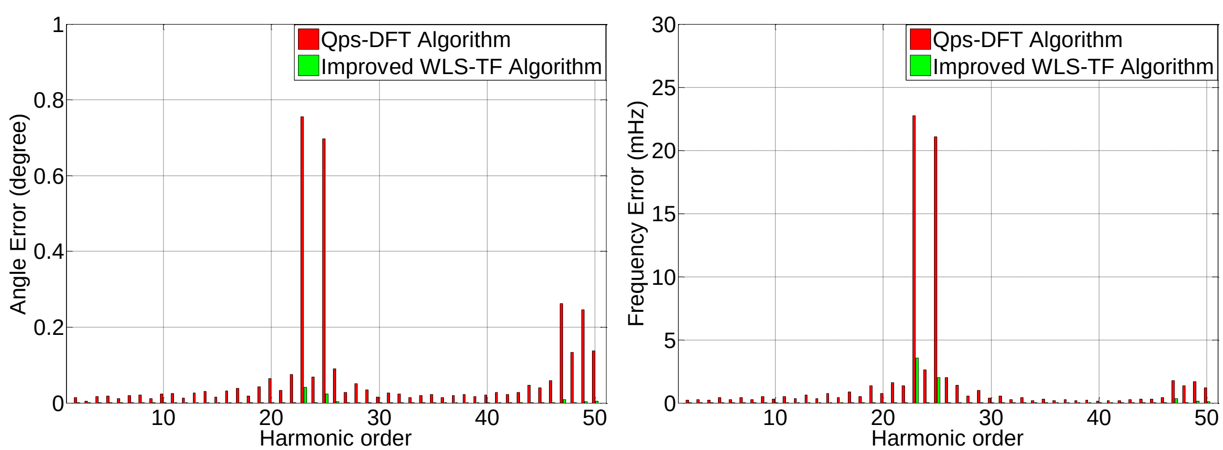

(a). Angle error (b). Frequency error

Figure 5.6 Harmonics test under 59.5Hz fundamental frequency condition

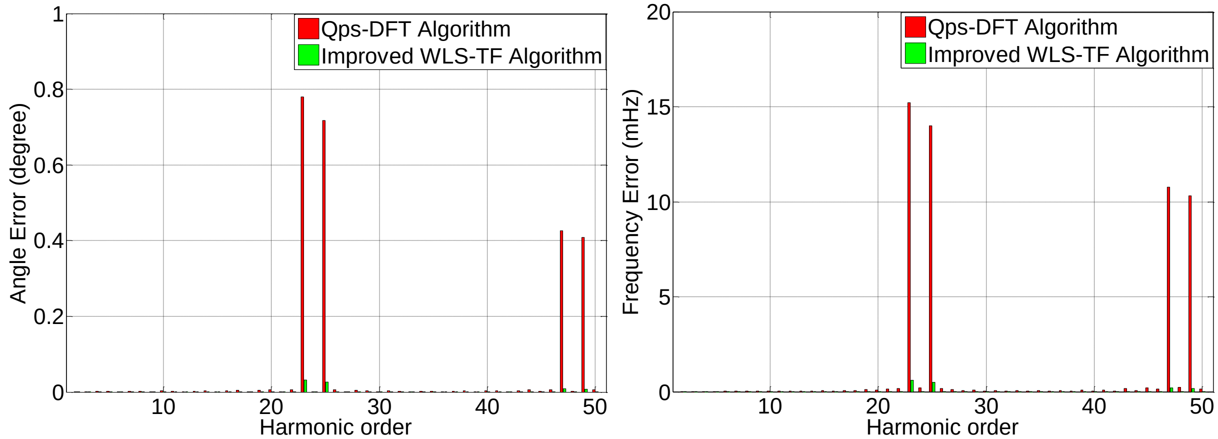

(a). Angle error (b). Frequency error

Figure 5.7 Harmonics test under 59.95Hz fundamental frequency condition

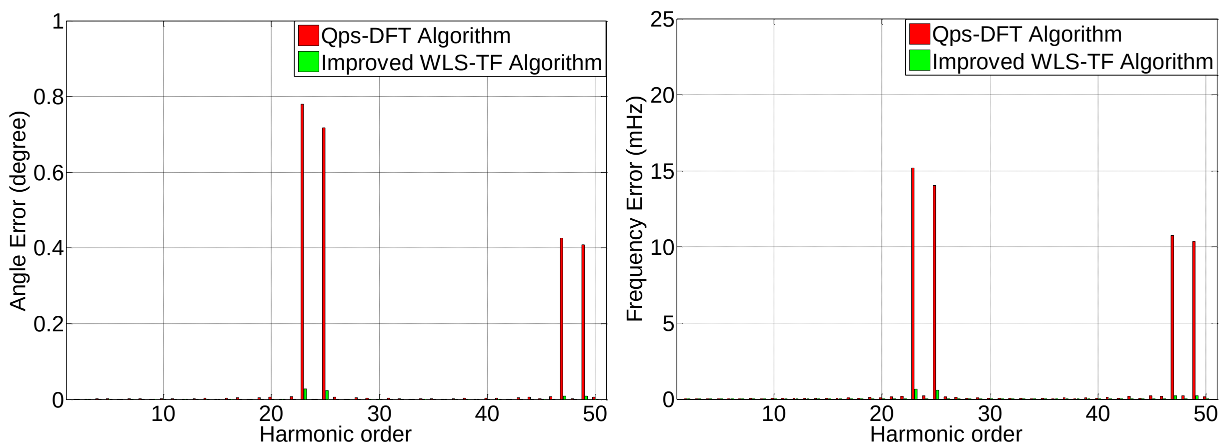

(a). Angle error (b). Frequency error

Figure 5.8 Harmonics test under 60.05Hz fundamental frequency condition

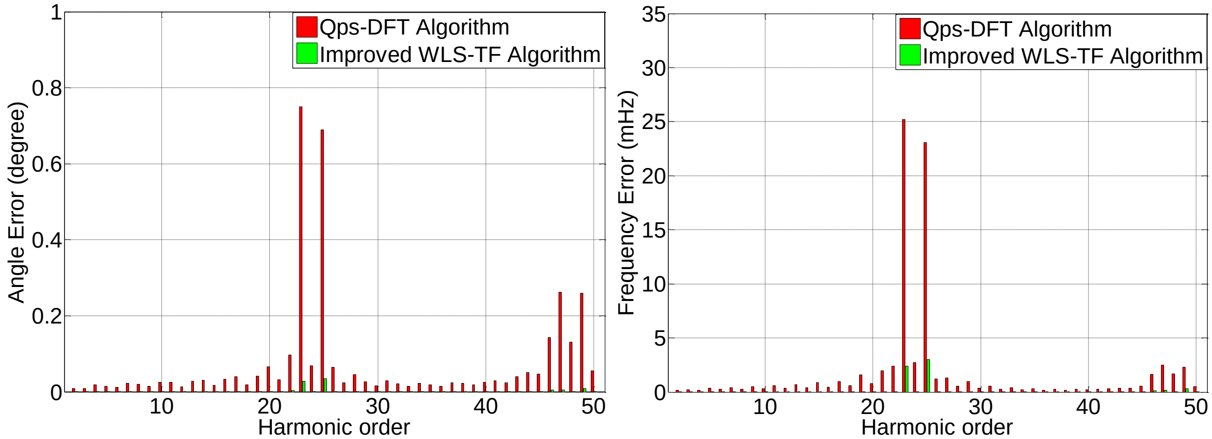

(a). Angle error (b). Frequency error

Figure 5.9 Harmonics test under 60.5Hz fundamental frequency condition

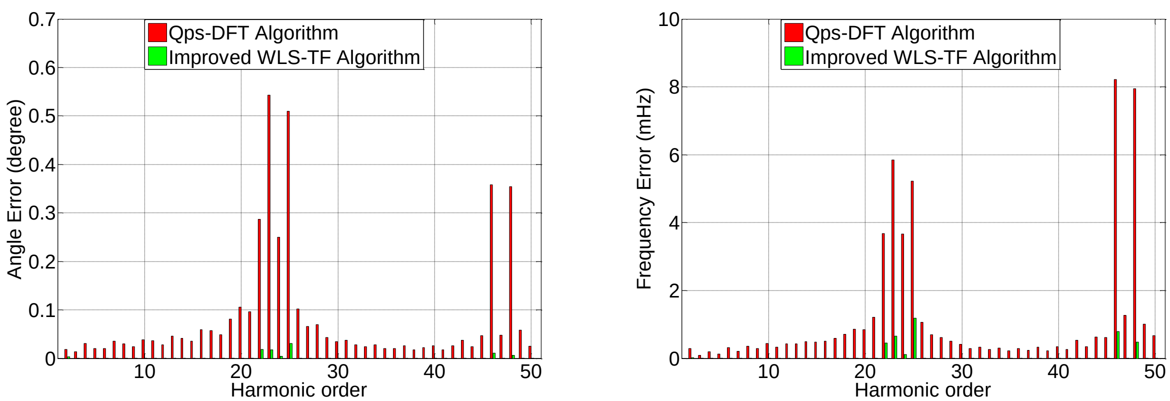

(a). Angle error (b). Frequency error

Figure 5.10 Harmonics test under 61 Hz fundamental frequency condition

5.4.5 Frequency ramp test

Thanks to the dynamic model, the new algorithm has very good accuracy under frequency ramp condition as shown in Figure 5.11 and Figure 5.12. The test signal is $\mathrm{s(t)} = 1\cos(2\pi(59.5 + 0.5t)t)$ and $\mathrm{s(t)} = 1\cos(2\pi(60.5 - 0.5t)t)$, $0 \leq t \leq 1$, respectively.

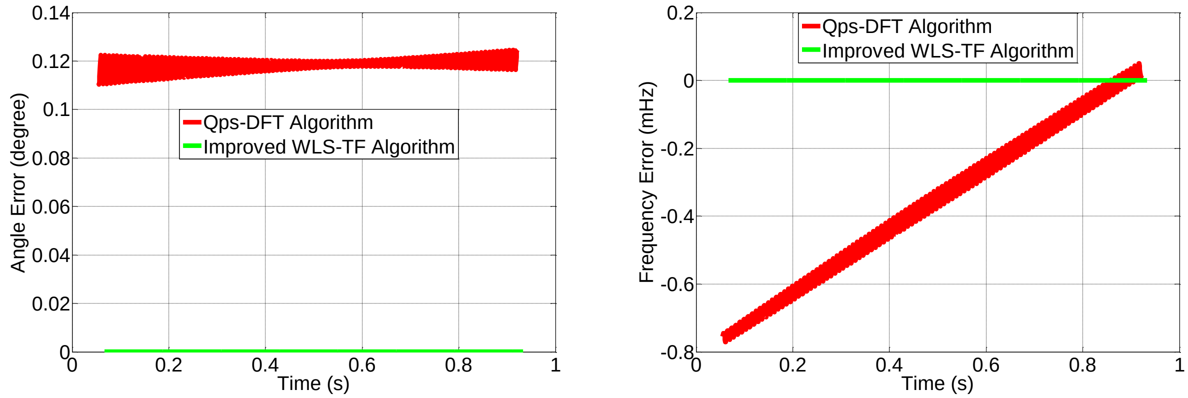

(a). Angle error (b). Frequency error

Figure 5.11 Frequency ramp test

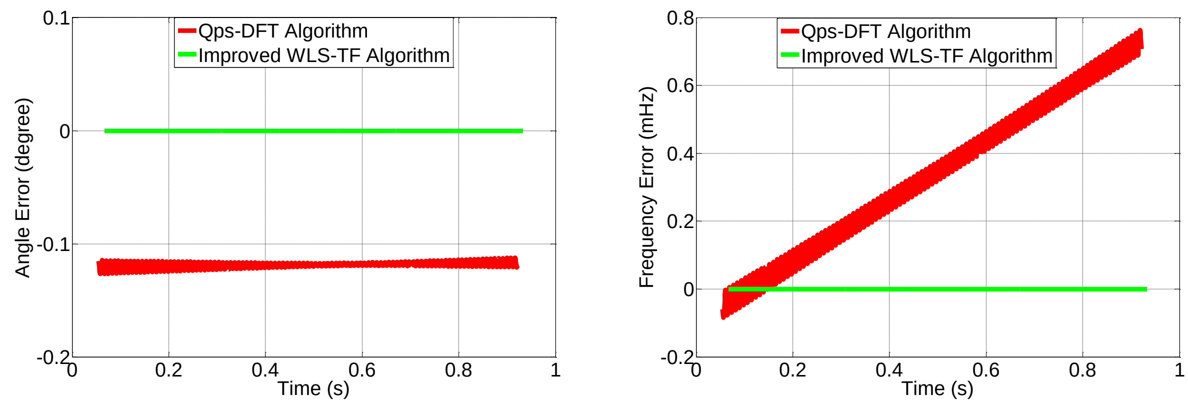

(a). Angle error (b). Frequency error

Figure 5.12 Frequency ramp test

5.4.6 Magnitude modulation test

As for magnitude modulation test, both the FDR algorithm and new algorithm perform well under this condition, and the new algorithm shows better accuracy under this condition.

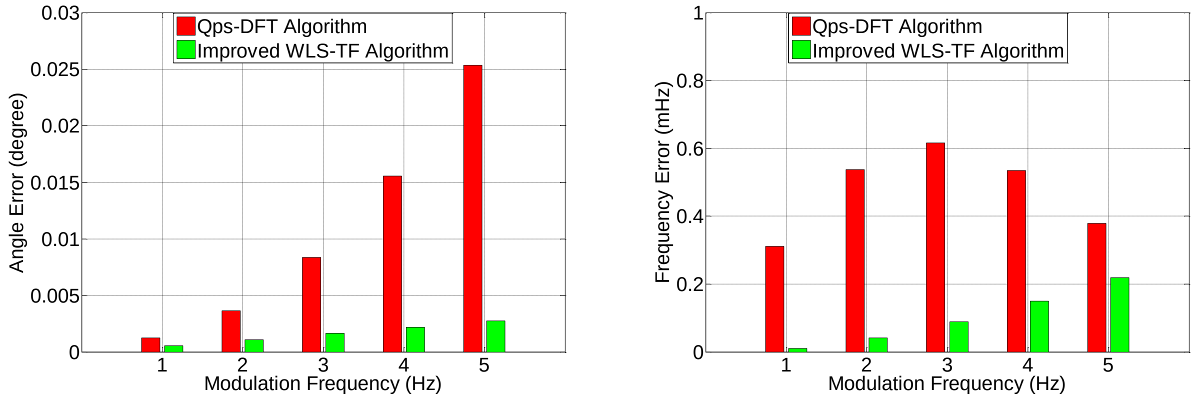

(a). Angle error (b). Frequency error

Figure 5.13 Magnitude modulation test

5.4.7 Phase modulation test

As for phase modulation test, the angle measurement of the new algorithm is rather accurate compared to FDR algorithm. The frequency accuracy of the new algorithm is about one order of magnitude better than FDR algorithm. Note that the frequency accuracy can be improved further by reducing the number of angles for frequency estimation or increasing the order of the polynomial in (5.9) . However, the frequency accuracy improvement under phase modulation condition is at the expense of worse noise rejection performance, so there is a tradeoff for frequency accuracy between noise condition and phase modulation condition.

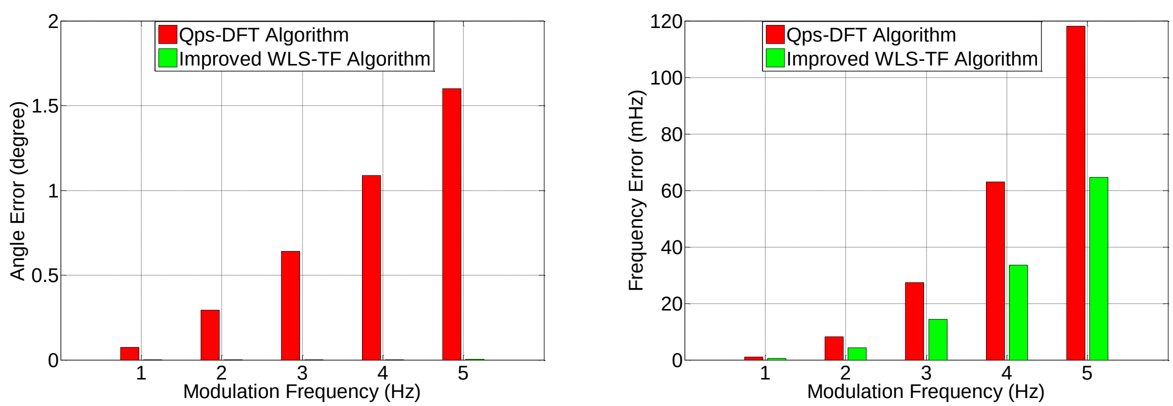

(a). Angle error (b). Frequency error

Figure 5.14 Phase modulation test

5.4.8 Composite signal test

The reference test signal is:

$s(t) = (1 + 0.1\cos(2\pi 2t)) * \cos(2\pi 59.5t + 0.1\cos(2\pi 2t - \pi))$+0.1cos$(2\pi * 2 * 59.5t)$+ 0.1cos$(2\pi * 3 * 59.5ft)$+50 dB noise

We can see the new algorithm also has good performance under this condition, especially for angle accuracy.

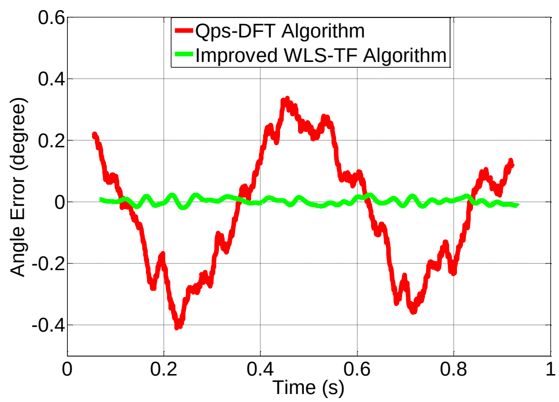

(a). Angle error

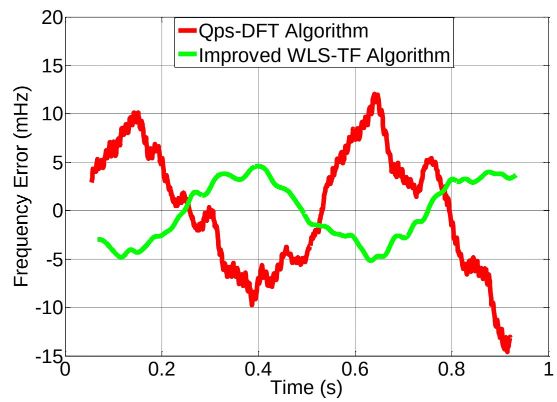

(b). Frequency error

Figure 5.15 Composite signal test

5.4.9 Real data test

In this test, the real data sampled from 120 V distribution level is used for algorithm testing. Since there is no true reference for error analysis, the angle difference between the algorithms is plotted in Figure 5.16 (a), and the frequency of the two algorithms are plotted in Figure 5.16 (b). We can see the maximum angle difference is about 0.3 degree. As for frequency comparison, since the signal frequency is close to 60 Hz, both the algorithms have high accuracy and the results of the two algorithms almost match each other.

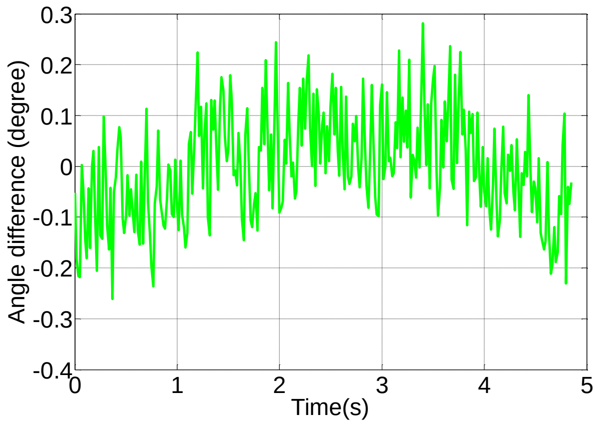

(a). Angle difference

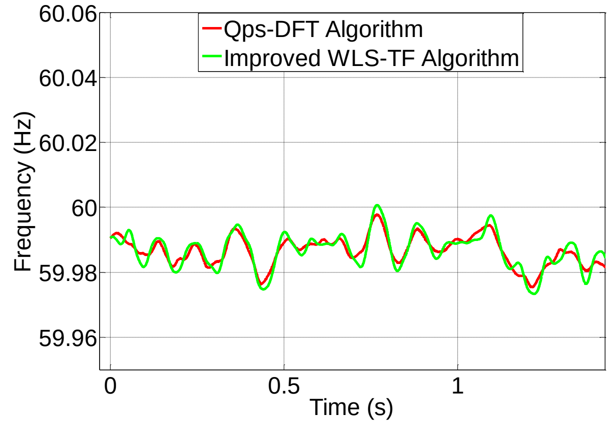

(b). Frequency

Figure 5.16 Real data test

5.5 Conclusion

In this chapter, based on the WLS-TF method, an extended phasor model suitable for power grid synchrophasor measurement is proposed. The new algorithm has high angle estimation accuracy under all testing conditions and improved frequency estimation accuracy compared to FDR algorithm. Different testing conditions following the PMU Standard, harmonic test under off-nominal frequency condition, and real data test demonstrated that the new algorithm is a promising method for angle and frequency estimation at distribution level.

Chapter 6 PMU Testing and Calibration of PMU/FDR Testing System

6.1 Introduction of PMU testing system

As a part of synchrophasor measurement improvement, it is important to build an accurate PMU/FDR testing system. UTK and ORNL, as a participating laboratory of PMU metrological interlaboratory comparison (PMU ILC) initiated by National Institution of Standard and Technology (NIST), built a PMU testing system. The testing system consists of a computer, Power System Simulator (PSS), GPS antenna, and PMU under test. The overall structure of the testing system is shown in Figure 6.1.

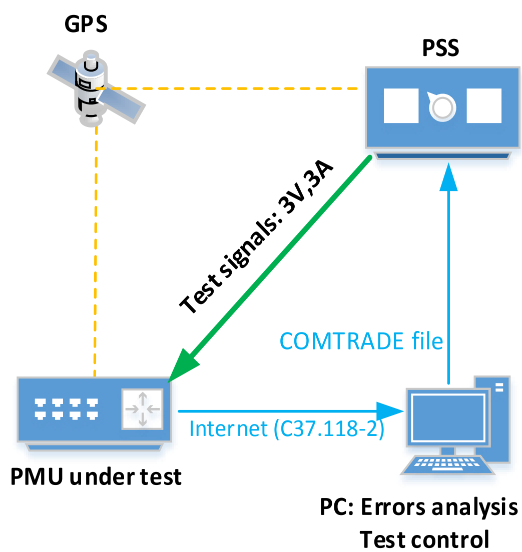

Figure 6.1 Overall structure of PMU testing system

Doble F6150 is used as the PSS. Doble is synchronized to GPS and controlled by software Transwin to generate accurate three-phase voltage and three phase current signals for PMU under test.

On the computer, there are four software:

1) Matlab: Generate reference testing signal for PMU in COMTRADE file format.
2) Transwin: Import COMTRADE file and generate reference signals for PMU under test.

3) Open PDC: Receive PMU measurement data in C37.118.2-2011 data format.
4) Error analysis software: calculate the errors of the PMU measurement data.

More than 600 tests have been tested on a commercial PMU at the UTK/ORNL:

1) Preliminary test including different nominal frequency (50Hz/60Hz), and different reporting rate.
2) Steady-state compliance test including signal frequency range, signal magnitude (voltage/current), harmonic distortion, and out-of-band interference.
3) Dynamic compliance test including amplitude modulation, phase modulation, frequency ramp, and step change in phase/magnitude.

6.2 Calibration of PMU testing system

The PMU testing results at UTK/ORNL are compared to the testing results at NIST. Figure 6.2 shows the total vector error (TVE), phase angle error, and frequency error of the PMU under frequency range test. The green curves represents the testing result at UTK/ORNL, and the blue curves represents the testing results at NIST. We can see that the testing results at UTK/ORNL are not consistent with the testing results at NIST for both TVE and phase angle.

The testing results under frequency ramp test are summarized in Table 6.1. It can also be seen that the testing results at UTK/ORNL are inconsistent with those at NIST including TVE, phase angle error, and frequency error. **It should be noted that the PMU under test in this Chapter is not traceably calibrated and all the data from NIST is unofficial, and the data is only for research purpose.**

Table 6.1 PMU error under frequency ramp test

	TVE (%)	Maximum angle error (degree)	Maximum frequency error (Hz)
UTK/ORNL	0.3275	0.4906	0.0513
NIST	0.2462	0.2487	0.0456

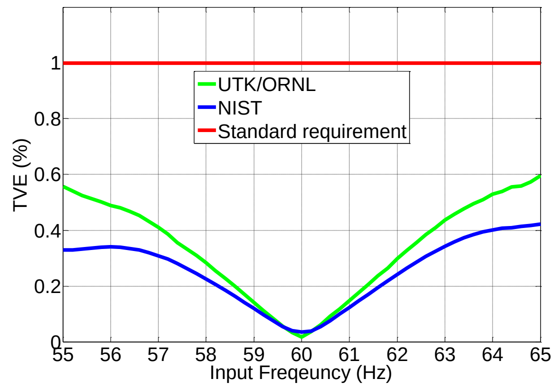

(a). TVE

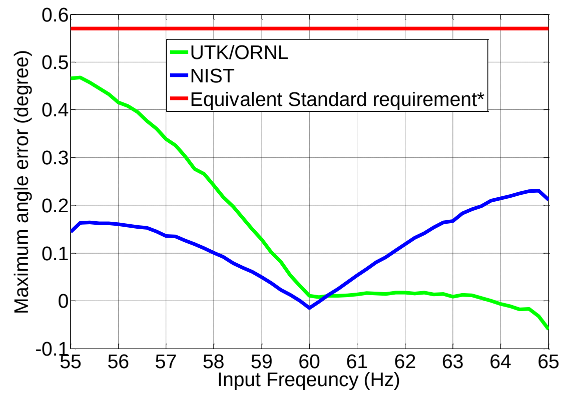

(b). Phase angle error

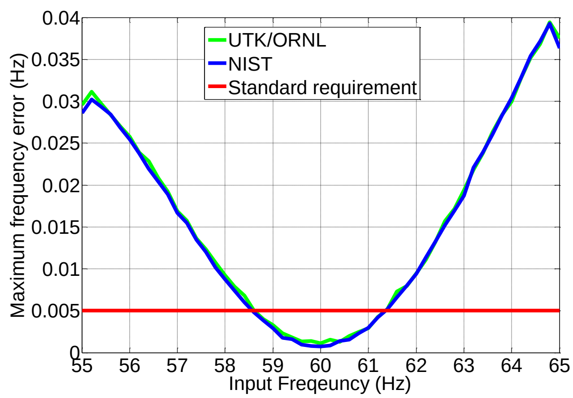

(c). Frequency error

Figure 6.2 PMU error under frequency range test

Since frequency errors at UTK/ORNL and NIST are close to each other but the TVE and phase angle errors are different under frequency range test, it is reasonable to assume the signal generated by Doble is delayed. This assumption can explain why the frequency errors at UTK/ORNL and NIST under frequency range test are close because frequency is the derivate of the angle and time delay of Doble will only cause a dc offset error for angle under frequency range condition. However, the frequency estimation will be affected by the time delayed signal under frequency ramp condition because frequency is a function of time under this condition, so we can see that the frequency errors at UTK/ORNL are different from those at NIST.

To verify the hypothesis, assuming the ideal signal generated by Doble under frequency range test is

$$Sig_{ideal} = Acos(2\pi ft + \theta) \tag{6.1}$$

Because of time delay caused by Doble, the actual signal generated by Doble is

$$Sig_{actual} = Acos(2\pi f(t - t_d) - \theta_d + \theta) \tag{6.2}$$

Then, the angle error caused by Doble is

$$Ang_E = Sig_{actual} - Sig_{ideal} = -2\pi ft_d - \theta_d \tag{6.3}$$

As a result, all the time dependent measurement data will be affected by the time delay of the signal. The time delay of Doble will result in inaccurate phasor error and TVE analysis under all the testing conditions, and inaccurate frequency errors analysis under some dynamic conditions including frequency ramp and phase modulation conditions. Since the errors caused by time delay is large, t_d and θ_d must be known and compensated to improve the accuracy of the PMU testing system.

As indicated in (6.3), the angle error caused by Doble is a function of the signal frequency, t_d, and θ_d, so if we know the signal frequency and the angle error caused by Doble under some different frequency conditions, it is possible to calculate t_d and θ_d. Figure 6.3 shows the angle errors of the PMU under frequency range test (55Hz to 65 Hz) at UTK/ORNL and NIST, respectively. Ang3 and Ang1 are the angle errors of the PMU under 55 Hz condition at UTK/ORNL and NIST, respectively, we can have

$$Ang3 - Ang1 = -2\pi 55 t_d - \theta_d \tag{6.4}$$

Similarly, under 65 Hz condition, we have

$$Ang4 - Ang2 = -2\pi 65 t_d - \theta_d \tag{6.5}$$

Then t_d and θ_d can be computed by

$$\begin{cases} t_{d\_cal} = \dfrac{(Ang3 - Ang1) - (Ang4 - Ang2)}{2\pi 10} \\ \theta_{d\_cal} = -\dfrac{65(Ang3 - Ang1) - 55(Ang4 - Ang2)}{10} \end{cases} \tag{6.6}$$

The computed t_{d_cal} and θ_{d_cal} are compensated in the signal generated in Doble. As a result, the signal generated by Doble has no time delay. In the following section, the testing results of UTK/ORNL will be compared to the results of NIST to verify the performance of the calibration method.

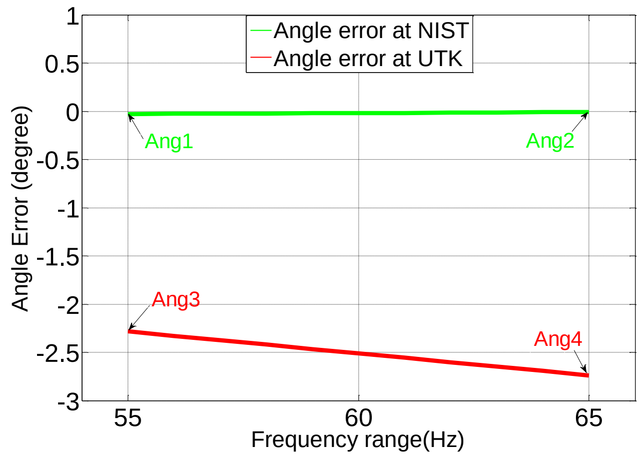

Figure 6.3 Angles for PSS calibration

6.3 Testing results

The PMU was tested again using the compensated signal, and the testing results are shown from Figure 6.4 to Figure 6.6. Figure 6.4 shows the testing results under frequency range test, the maximum TVE difference between UTK/ORNL and NIST is less than 0.02%, the angle difference is less than 0.02 degree, and the frequency difference is less than 0.0015 Hz.

Figure 6.5 shows the testing results under phase modulation condition, and the modulation index is 0.1 and the phase modulation varies from 0.1 Hz to 4.9 Hz. The maximum TVE difference, maximum angle error difference, and frequency error difference are less than 0.015%, 0.015 degree, and 0.002 Hz. The differences are small so that they can be ignored.

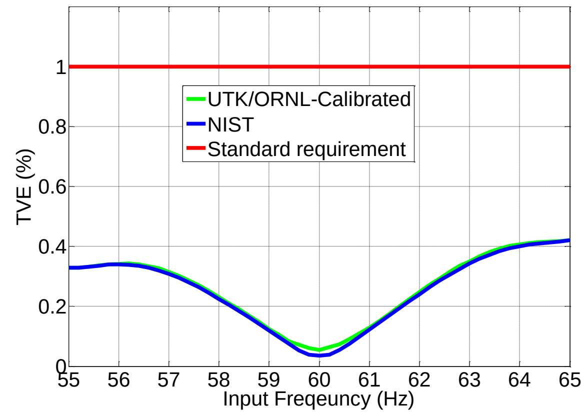

(a). TVE

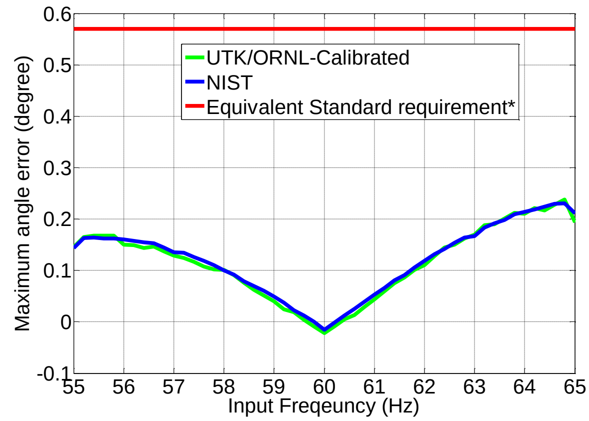

(b). Phase angle error

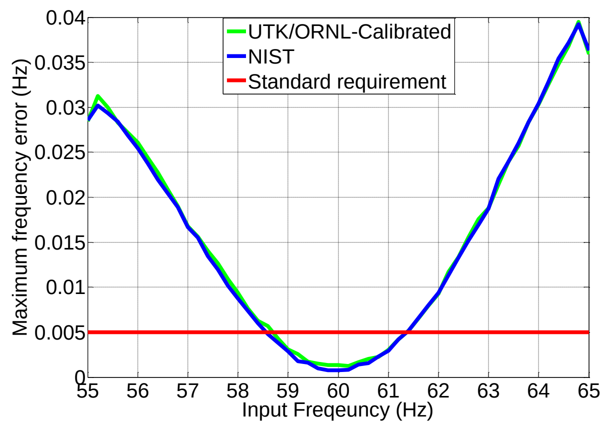

(c). Frequency error

Figure 6.4 Frequency range test

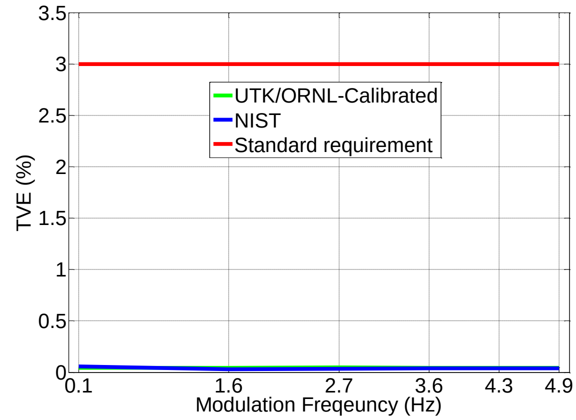

(a). TVE

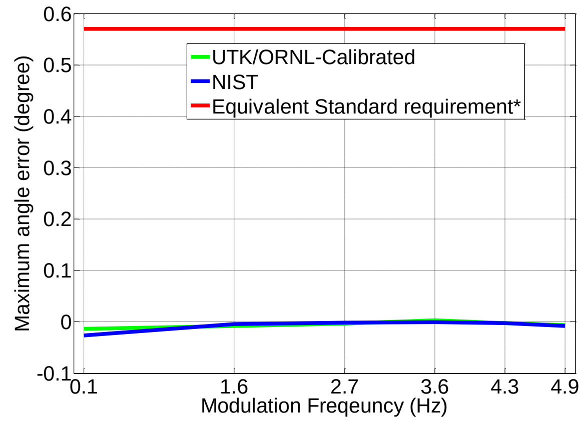

(b). Phase angle error

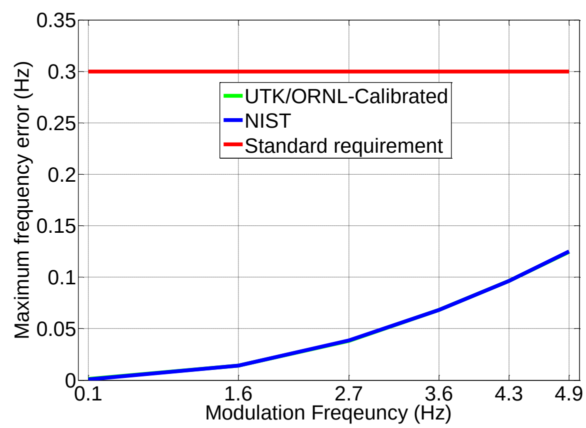

(c). Frequency error

Figure 6.5 Phase modulation test

Figure 6.6 shows the testing results under magnitude modulation condition, and the modulation index is 0.1 and the magnitude modulation frequency varies from 0.1 Hz to 4.9 Hz. The maximum TVE difference, maximum angle error difference, frequency error difference are less than 0.025%, 0.025 degree, and 0.001 Hz. The testing results at UTK/ORNL and NIST are very close to each other.

Table 6.2 shows the testing results under frequency ramp test, and the frequency ramps from 55 Hz to 65 Hz at a rate of 1Hz/s. Compared to Table 6.1, we can see the testing results are UTK/ORNL are much closer to the testing results at NIST.

Table 6.2 Frequency ramp test

	TVE (%)	Maximum angle error (degree)	Maximum frequency error (Hz)
NIST	0.2462	0.2487	0.0456
UTK/ORNL	0.2450	0.2407	0.0459

In conclusion, the time delay compensation method proposed in this chapter can greatly improve the accuracy of the signal generated by Doble. The PMU testing results under both steady-state and dynamic conditions are compared to the testing results at NIST to verify the capability of PMU testing system.

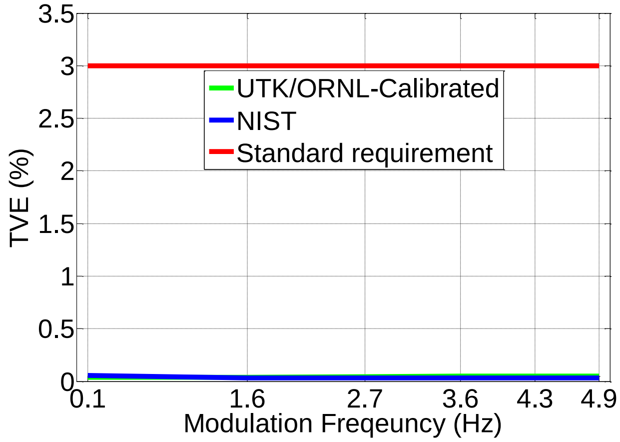

(a). TVE

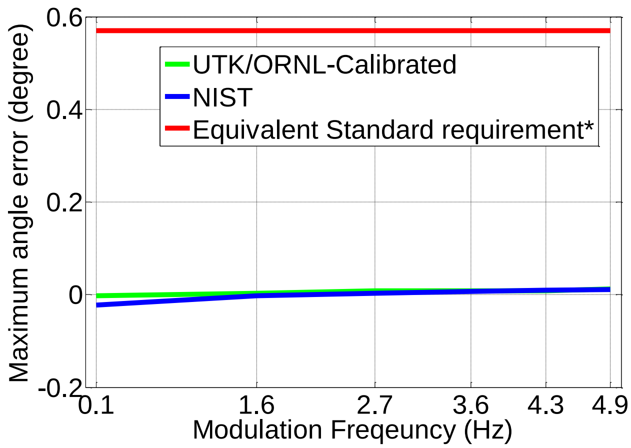

(b). Phase angle error

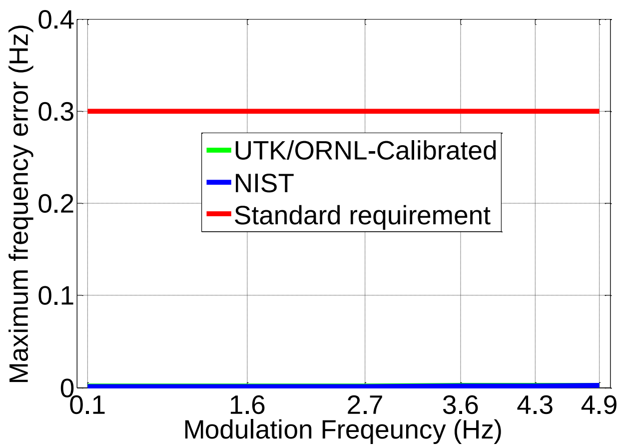

(c). Frequency error

Figure 6.6 Magnitude modulation test

6.4 Performance of the PMU under test

In this section, the measurement accuracy of the PMU under test is shown. It should be noted again that the PMU under test is not traceably calibrated.

NOMENCLATURE

$\mathbf{TVE}$: Total vector error

$\mathrm{MaxTVE\_VX}(\mathrm{X} = \mathrm{A}, \mathrm{B}, \mathrm{C}, +)$: Maximum voltage TVE of phase A, B, C, and positive sequence

$\mathrm{MaxTVE\_IX}(\mathrm{X} = \mathrm{A}, \mathrm{B}, \mathrm{C}, +)$: Maximum current TVE of phase A, B, C, and positive sequence

Min_FE: Minimum frequency errors

Max_FE: Maximum frequency errors

Min_RFE: Minimum rate of change of frequency errors

Min_RFE: Minimum rate of change of frequency errors

Note: The red curves represents the error limits according to IEEE PMU Standard.

6.4.1 Frequency range test

Figure 6.7 shows the measurement accuracy under frequency range test. We can see the PMU can meet the TVE requirement. However, the frequency and rate of change of frequency measurements do not comply with the Standard. The maximum frequency error is 0.04 Hz, and the maximum ROCOF error is 2.31 Hz/s. They are much higher than Standard requirements.

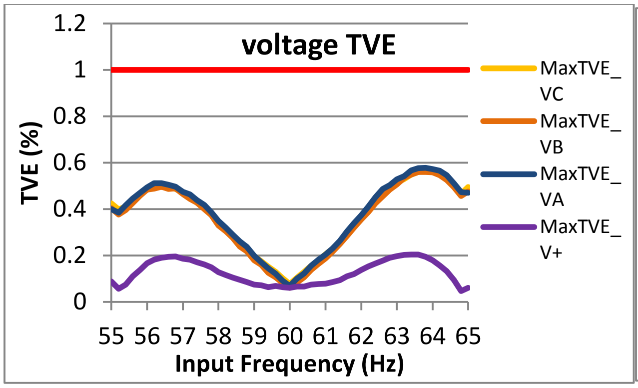

(a). Voltage TVE

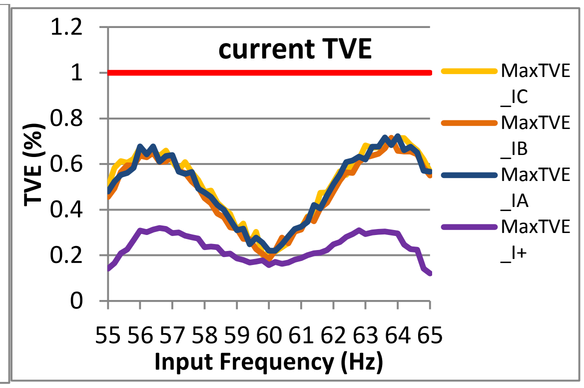

(b). Current TVE

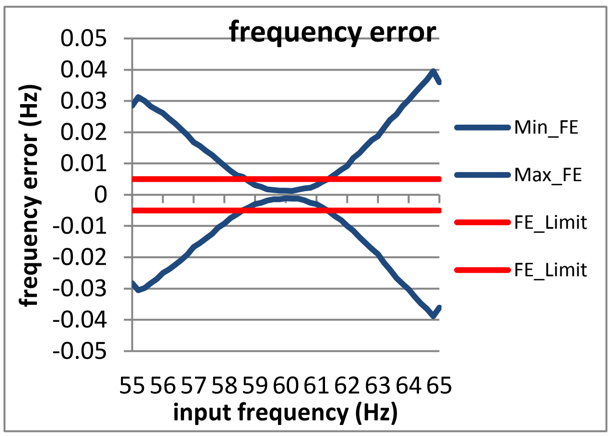

(c). Frequency error

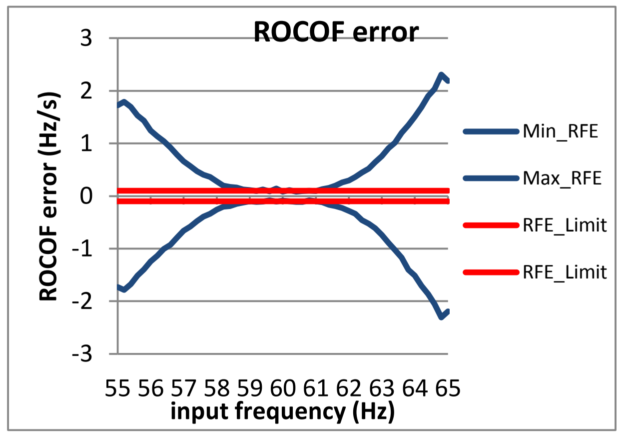

(d). ROCOF error

Figure 6.7 Frequency range test

6.4.2 Harmonic distortion test

Figure 6.8 shows the measurement accuracy under harmonic distortion test. We can see the PMU can meet the all the requirements in the Standard. It should be noted that in this test, the fundamental frequency is equal to 60Hz, and the frequencies of all the harmonic components are integer multiples of 60.

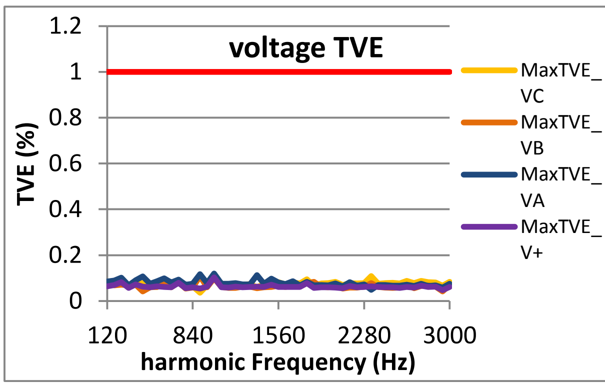

(a). Voltage TVE

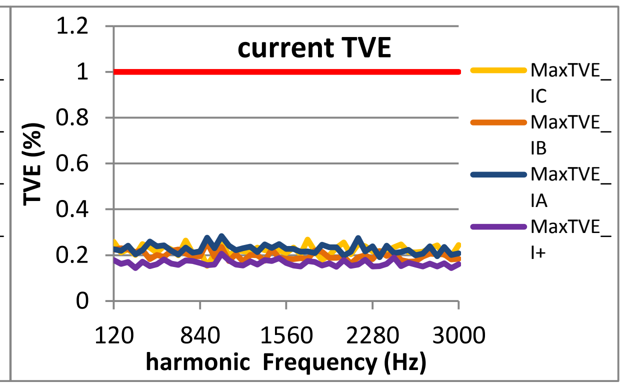

(b). Current TVE

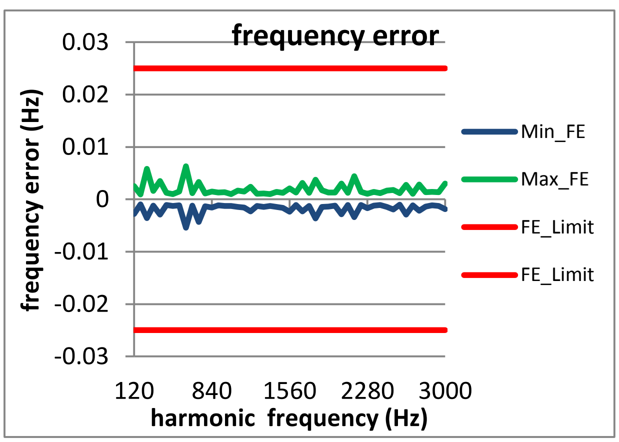

(c). Frequency error

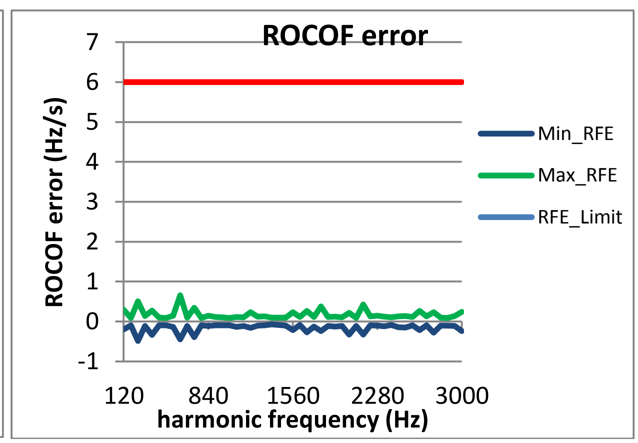

(d). ROCOF error

Figure 6.8 Harmonic distortion test

6.4.3 Out of band interference test

Figure 6.9 to Figure 6.11 shows the measurement errors under out-of-band interference test. We can see under the tests, the TVE can comply with the Standard. However, the frequency, and particularly ROCOF failed to pass the Standard.

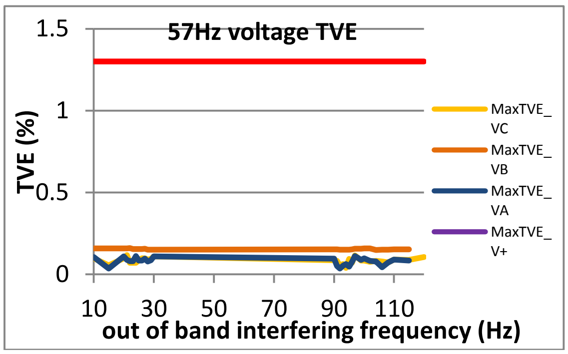

(a). Voltage TVE

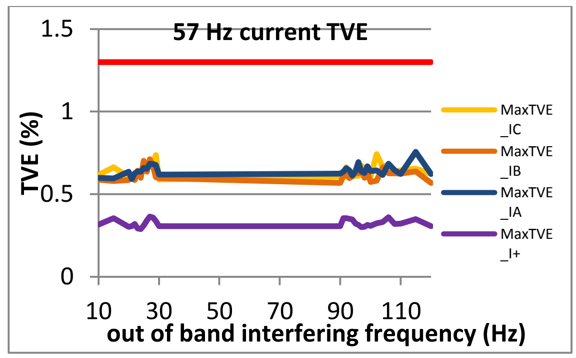

(b). Current TVE

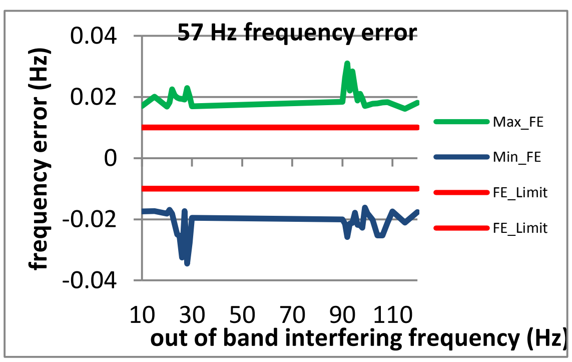

(c). Frequency error

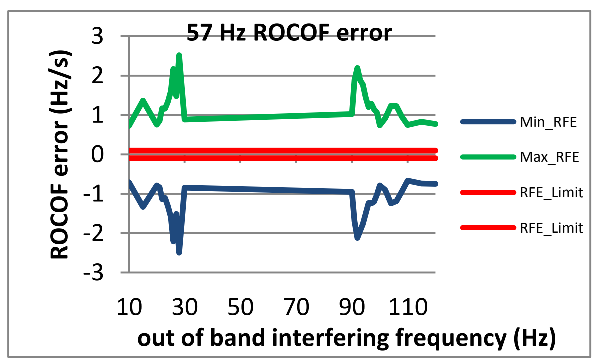

(d). ROCOF error

Figure 6.9 Out of band interference test under 57 Hz.

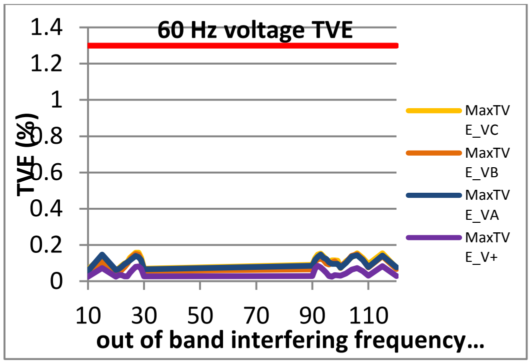

(a). Voltage TVE

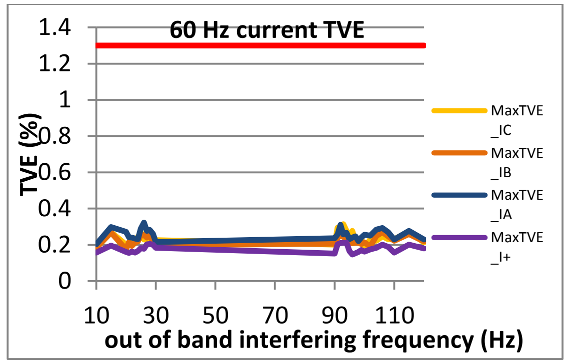

(b). Current TVE

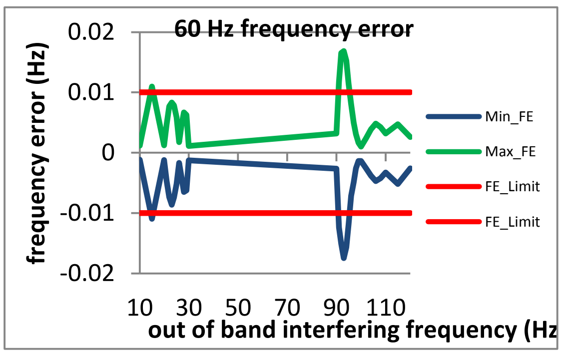

(c). Frequency error

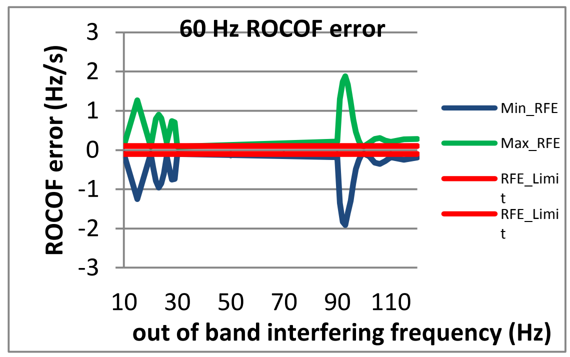

(d). ROCOF error

Figure 6.10 Out of band interference test under 60 Hz.

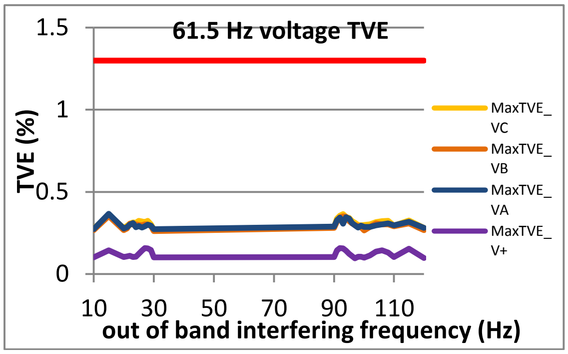

(a). Voltage TVE

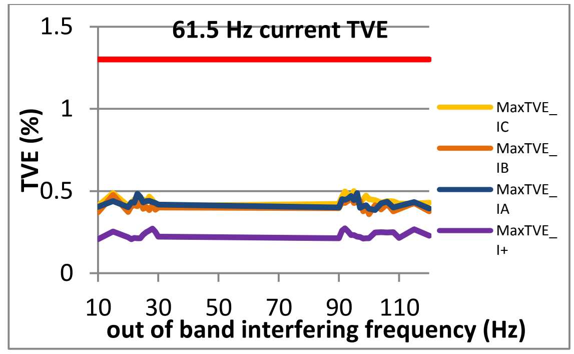

(b). Current TVE

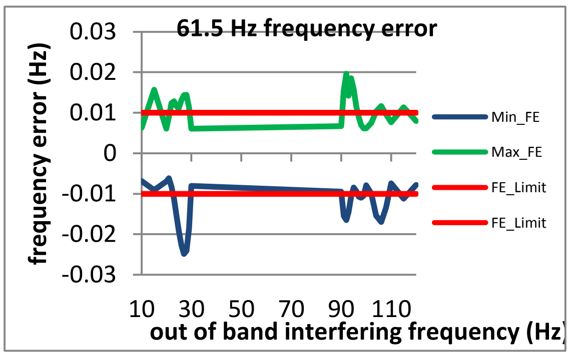

(c). Frequency error

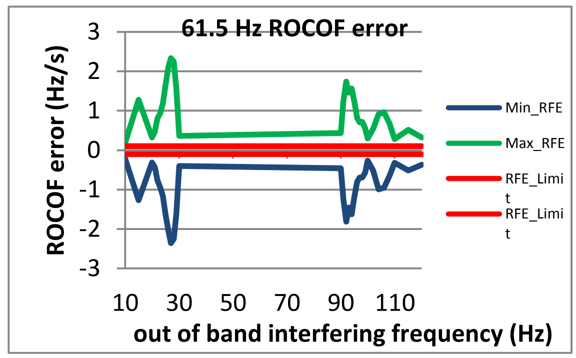

(d). ROCOF error

Figure 6.11 Out of band interference test under 61.5 Hz.

6.4.4 Magnitude modulation test

Figure 6.12 shows the measurement errors under magnitude modulation test. We can see that the PMU under test can pass the standard easily with a large margin.

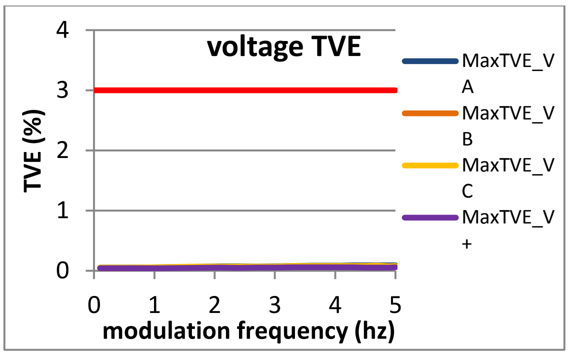

(a). Voltage TVE

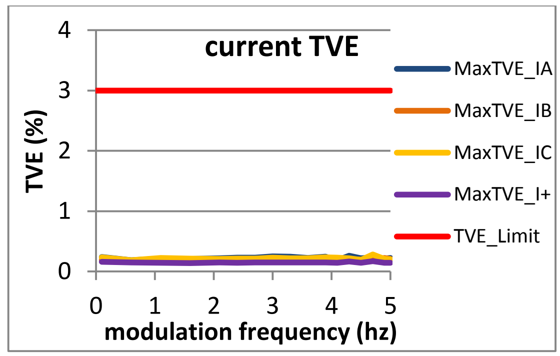

(b). Current TVE

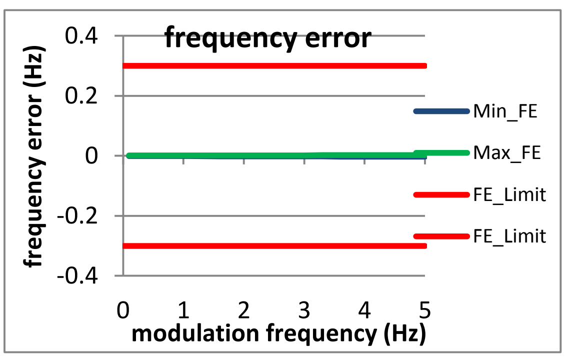

(c). Frequency error

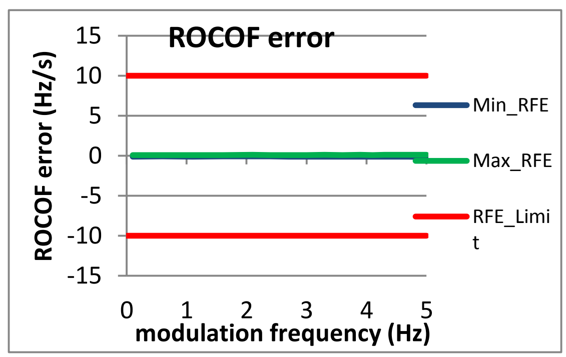

(d). ROCOF error

Figure 6.12 Magnitude modulation test

6.4.5 Phase modulation test

Figure 6.13 shows the measurement errors under phase modulation test. We can see that the voltage TVE and current TVE can pass the Standard. The frequency and ROCOF errors increase dramatically with the increase of modulation frequency, and they can pass the Standard but with a little margin.

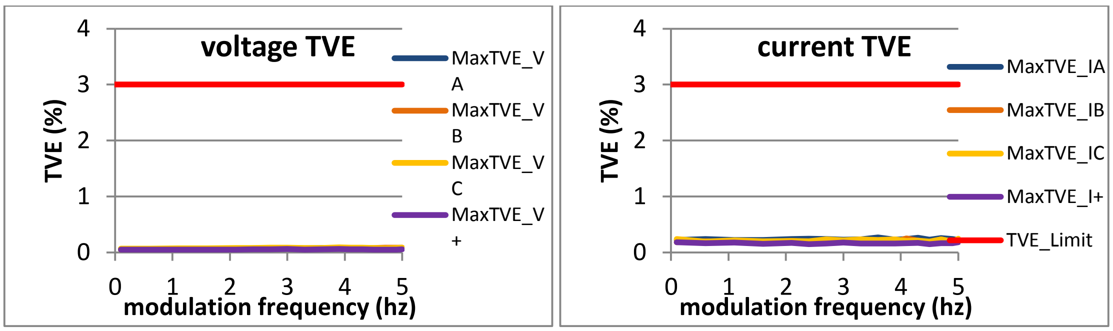

(a). Voltage TVE (b). Current TVE

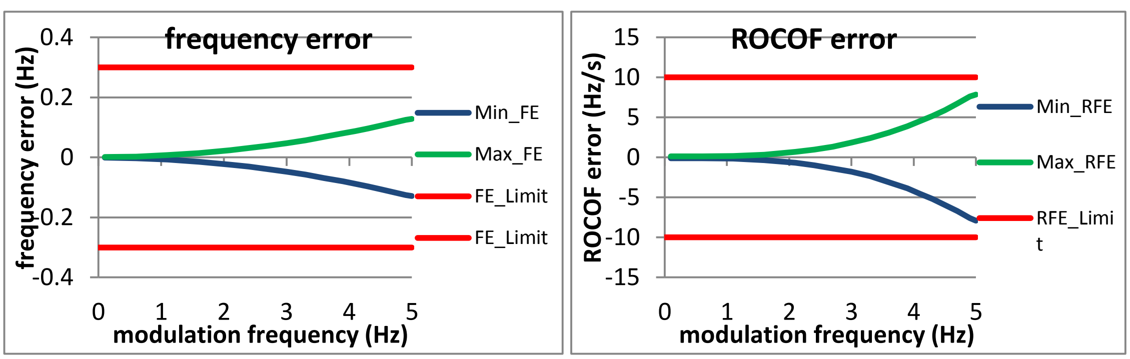

(c). Frequency error (d). ROCOF error

Figure 6.13 Phase modulation test

6.4.6 Summary

C37.118.1-2011 compliance of the PMU under test is shown in Table 6.3 and Table 6.4. The nominal frequency is 60 Hz and the reporting rate is 60Hz. In the tables, P means pass the PMU Standard, F means fail to pass the PMU Standard, and M means the magnitude percentage of the voltage or current signal. We can see that the PMU under test could pass the TVE requirement in most conditions. However, the FE and REF of the PMU under test failed in several conditions including frequency range test, magnitude modulation, out-of-band test, and frequency ramp test. In fact, the PMU Standard C37.118.1-2011 is too strict for PMU vendors to pass, an amendment version of PMU Standard, which is C37.118.1a-2014 was published in 2014. In the amendment [27], the measurement accuracy requirement for frequency and ROCOF was reduced.

Table 6.3 PMU Standard compliance of PMU under steady-state condition

<table>
<tr><td colspan="16">Steady State Test</td></tr>
<tr><td colspan="4">Frequency range test</td><td colspan="4">Signal magnitude test</td><td colspan="4">Harmonic distortion test</td><td colspan="4">Out of band test</td></tr>
<tr><td colspan="2">TVE</td><td>FE</td><td>RFE</td><td colspan="2">TVE</td><td>FE</td><td>RFE</td><td colspan="2">TVE</td><td>FE</td><td>RFE</td><td colspan="2">TVE</td><td>FE</td><td>RFE</td></tr>
<tr><td>V</td><td>P</td><td rowspan="2">Δf≤1.4: P
Δf>1.4: F</td><td rowspan="2">F</td><td>V</td><td>P</td><td rowspan="2">M=10%: F</td><td rowspan="2">F</td><td>V</td><td>P</td><td rowspan="2">P</td><td rowspan="2">P</td><td>V</td><td>P</td><td rowspan="2">F</td><td rowspan="2">F</td></tr>
<tr><td>I</td><td>P</td><td>I</td><td>P</td><td>I</td><td>P</td><td>I</td><td>P</td></tr>
</table>

Table 6.4 PMU Standard compliance of PMU under dynamic condition

<table>
<tr><td colspan="15">Dynamic State Test</td></tr>
<tr><td colspan="4">Amplitude modulation test</td><td colspan="4">Phase modulation test</td><td colspan="4">Frequency ramp test</td><td colspan="3">Step test</td></tr>
<tr><td colspan="2">TVE</td><td>FE</td><td>RFE</td><td colspan="2">TVE</td><td>FE</td><td>RFE</td><td colspan="2">TVE</td><td>FE</td><td>RFE</td><td>RT</td><td>DT</td><td>OS</td></tr>
<tr><td>V</td><td>P</td><td rowspan="2">P</td><td rowspan="2">P</td><td>V</td><td>P</td><td rowspan="2">P</td><td rowspan="2">P</td><td>V</td><td>P</td><td rowspan="2">F</td><td rowspan="2">F</td><td rowspan="2">P</td><td rowspan="2">P</td><td rowspan="2">P</td></tr>
<tr><td>I</td><td>P</td><td>I</td><td>P</td><td>I</td><td>P</td></tr>
</table>

6.5 Conclusion

In this chapter, the PMU testing system in UTK/ONRL was introduced. Collaborating with NIST, a PMU was tested in the laboratory. The testing results are compared with the results from

NIST. Based on the comparison results, a calibration was proposed to calibrate the PMU testing system in UTK/ORNL. The new testing results demonstrated that the calibration method can effectively calibrate the PMU testing system in UTK/ORNL.

The measurement accuracy of the PMU under test was evaluated by the PMU testing system in UTK/ORNL. The testing results show that the current PMU Standard is very hard to pass, particularly for frequency and ROCOF measurement. In the latest PMU Standard C37.118.1a-2014, which is an amendment to C37.118.1-2011, the measurement accuracy requirements are decreased.

Chapter 7 Development of Universal Grid Analyzers

7.1 Introduction

To better understand the power grid dynamics and power quality at the distribution level, a concept of "Universal Grid Analyzers (UGA)" was proposed. The UGA is a real-time, highly accurate, and GPS synchronized power grid monitoring device used at distribution level. They can function as a power quality analyzer by performing harmonics measurement, voltage sag and swell detection. They can also be used as a FDR at the distribution level. Moreover, as discussed in Chapter 4, the noise can cause phasor estimation errors, and this is not discussed in the PMU Standard. Therefore, to better understand the noise of power grid signals at the distribution level, the noise analysis function is developed for the UGA to analyze the power grid signals at distribution level. This function can provide important information for analyzing true synchrophasor measurement errors at the distribution level.

In this chapter, the hardware architecture of the UGA is introduced first. The adaptive synchronous sampling architecture is presented in 7.2. The software architecture and algorithm are introduced in 7.3. The UGA data format and server is presented in 7.4. Experimental results are shown and discussed in 7.5. At last, a method that can further verify the effect of noise on measurement accuracy is introduced in 7.6.

A photo of the prototype UGA is shown in Figure 7.1. The hardware of the prototype UGA is based on the new FDR, but with new software. It mainly consists of a power module, a data acquisition module, a GPS receiver, a digital signal processor (DSP), An ARM microprocessor, An Ethernet transceiver, and an LCD. Figure 7.2 shows the hardware architecture of the UGA. The voltage transducer takes an analog voltage signal from a 120V wall outlet and converts it to ADC acceptable voltage level. The anti-aliasing filter eliminates the high frequency components, and the analog to digital converter (ADC) transforms the analog signal to digital data. The DSP is used to provide synchronous sampling conversion signal that is synchronized to coordinated universal time (UTC) for ADC. All the measurement functions are also implemented on the DSP. The measurement data from the DSP are transmitted to the ARM through Serial Peripheral Interface (SPI), and then they are time stamped by the ARM. The data are then transmitted to the Ethernet receiver and sent to UGA server via the Internet.

Figure 7.1 A photo of the prototype UGA

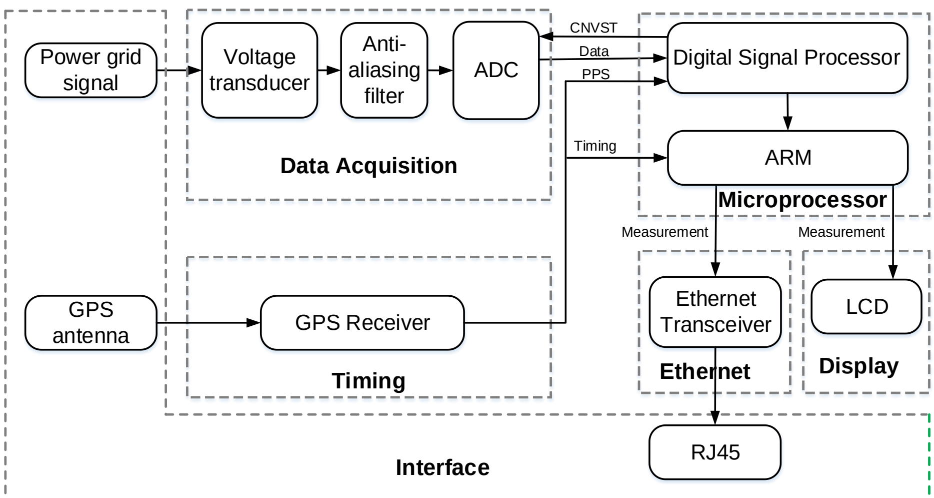

Figure 7.2 Flowchart of the UGA

7.2 Adaptive synchronous sampling architecture

Synchrophasor measurement is one of UGA's core functions, and highly accurate synchronous sampling is at the heart of the hardware and crucial to phasor measurement accuracy. Different synchronous sampling methods have been proposed [55]-[57]; Phase-locked loop (PLL) is one of the common methods. In order to achieve PLL, an extra chip such as an FPGA or CPLD is usually required, and it is difficult to change sampling frequency in real-time. In the UGA, a method is proposed to achieve accurate and flexible synchronous sampling based on existing hardware of the UGA without adding extra hardware devices.

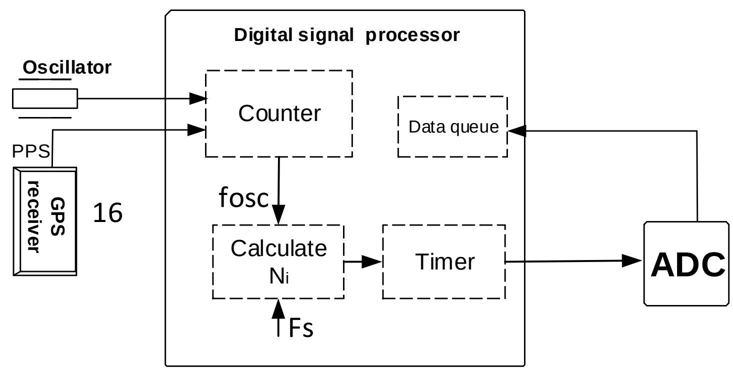

Figure 7.3 Adaptive synchronous sampling architecture

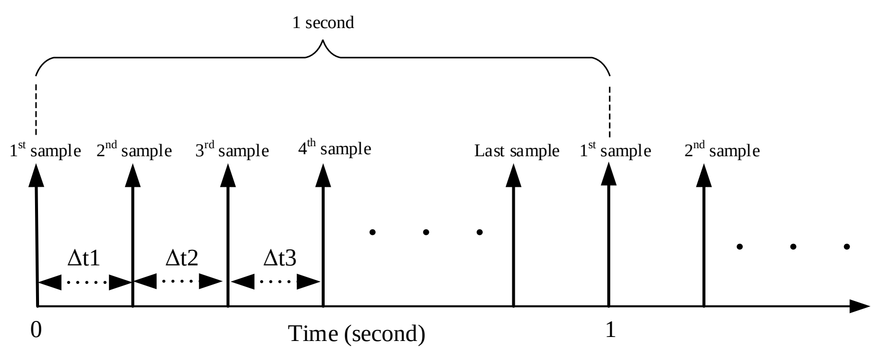

Figure 7.4 Illustration of synchronous sampling

Figure 7.3 shows the hardware architecture of the method. The proposed synchronous sampling method only uses a pulse per second (PPS) signal from the GPS receiver, a 50 MHz oscillator, and a DSP. The PPS signal is used to initiate an analog to digital conversion through the conversion start pin (CNVST) of the ADC at the beginning of each second; this ensures that the time of first sample in each second is aligned to PPS. From the second sample to last sample in one second, the CNVST of ADC is generated by the interrupt of a timer in DSP. Since the time of the first sample is aligned to the PPS signal, synchronous sampling can be achieved by controlling the time interval between two consecutive samples as shown in Figure 7.4. The time interval can be controlled by modifying the value of Period Register (PR) of the timer,

$$\Delta t_{i-1} = \frac{N_i}{f_{osc}}, \qquad i = 2, \dots, F_s \tag{7.1}$$

where Δt_{i-1} is the time interval between (i-1)th and ith samples. N_i is the value of PR, f_{osc} is the estimated clock frequency of the oscillator, F_s is the number of samples in one second.

In practical implementation, the clock frequency of the oscillator is not a constant number and may vary with temperature, and value of PR must be an integer. As a result, actual sampling rate is probably not exactly equal to the ideal sampling rate F_s. For example, if a 50 MHz oscillator is used in the UGA, and the actual frequency of this oscillator is about 49999454 Hz. If a sampling rate of 5.76 kHz is required, then the value of PR is

$$N_{PR} = \frac{f_{osc}}{F_s} = \frac{49999454}{5760} \approx 8680.46076389 \tag{7.2}$$

Note that the ideal period register value N_{PR} is not an integer, and using either 8680 or 8681 will cause sampling error. If 8680 is used, the sampling error of ith sample in one second is

$$Te_i = \frac{N_{PR} - 8680}{f_{osc}} \times (i-1) = \frac{0.46076389}{49999454} \times (i-1), \mathrm{i} \leq n \leq 5760 \tag{7.3}$$

The sampling error of the last sample of one second is

$$Te_{5760} = \frac{0.4607638}{49999454} \times 5759 \ \approx 53.07\ (\mu\mathrm{s}) \tag{7.4}$$

The angle error caused by 53.07 μs error for 60Hz power system is $53.07 \times 10^{-6} \times 360 \times 60° = 1.1463°$, which exceeds the 1% TVE requirement in the PMU Standard.

In order to achieve accurate sampling frequency, it is first important to accurately measure the oscillator frequency f_{osc}. In the proposed method, f_{osc} is monitored in real-time using PPS signal and a counter in the DSP as shown in Figure 7.3. The counter is triggered by the rising edge of one PPS signal, and stopped by the rising edge of a following PPS signal. Assuming the time between two consecutive PPS signals is one second, then the value of the counter is equal to oscillator frequency. Note that as the oscillator frequency is monitored and updated every second, the temperature sensitivity of the oscillator will not affect the sampling accuracy.

More importantly, ideally N_{PR} is probably not an integer. Although N_i must be an integer at every sample point, the average value of N_i in one second can be a non-integer by alternating two consecutive integers at a certain proportion. Assuming N_L is the nearest integer towards minus infinity of N_{PR}, and N_H is the nearest integer towards infinity of N_{PR}, which is 8680 and 8681, respectively, in the UGA. For each sample in one second, either N_L or N_H is used as the value of PR. The criteria to select N_L or N_H is

$$N_i = \begin{cases} N_L & \left(if \left|\sum_{k=2}^{i-1}(N_k) + N_L - (i-1)N_{PR}\right| < \left|\sum_{k=2}^{i-1}(N_k) + N_H - (i-1)N_{PR}\right|\right) \\ N_H & \left(if \left|\sum_{k=2}^{i-1}(N_k) + N_L - (i-1)N_{PR}\right| \geq \left|\sum_{k=2}^{i-1}(N_k) + N_H - (i-1)N_{PR}\right|\right) \quad , i \geq 3 \\ round\left(\frac{f_{osc}}{F_s}\right) & , i = 2 \end{cases} \tag{7.5}$$

where N_i is the actual value of PR for ith sample in one second. $round\left(\frac{f_{osc}}{F_s}\right)$ rounds $\frac{f_{osc}}{F_s}$ to nearest integer for the second sample in one second. From the third sample to last sample in one second, the value of PR is selected by comparing $\left|\sum_{i=2}^{i-1}(N_k) + N_L - (i-1)N_{PR}\right|$ with $\left|\sum_{i=2}^{i-1}(N_k) + N_H - (i-1)N_{PR}\right|$. The criteria can insure that maximum sampling error of all the samples in one second is less than $1/2f_{osc}$. Figure 7.5 (a) shows the first twenty N_i in one second, we can see that the N_i alternates between 8680 and 8681. Figure 7.5 (b) shows the sampling errors of all the samples in one second, and it can be seen that sampling error does not accumulate over time, and the maximum sampling error is less than $1/2f_{osc} \approx 10\ (ns)$. The angle error caused by 10 ns error is only $10 \times 10^{-9} \times 360 \times 60° \approx 0.0002°$.

Another factor that affects the accuracy of synchronous sampling is signal to noise ratio (SNR) of the sampling circuit. In the prototype UGA, a 16-bit SAR ADC with ultrahigh precision bandgap voltage reference is used instead of a 14-bit ADC with internal voltage reference that is used in FDRs. The SNR of the sampling circuit can be improved from 78 dB to 90 dB theoretically.

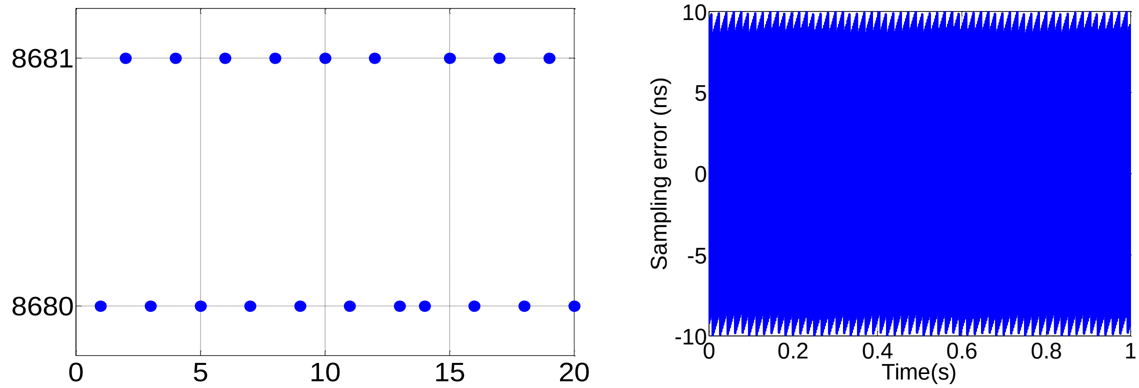

(a). N_i (b). Sampling errors in one second

Figure 7.5 N_i and sampling errors

7.3 Software architecture and algorithms of the UGA

The embedded microprocessors of the UGA consist of an ARM and a DSP. Basically, the ARM receives the measurement results from the DSP, parses timing information from the GPS receiver, wraps the measurements and time stamps, and then sends the data to the Ethernet transceiver. The DSP is mainly used for measurement and synchronous sampling. The ARM and DSP program flowcharts are shown in Figure 7.6 and Figure 7.7, respectively.

The $main$ () loop of ARM program starts with initializing the variables and peripherals before repeating the infinite loop that checks the status of the $HaveNewDataFlg$ variable, which is set to true by the SPI interrupt upon the arrival of a new measurement data transmitted from the DSP. There is another infinite loop to wait the recovery of the GPS signal. When the $HaveNewDataFlg$ variable is refreshed by the SPI interrupt service routine (ISR) and GPS_Status is set to be ready, the ARM program generates the newest data package. Then, the packet is sent to the Ethernet transceiver, which is the module to send the data to the UGA server via the Internet.

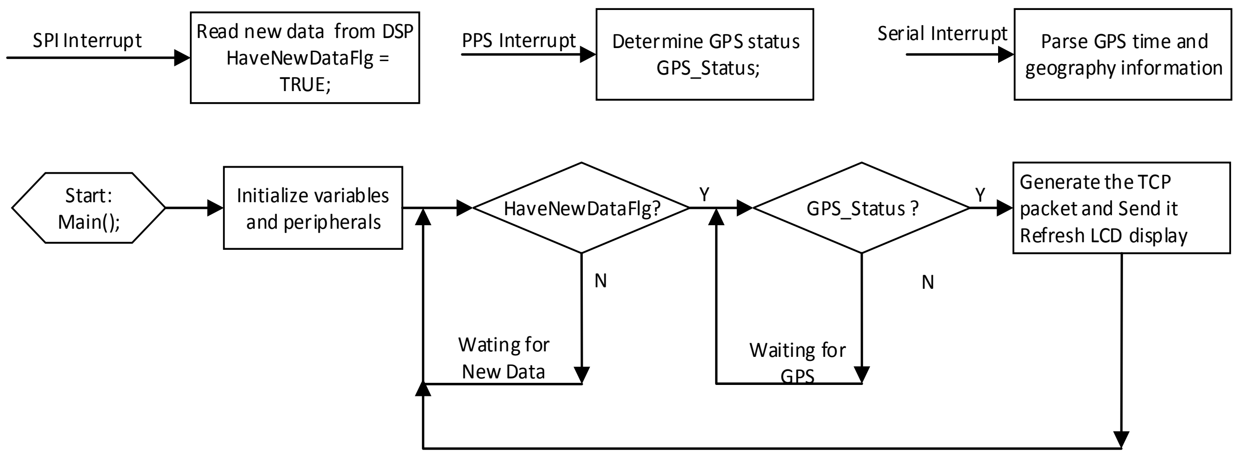

Figure 7.6 ARM program flowchart of the UGA

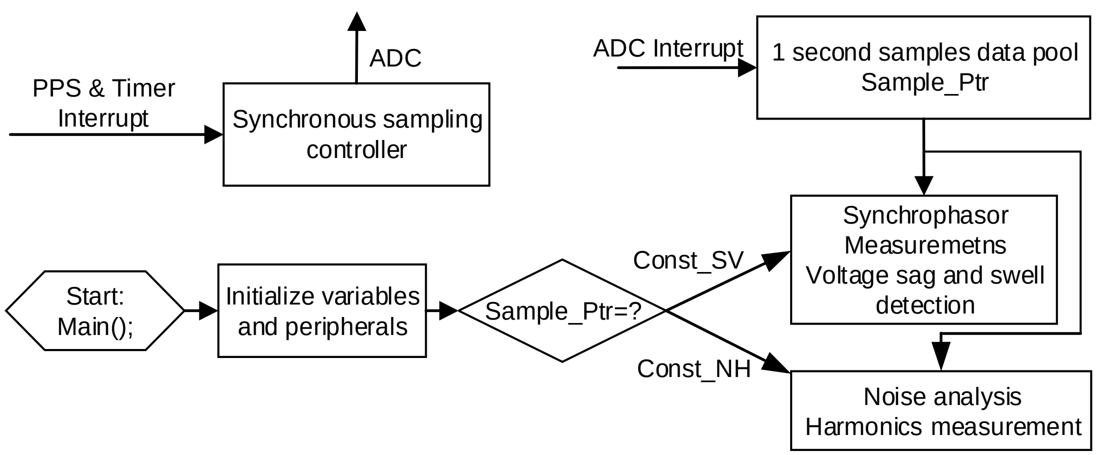

Figure 7.7 DSP program flowchart of the UGA

There are two major parts of the DSP program, the ISR and the main function, respectively. The PPS & timer interrupt routine generates sampling conversion signal CNVST for the ADC. The ADC interrupt transmits sample data to a data queue with one second data size in the DSP, and $Sample\_Ptr$ is a pointer that points to the newest sample. DSP resets $Sample\_Ptr$ to 0 at the beginning of each second. The $main()$ loop runs continuously, and executes different measurement function by comparing $Sample\_Ptr$ with two constants: $Const\_SV$ and $Const\_NH$. The program will execute synchrophasor measurement, voltage sag and swell detection functions when $Sample\_Ptr$ is equal to constant $Const\_SV$, and noise analysis and harmonics measurement functions when $Sample\_Ptr$ is equal to constant $Const\_NH$. In the UGA, synchrophasor measurement and voltage sag and swell detection functions are executed once every 0.1 second, so

$$\text{Const\_SV} = 0.1 f_s \times i \qquad , i = 0, \ldots, 9 \tag{7.6}$$

Noise analysis and harmonics measurement functions are executed once every second, so

$$\text{Const\_NH} = 0.5 f_s \tag{7.7}$$

The two functions are executed at 0.5 second of each second.

A. Noise analysis and harmonics measurement

As the noise and harmonics analysis method presented in 4.1, the modified periodogram method is adopted to calculate power spectral density (PSD) of the power grid signal in frequency domain and implemented in DSP. The equation used to calculate PSD is

$$P_{xx}\left(\frac{k}{N}\right) = \frac{1}{N}\left|\sum_{N=0}^{N-1} h(n)x(n)e^{-j2\pi nk/N}\right|^2, \quad k = 0, 1, \ldots, N-1 \tag{7.8}$$

In the UGA, 0.5 second data is used as the window size, so N is equal to $f_s/2$ and the frequency resolution is 2 Hz. As a result, the ith order of harmonics can be obtained by substituting k with $(30i + 1)$ in (7.8).

B. Voltage sag/swell detection

The voltage sag and swell is defined in IEC 61000-4-30 [58], In the UGA, the method recommended in the Standard is adopted to detect voltage sag and swell. The RMS of voltage signal is calculated every half fundamental frequency cycle, which is represented by

$$U_{RMS} = \sqrt{\frac{1}{N_{RMS}} \sum_{i=1}^{N_{RMS}} {x_i}^2} \tag{7.9}$$

where N_{RMS} is the number of samples used for RMS calculation, and it is equal to half of number of samples in per fundamental frequency cycle. The sliding window of RMS calculation is also equal to N_{RMS}. As a result, the RMS of voltage signal is calculated 120 times for 60Hz grid. Flags are used to indicate the occurrence of voltage sag or swell. Each voltage sag and swell flag is one byte. The first two bits are starting bits, and they are equal to 11, the following six bits indicate the status of voltage sag and swell. 0 means that no voltage sag or swell occurs, and 1 means voltage sag or swell occurs. Figure 7.8 shows an example of the flags for six cycles of data. The nominal voltage is 120V. The voltage sag threshold is 110V, and the voltage swell threshold is 130V. When the voltage is less than 110V, the voltage sag flag is 1, otherwise it is 0. When the voltage is greater than 130V, the voltage swell flag is 1, otherwise it is 0. As shown in Figure 7.8, the voltage sag flag is 0xfc, 0xc0, and the voltage swell flag is 0xc0, 0xcf.

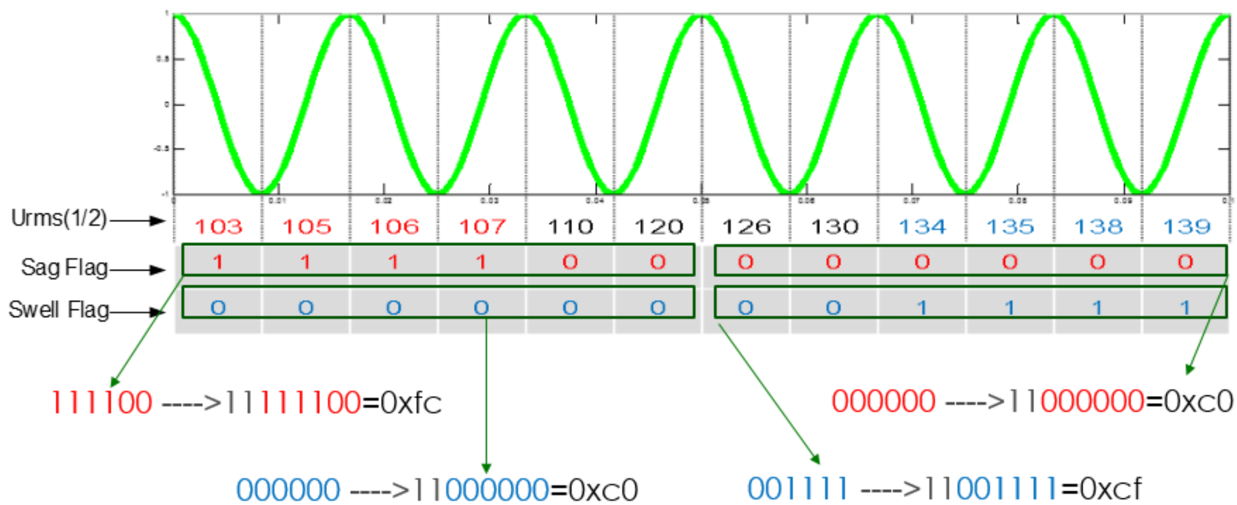

Figure 7.8 Flag of voltage sag and swell.

7.4 UGA data format and UGA server

7.4.1 UGA data format

The UGA data is transmitted from UGA to UGA server through Ethernet. The data rate is 10Hz per second. Figure 7.9 shows an example of the UGA data in one second. The data frame is divided into five segments. The first segment is the Unit ID, which is “1” in the example; The second segment is the time information. For example, 101414 190717 1 means 19:07:17.1, Oct. 14, 2014. The third segment represents the synchrophasor results, and the four columns in this segment represent first frequency, second frequency, voltage magnitude, and voltage phase angle, respectively. The fourth segment includes the harmonics and THD. The first eight data frames of one second data include 3rd, 5th, 7th, 9th, 11th, 13th, 15th order of harmonics, and THD respectively. The last two samples are reserved. As shown in Figure 7.9, the 3rd, 5th, 7th, 9th, 11th, 13th, and 15th order of harmonics is 0.42%, 1.45%, 0.22%, 0.06%, 0.23%, 0.04%, and the THD is 1.56%. The fifth segment is the voltage sag and swell flags. The first two columns are voltage sag flags, and the last two columns are voltage swell flags. Since there are six cycles in per 0.1 second and voltage magnitude is calculated 12 times in this period, two bytes are needed to indicate the status of voltage sag and swell, respectively in per 0.1 second.

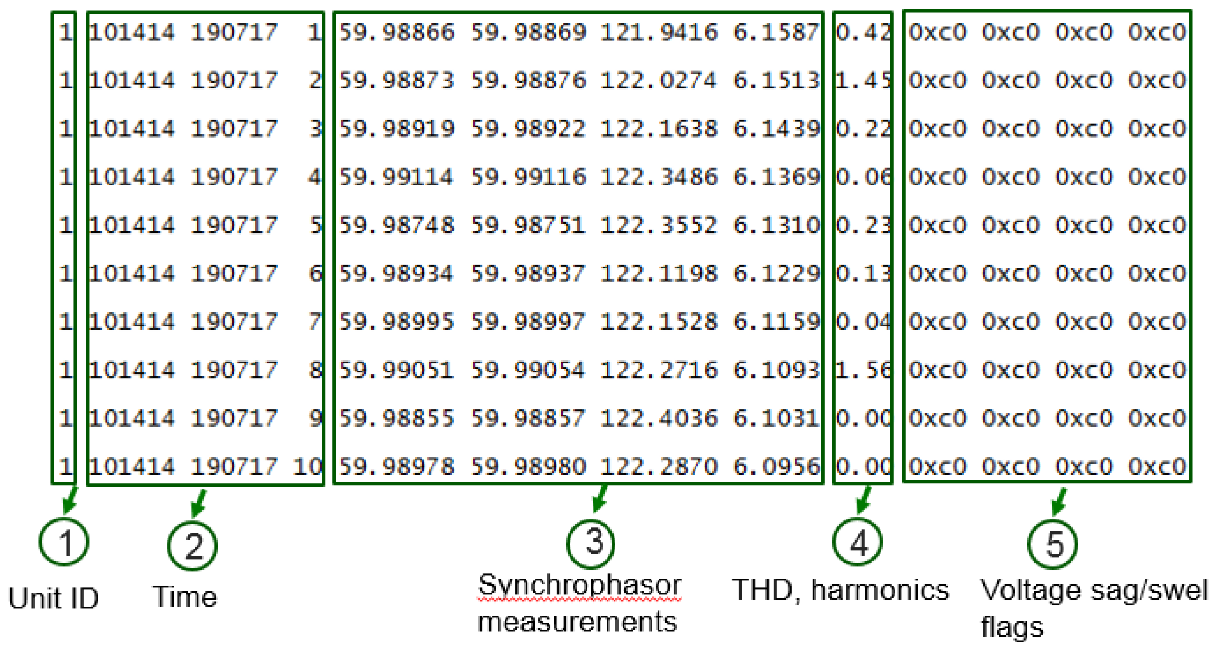

Figure 7.9 UGA data format

7.4.2 UGA server

In order to test the communication of prototype UGA, a UGA server was developed using Python. The server parses the UGA data in real-time and save the data in txt file. Figure 7.9 shows an example of the UGA data in txt file. The python code is given in Appendix B.

7.5 Testing of prototype UGA

A prototype UGA was built and tested in Power IT Laboratory. The test includes synchrophasor measurement accuracy, noise analysis, voltage sag/swell, and harmonics measurement.

7.5.1 Synchrophasor measurement accuracy

The accuracy of the proposed synchronous sampling method was analyzed in 7.2. Since the accuracy of synchronous sampling affects synchrophasor measurement accuracy, the angle and frequency measurement errors using the adaptive synchronous sampling method and manual-calibration synchronous sampling method [34] are compared. In order to compare the results in detail, the angle and frequency is calculated at a rate of sampling rate, which means that the reporting rate of the angle and frequency is equal to sampling rate. In this test, the sampling rate is 1440 Hz/s. The testing results are shown in Figure 7.10. Table 7.1 summarizes the standard deviation (STD) and maximum errors.

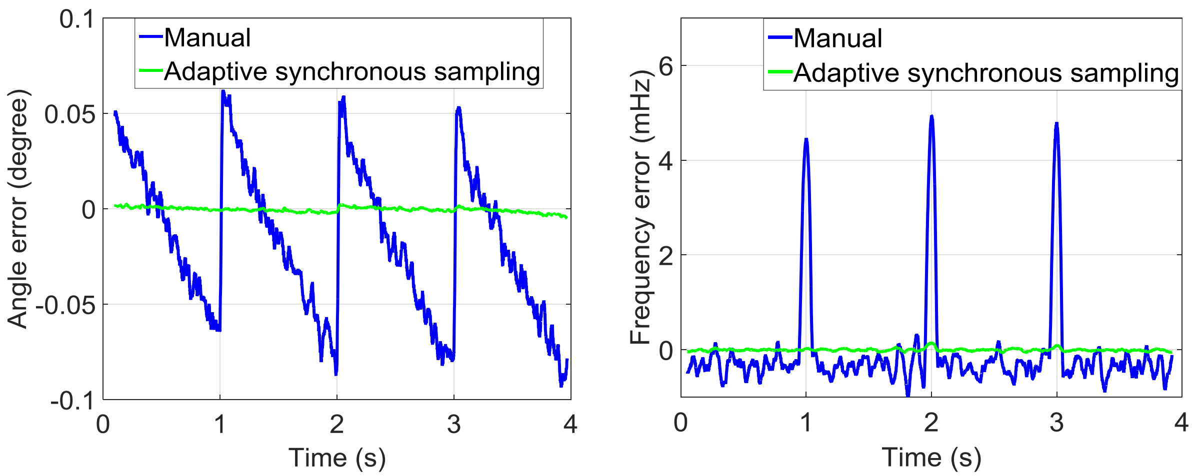

(a). Angle errors (b). Frequency errors

Figure 7.10 Comparison of manual calibration and adaptive synchronous sampling method

According to the results shown in Figure 7.10 and Table 7.1, we can see that the adaptive synchronous sampling method and new sampling circuit greatly reduced the measurement errors. More importantly, obvious frequency and angle error spikes occur once every second for manual calibration method due to accumulated sampling errors in one second. In contrast, the adaptive synchronous sampling method can greatly reduce the spikes.

Table 7.1 Comparison of manual calibration and adaptive synchronous sampling method

Device under test	Angle errors (degree)		Frequency errors (mHz)	
	STD	MAX	STD	MAX
Manual calibration	0.0378	0.0937	1E-3	4.94
Adaptive synchronous sampling method	0.0012	0.0049	2.8E-5	0.15

Furthermore, the UGA is compared to a commercial PMU. Since the commercial PMU cannot output the results at a rate equal to sampling rate, 10 Hz reporting rate is used for comparison. Figure 7.11 shows the measurement errors of the UGA and PMU, we can see that the measurement accuracy of the UGA outperforms the PMU, though the UGA uses only single phase signal for calculation and PMU normally uses three phase signals. Note that for the commercial PMU under test, we can still see the frequency and angle spike at the end of each second while the spikes are much smaller in the UGA.

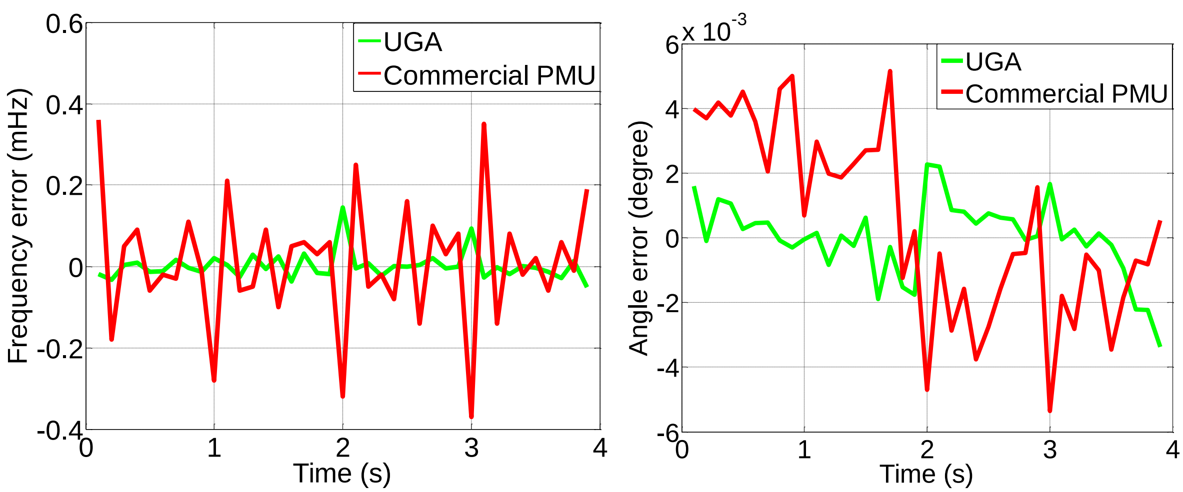

(a). Angle errors b). Frequency errors

Figure 7.11 Angle and frequency errors of the UGA and PMU

The requirement of maximum frequency measurement errors is 5 mHz in the PMU Standard. The frequency measurement errors due to the hardware and synchronous sampling of UGA are much lower than the requirement. In addition, the PMU Standard does not have an angle measurement accuracy requirement, and TVE is used instead for phasor measurement accuracy. The corresponding TVE error caused by 0.0049 degree angle error of the UGA is

$$TVE = \sqrt{\frac{(\cos 0.0049 - 1)^2 + (\sin 0.0049)^2}{1}} \approx 0.0086\% \tag{7.10}$$

Compared to the 1% TVE requirement in the PMU Standard, the TVE error of the UGA is very low. Thus, the hardware platform of the UGA provides the potential to develop a highly accurate synchrophasor measurement device that far exceeds the accuracy requirements in the PMU Standard in the future.

7.5.2 Noise analysis

The UGA was connected to a 120V outlet in the laboratory to analyze power grid signals at distribution level.

Figure 7.12 (a) shows PSD of the power grid signal, and we can see that the power grid signal contains noise as well as 60 Hz components and harmonic components. To study the effect of noise and harmonics on measurement accuracy, the noise and harmonics of the power grid signal are calculated by the noise analysis function, then the same amount of noise and harmonics are used to generate an artificial signal with known fundamental frequency component, which is

$$Sig = A_0 \cos(2\pi f_0 + \varphi_0) + \sum_{i=2}^{N} A_i \cos(2\pi i f_0 + \varphi_i) + \omega(t) \tag{7.11}$$

where $A_0 \cos(2\pi f_0 + \varphi_0)$ is the fundamental frequency component. A_0 , f_0 , and φ_0 are predetermined parameters. $A_i \cos(2\pi i f_0 + \varphi_i)$ is the ith-order harmonic component, and $\omega(t)$ is the noise of the power grid signal. A_i and $\omega(t)$ are obtained by noise analysis function, and phase angle φ_i is a random number between 0 to 2π. In order to verify that the artificial signal can represent the original power grid signal, the PSD of the artificial signal is compared to the PSD of the original power grid signal, and results are shown in Figure 7.12 (b). We can see that the PSD of the artificial signal can match the original power grid signal well. Then, the frequency and angle of the artificial signal are estimated by the UGA's synchrophasor measurement algorithm. Since the frequency and angle of the artificial signal are known parameters, it is easy to calculate the frequency and angle estimation errors, and the errors are shown in Figure 7.13. We can see that the angle and frequency measurement errors of the UGA in the field application are about 0.01 degree and 0.4 mHz, respectively.

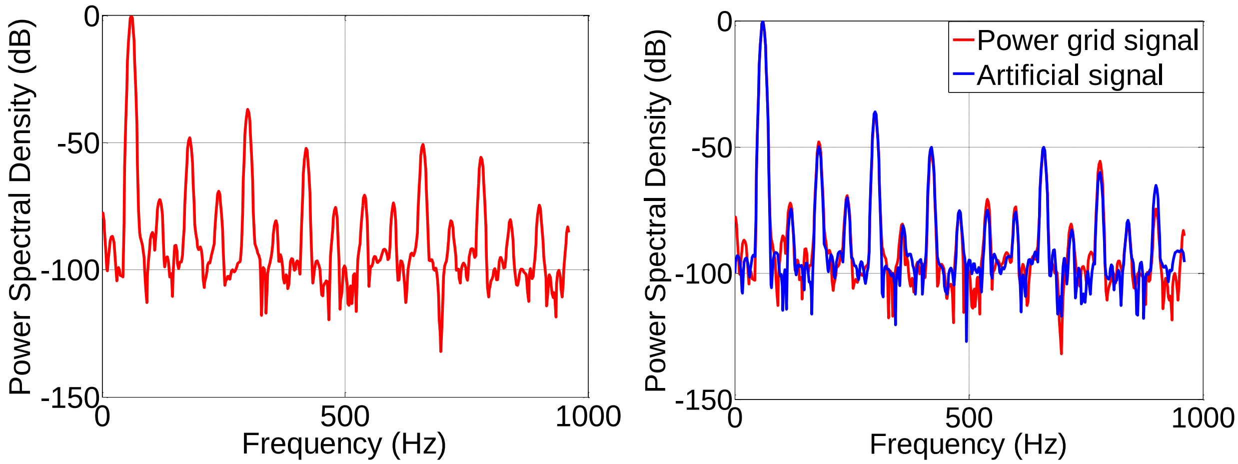

(a). PSD of power grid signal (b). PSD of power grid signal and artificial signal

Figure 7.12 PSD of power grid signal

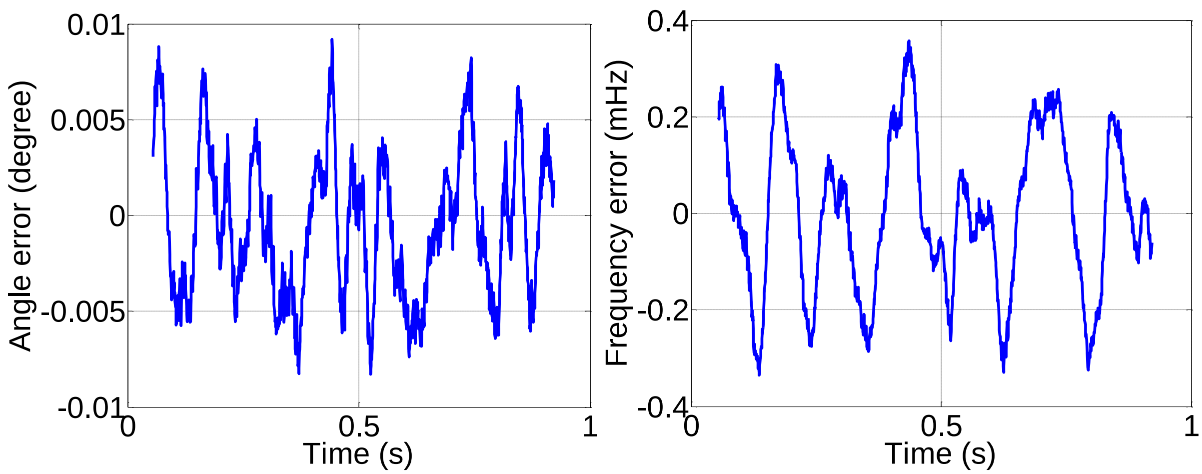

(a). Angle errors (b). Frequency errors

Figure 7.13 Synchrophasor measurement errors in field application

7.5.3 Harmonics measurement

Harmonics are computed by the noise analysis function as well. Generally, it is challenging to measure the harmonics accurately when the power grid frequency deviates from nominal frequency (50Hz or 60Hz) due to spectrum leakage of DFT. Figure 7.14 shows the maximum harmonics measurement errors of 2nd to 15th order of harmonics when power grid frequency varies from 59.9 Hz to 60.1 Hz. We can see that the harmonics measurement errors of the UGA increase as harmonics order increases, and maximum error is about 0.7%, which is good enough for practical applications. However, it should be noticed that some error compensation method is necessary if higher order harmonics need to be measured as the estimation errors increase exponentially with the increase of harmonics order.

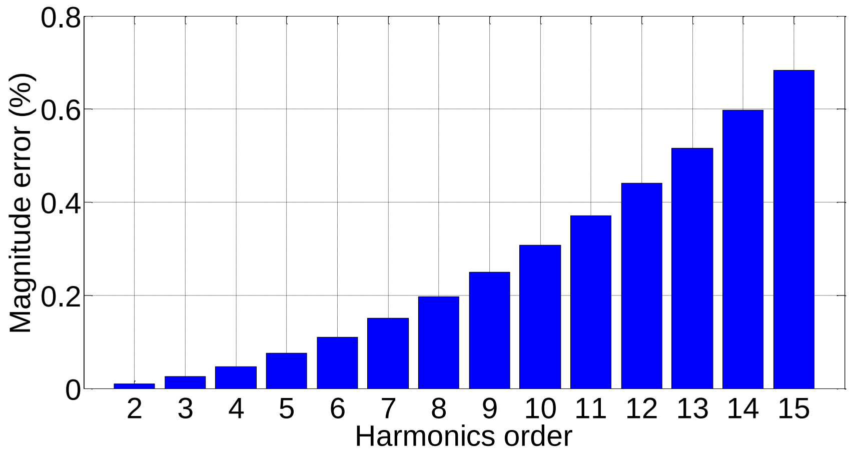

Figure 7.14 Harmonics measurement errors of the UGA

7.5.4 Voltage sag and swell detection

The Agilent power AC source is used to test the voltage sag and swell function. Figure 7.15 shows the voltage sag test results. In Figure 7.15 (a), the voltage was changed from 121 V to 111V, we can see that the voltage sag flags changed from 0xc0 to 0xff, which indicated the occurrence of voltage sag. Figure 7.15 (b) shows the flags when the voltage was changed from 111V to 121V, and we can see that the flags changed from 0xff to 0xc0. Similarly, Figure 7.16 shows the voltage swell test.

1	090514	155305	4	59.99999	59.99999	121.7480	2.8650	0.12	0xc0	0xc0	0xc0	0xc0
1	090514	155305	5	60.00001	60.00001	121.7414	2.8647	0.12	0xc0	0xc0	0xc0	0xc0
1	090514	155305	6	59.99999	59.99999	121.7348	2.8644	0.12	0xc0	0xc0	0xc0	0xc0
1	090514	155305	7	59.98663	59.98665	119.4160	2.8648	0.12	0xf0	0xc0	0xc0	0xc0
1	090514	155305	8	60.01153	60.01150	110.9350	2.8530	0.10	0xff	0xff	0xc0	0xc0
1	090514	155305	9	60.00178	60.00178	111.4696	2.8616	0.13	0xff	0xff	0xc0	0xc0

(a). Voltage changes from 121V to 111V

1	090514	155103	2	60.00001	60.00001	111.5378	3.2076	0.14	0xff	0xff	0xc0	0xc0
1	090514	155103	3	60.00000	60.00001	111.5312	3.2073	0.14	0xff	0xff	0xc0	0xc0
1	090514	155103	4	59.99585	59.99587	113.3088	3.2072	0.14	0xcf	0xff	0xc0	0xc0
1	090514	155103	5	60.00365	60.00364	121.2420	3.2045	0.16	0xc0	0xc0	0xc0	0xc0
1	090514	155103	6	60.00070	60.00070	121.7062	3.2062	0.13	0xc0	0xc0	0xc0	0xc0
1	090514	155103	7	60.00001	60.00001	121.7150	3.2064	0.12	0xc0	0xc0	0xc0	0xc0

(b). Voltage changes from 111V to 121V

Figure 7.15 Voltage sag test

1	090514	153327	4	60.00001	60.00001	121.7502	5.3874	0.13	0xc0	0xc0	0xc0	0xc0
1	090514	153327	5	60.00065	60.00065	121.7458	5.3871	0.13	0xc0	0xc0	0xc0	0xc0
1	090514	153327	6	59.99485	59.99483	125.9346	5.3883	0.12	0xc0	0xc0	0xff	0xf8
1	090514	153327	7	60.00450	60.00451	131.6590	5.3840	0.12	0xc0	0xc0	0xff	0xff
1	090514	153327	8	60.00030	60.00030	131.8328	5.3865	0.12	0xc0	0xc0	0xff	0xff

(a). Voltage changes from 121V to 131V

1	090514	153039	4	60.00000	60.00000	131.8702	5.8615	0.11	0xc0	0xc0	0xff	0xff
1	090514	153039	5	59.98896	59.98894	130.8296	5.8618	0.11	0xc0	0xc0	0xc1	0xff
1	090514	153039	6	60.00550	60.00550	121.5654	5.8526	0.10	0xc0	0xc0	0xc0	0xc0
1	090514	153039	7	60.00525	60.00525	121.5698	5.8570	0.12	0xc0	0xc0	0xc0	0xc0
1	090514	153039	8	60.00030	60.00030	121.7656	5.8599	0.12	0xc0	0xc0	0xc0	0xc0

(b). Voltage changes from 131V to 121V

Figure 7.16 Voltage swell test

7.6 Verification of the effect of noise on measurement accuracy

Taking the advantage of the UGA, the characteristics of the power grid voltage signals at distribution level can be studied, and the distortions can be extracted and used to study the measurement errors of synchrophasor at distribution level as discussed in 7.5.2. However, in practical applications, since there are no reference values for error analysis, it is difficult to verify the credibility of the measurement errors analysis results. In this section, an approach is proposed to measure the credibility of the measurement errors analysis results. The flowchart of the approach to evaluate the measurement errors analysis results is shown in Figure 7.17.

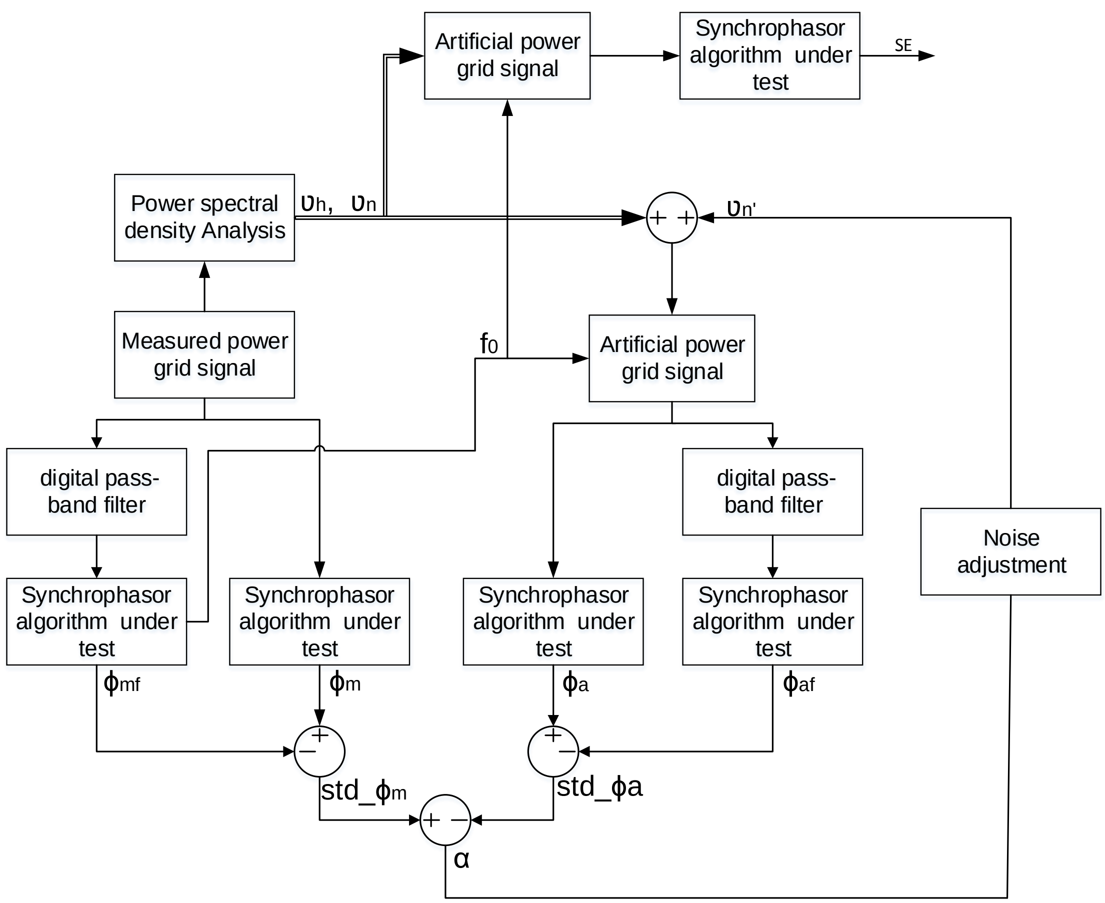

Figure 7.17 Flowchart of measurement errors evaluation

Power grid voltage signals at distribution level are sampled by the UGA, and modified periodogram is used to calculate the harmonics ʋh and noise ʋn of the voltage signal through power spectral density analysis. Meanwhile, the frequency of the voltage signal is estimated by the synchrophasor algorithm under test, named as f_0 in Figure 7.17. As a result, an artificial signal is generated with the estimated frequency f_0, harmonics υh, and noise υn, which is represented by the below equation

$$Sig_A = \cos(2\pi f_0 t) + \upsilon\mathrm{h} + \upsilon\mathrm{n} + \upsilon\mathrm{n}' \tag{7.12}$$

where Sig_A is the artificial signal, $\cos(2\pi f_0 t)$ is the fundamental frequency component of the artificial signal, υh is the harmonic components of the measured signal which has up to 48th order of harmonics, υn is the noise of the measured signal in dB, υn′ is the noise compensated by the noise adjustment block and will be explained later in this section.

Then the artificial signal is processed by two different ways. One of the ways is to process the signal by the synchrophasor measurement algorithm directly, and the phase angle $\emptyset_a$ can be estimated. The other way is to filter the signal by a narrow-band digital band-pass filter, which can greatly reduce the noise and harmonics. Then the filtered signal is processed by the synchrophasor measurement algorithm. As a result, phase angle, which is called $\emptyset_{af}$ can be estimated. Since the digital filter mainly functions as a filter to reduce the harmonics and noise, the angle difference between $\emptyset_a$ and $\emptyset_{af}$ is mainly caused by the noise and harmonics in the artificial signal.

Similarly, the phase angle of the measured power grid signal is estimated by the synchrophasor measurement algorithm. As a result, phase angle $\emptyset_{mf}$ and $\emptyset_m$ are obtained as shown in Figure 7.17.

Then the below equation is used to evaluate the difference between the artificial signal and measured signal,

$$\alpha = std\left(\emptyset_m - \emptyset_{mf}\right) - std\left(\emptyset_a - \emptyset_{af}\right) \tag{7.13}$$

where $std\left(\emptyset_m - \emptyset_{mf}\right)$ represents the standard deviation of $(\emptyset_m - \emptyset_{mf})$, and $std\left(\emptyset_a - \emptyset_{af}\right)$ represents the standard deviation of $\left(\emptyset_a - \emptyset_{af}\right)$.

Figure 7.18 shows the STD of angle difference regard to noise level. We can see that the STD has a linear relationship with noise. Therefore, if the artificial signal is the same as the measured power grid signal, then the α should be equal to 0. However, it is not possible to duplicate the measured signal exactly using a simple mathematical function. In this method, α is used as an index to represent the difference between measured voltage signal and the artificial signal in term of noise. According to Figure 7.18, a positive α indicates that the artificial signal has less noise than the measure signal, and a negative α indicates that the artificial signal has more noise than the measured signal. Therefore α can be used to adjust the amount of noise compensated for the generation of the artificial signal, which is $\upsilon n'$ in Figure 7.17. α can approach to zero after several times of iterations, then we can claim the "equivalent noise" of the measured voltage signal is $(\upsilon n + \upsilon n')$.

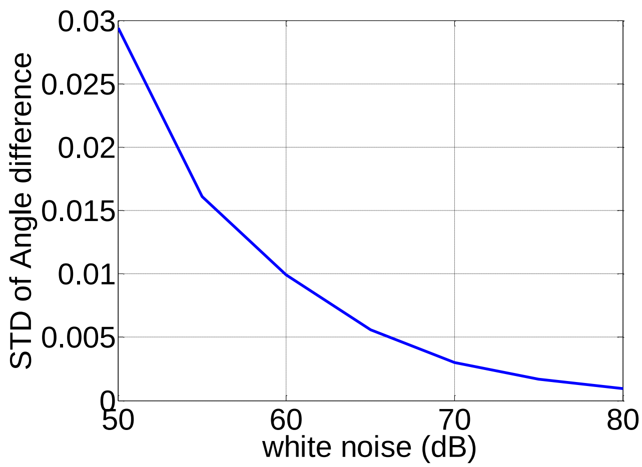

Figure 7.18 STD of angle difference

As a result, the difference between υn and $(\upsilon n + \upsilon n')$ can be used an index to evaluate the accuracy of artificial signal, which is

$$\gamma = \frac{\upsilon n'}{\upsilon n} \tag{7.14}$$

where υn is the noise of the measured signal calculated by "Power spectral density Analysis" in Figure 7.17, $\upsilon n'$ is the noise obtained from the "noise adjustment" block.

The credibility of the proposed analysis method in 7.5.2 increases as γ approaches to zero. If γ is zero, it means the method is perfect. Figure 7.19 shows the experimental result. In this test, the estimated SNR of the measured signal is 70dB, and the noise that make α to be zero is equal to 65dB. Therefore γ is equal to

$$\gamma = \frac{\upsilon n'}{\upsilon n} = \frac{-5}{70} = -0.0714$$

The test shows that "equivalent noise" of the measured signal is 65dB, which is quite close to the 70 dB SNR estimated by the noise analysis function of the UGA.

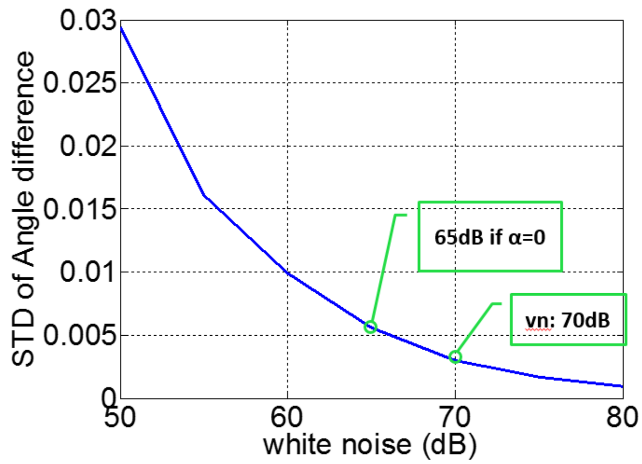

Figure 7.19 Experimental verification

Since the artificial signal model assumes that the measured power grid signal only consists of constant fundamental frequency component, white noise and harmonics, the reason that $\upsilon n'$ is not equal to zero can be explained by:

1) Because the true frequency of the measured power grid signal is unknown, an averaged and constant frequency value f_0 is used. However, the true frequency of the measured signal varies with time.
2) The noise used for generating the artificial signal is white noise. However, according to "Power spectral density Analysis" of the measured signal, the color of the noise of the measured signal is not white. There is more noise at lower frequency range.
3) Since the frequency of the measured signal varies with time, the frequency of the harmonic components will also vary.
4) The distortion of the measured signal may contain not only harmonics and noise, there may be some other interferences that cannot be observed by the power spectral density analysis method.

7.7 Conclusion

In this chapter, a concept of UGA that is a GPS time synchronized and real-time power grid monitoring device was proposed and a prototype was built in laboratory. A new synchronous sampling method was proposed and implemented in the UGA, and experimental results verified that the proposed method and new hardware can achieve high sampling accuracy, which far exceeds the IEEE PMU Standard. This feature can provide a potential to develop a highly accurate synchrophasor measurement device based on the UGA platform. Meanwhile, the UGA can also function as a power quality analyzer. It has harmonics measurement, voltage sag and swell detection function. Additionally, the noise analysis function of the UGA can analyze the power grid signal in frequency domain; hence the UGA can help analyze synchrophasor measurement errors in a real power grid environment. This function is also expected to provide guidance for designing a digital filer to improve synchrophasor measurement accuracy further in the future.

Chapter 8 Conclusions and Future Works

8.1 Conclusions

This dissertation covered a wide variety of research topics in the area of wide-area power grid monitoring, including timing reliability and measurement accuracy improvement of synchrophasor measurement, PMU testing system, as well as the development of a Universal Grid Analyzer that can function as a phasor measurement device as well as a power quality analyzer.

At the very beginning, this dissertation studied two alternative timing sources for PMUs and FDRs including eLoran and chip scale atomic clock (CSAC). Experimental results demonstrated that eLoran can provide accurate and reliable timing signal for PMUs and FDRs. Additionally, the testing of CSAC on FDRs demonstrated that CSAC can be a good backup for GPS for at least 24 hours. The integration of CSAC into GPS receiver is expected to improve the timing reliability of PMUs and FDRs.

Next, the measurement errors of FDRs were analyzed in terms of both hardware and measurement algorithm. Hardware error sources including GPS and ADC were analyzed. The ADC of the new FDR was upgraded with a 16-bit ADC to improve phasor measurement accuracy. Next, the measurement algorithm of the FDRs was evaluated under various steady-state and dynamic conditions according to the PMU Standard. The testing results revealed that the FDR measurement algorithm has some room for improvement under harmonic conditions at the presence of frequency offset, dynamic conditions as well as noise condition for phase angle measurement.

Therefore, two new phasor estimation algorithms were proposed to improve the phasor measurement accuracy. The first algorithm is based on phasor estimation model in the PMU Standard. The algorithm consists of six modules to measure the phasor and frequency accurately under various conditions in the PMU Standard as well as real power grid condition at the distribution level. The second algorithm is a signal model based method. The algorithm models the different reference signals in the PMU Standard, and the testing results verified that the algorithm has good measurement accuracy compared to the FDR algorithm.

After that, the PMU testing system at UKT/ORNL was introduced. It was found that the time delay of the signal generated by PSS caused the errors of the PMU testing system. As a result, a calibration method was proposed in this dissertation to compensate the delay. The new testing results can match the results from NIST, and therefore verified the performance of the proposed calibration method. Additionally, according to the testing results, the current PMU Standard is too strict for current commercial PMU to pass, particularly for frequency and ROCOF measurements.

At last, the development of a prototype UGA was presented. Taking advantage of the proposed adaptive synchronous sampling method and high-precision ADC, experimental results demonstrated that the prototype UGA has better measurement accuracy compared to GenII-FDR and commercial PMUs. The UGA also has power quality analyzer's functions including harmonics measurement, voltage sag and swell detection. Moreover, the noise analysis function of the prototype UGA allows the analysis of phasor measurement errors in a real power grid environment. Further, a method that can verify the analysis results of measurement errors was presented at the end.

8.2 Future works

Potential further work may include:

1) For the timing reliability of PMUs and FDRs. The eLoran system needs to be tested in a longer time to demonstrate its reliability compared to GPS. For CSAC, how to coordinate the operation between GPS and CSAC is desirable since CSAC still drifts with time.
2) As for phasor measurement accuracy improvement, better understanding of the noise pattern and fundamental frequency variation pattern can contribute to the development of a more practical phasor measurement algorithm.
3) For the Universal Grid Analyzer part, more measurement functions such as voltage flicker can be developed for better characterizing the power grid quality. Moreover, the phasor measurement accuracy is expected to be further improved by increasing sampling rate and applying more advanced digital filters. The analysis of phasor estimation errors at the distribution level can be further improved by considering colorful noise and variable frequency of the fundamental frequency and harmonic components.

List of References

[1] A.G. Phadke, "Synchronized phasor measurements in power systems," IEEE Computer Applications in Power, vol. 6, no. 2, pp. 10-15, Apr. 1993.

[2] B. Qiu, L. Chen, V. Centeno, X. Dong, and Y. Liu, "Internet based Frequency Monitoring Network (FNET)," in Proc. 2001 IEEE Power Engineering Society Winter Meeting, pp. 1166-1171.

[3] Y. Zhang, P. Markham, T. Xia, L. Chen, Y. Ye, Z. Wu, Z. Yuan, L. Wang, J. Bank, J. Burgett, R. W. Conners, and Y. Liu, "Wide-Area Frequency Monitoring Network (FNET) Architecture and Applications," IEEE Transactions on Smart Grid, vol. 1, no. 2, pp. 159-167, 2010.

[4] Z. Zhong, C. Xu, B.J. Billian, L. Zhang, S.S. Tsai, R.W. Conners, et al. "Power system Frequency Monitoring Network (FNET) implementation," IEEE Trans. Power Systems, vol. 20, no. 4, pp. 1914-1921, Nov. 2005.

[5] [Online]: http://fnetpublic.utk.edu/

[6] Jian Chen, “Accurate frequency estimation with phasor angle,” M.S. thesis, Dept. ECE. Eng., Virginia Tech., Blacksburg, VA, 1994.

[7] T. Xia, and Y. Liu, "Single-phase phase angle measurements in electric power systems," IEEE Trans. Power System, vol. 25, no. 2, pp. 844-852, May 2010.

[8] T. Xia, H. Zhang, R. Gardner, J. Bank, J. Dong, J. Zuo, et al., "Wide-area frequency based event location estimation," in Proc. 2007 IEEE Power Engineering Society General Meeting, pp.1-7.

[9] M. Young, P. Markham, Y. Liu, "Advanced Power System Monitoring, Modeling, and Control Applications using FNET (Paper ID: 240, Invited Paper), the 16th IFAC Symposium on System Identification, (SYSID 2012)

[10] G. Zheng, Y. Liu, and G. Radman, "Wide area frequency based generation trip event location estimation," in 2012 IEEE Power and Energy Society General Meeting, 2012, pp. 1-6.

[11] Y. Zhang, L. Chen, Y. Ye, P. N. Markham, J. Bank, J. Dong, Z. Yuan, Z. Lin, and Y. Liu, "Visualization of wide area measurement information from the FNET system," Proc. IEEE Power Eng. Soc. Gen. Meeting, 2011, pp.1-8.

[12] Y. Ye, J. Dong, and Y. Liu, "Analysis of power system disturbances based on distribution-level phasor measurements," Proc. IEEE Power Eng. Soc. Gen. Meeting, 2011, pp. 1-7.

[13] Y. Ye, R. M. Gardner, and Y. Liu, "Oscillation analysis in Western Interconnection using distribution-level phasor measurements," Proc. IEEE Power Eng. Soc. Gen. Meeting, 2011, pp. 1-8.

[14] Y. Ye and Y. Liu, "Monitoring power system disturbances based on distribution-level phasor measurements," Proc. IEEE PES Innovative Smart Grid Technologies, 2012, pp. 1-8.

[15] J. Guo, Y. Liu et al, "Design and Implementation of Real-Time Off-Grid Detection Tool Based on FNET/GridEye" IEEE PES General Meeting, National Harbor, MD, July 2014

[16] Jiahui Guo, Ye Zhang, Yin Lei, Yilu Liu, Yanzhu Ye, "Events Associated Power System Oscillations Observation Based on Distribution-level Phasor Measurements", 2014 IEEE PES Transmission & Distribution Conference & Exposition, April 15-17, 2014 in Chicago, IL.

[17] G. Zhang, S. Lee, R. Carroll, J. Zuo, L. Beard, and Y. Liu, "Wide area power system visualization using real-time synchrophasor measurements," in 2010 IEEE Power and Energy Society General Meeting, 2010, pp. 1-7.

[18] T. Xia, Y. Zhang, L. Chen, Z. Yuan, P. N. Markham, Y. Ye, and Y. Liu, "Phase angle-based power system inter-area oscillation detection and modal analysis," Euro. Trans. Electr. Power, vol. 21, no. 4, pp. 1629-1639, 2011.

[19] Bank, J.N.; Omitaomu, O.A.; Fernandez, S.J.; Liu, Y.; "Extraction and visualization of power system interarea oscillatory modes," Power and Energy Society General Meeting, 2010 IEEE.

[20] Y. Ye, L. Chen, Y. Zhang, R. M. Gardner, and Y. Liu, "FNET observations of low frequency oscillations in the eastern interconnection and their correlation with system events," Proc. IEEE Power Eng. Soc. Gen. Meeting, 2011, pp. 1-8.

[21] W. L, R.M. Gardner, J. Dong, L. Wang; T. Xia; Y. Zhang, et al., "Wide area synchronized measurements and inter-area oscillation study," in Proc. 2009 IEEE Power Systems Conference and Exposition, pp.1-8.

[22] R.M. Gardener, Z. Zhong, Y. Liu, "Location determination of power system disturbances based on frequency responses of the system," U.S. Patent 7 519 454, Apr. 14, 2009.

[23] J.N. Bank, R.M. Gardner, S.S. Tsai, S.K. Kyung, Y. Liu, "Visualization of Wide-Area Frequency Measurement Information," in Proc. 2007 IEEE Power Engineering Society General Meeting, pp. 1-8.

[24] J.K. Wang, R.M. Gardner, Y. Liu, "Analysis of system oscillations using wide-area measurements," in Proc. 2006 IEEE Power Engineering Society General Meeting, pp. 1-6.

[25] [Online]: http://www.ursanav.com/capabilities/position-navigation-timing

[26] IEEE Standard for Synchrophasors Measurement for Power Systems, IEEE Std. C37.118.1-2011, Dec. 2011. (Revision of IEEE Std. C37.118-2005)

[27] IEEE Standard for Synchrophasor Measurements for Power Systems -- Amendment 1: Modification of Selected Performance Requirements, IEEE Std. C37.118.1a-2014, Apr. 2014.

[28] [Online]: http://www.ursanav.com/sites/default/files/pdfs/lf-pnt/UN-152A.pdf

[29] [Online]: http://www.microsemi.com/products/timing-synchronization-systems/embedded-timing-solutions/components/sa-45s-chip-scale-atomic-clock#documents

[30] [Online]: SA.45s Chip-Scale Atomic Clock User's Guide: http://www.microsemi.com/products/timing-synchronization-systems/embedded-timing-solutions/components/sa-45s-chip-scale-atomic-clock#documents.

[31] [Online]: Analog AD7663 datasheet: http://www.analog.com/media/en/technical-documentation/data-sheets/AD7663.pdf

[32] [Online]: Analog AD780 datasheet: http://www.analog.com/media/en/technical-documentation/data-sheets/AD780.pdf

[33] [Online]: Texas Instruments TMS320C6713: http://www.ti.com/product/tms320c6713

[34] Zhang, Ye, "Frequency Monitoring Network (FNET) Data Center Development and Data Analysis. " PhD diss., University of Tennessee, 2014.

[35] T. Xia, "Frequency Monitoring Network (FNET) algorithm improvements and application development," Ph.D. dissertation, Dept. ECE. Eng., Virginia Tech., Blacksburg, 2009.

[36] J. Warichet, T. Sezi, and J.C. Maun, "Considerations about synchrophasors measurement in dynamic system conditions," Int. J. Elect. Power & Energy Syst., vol. 31, no. 9, pp. 452-464, Oct. 2009.

[37] A. Phadke, and B. Kasztenny, "Synchronized phasor and frequency measurement under transient conditions, " IEEE Trans. Power Del., vol. 24, no. 1, pp. 89-95, Jan. 2009.

[38] D. Macii, D. Petri, and A. Zorat, "Accuracy analysis and enhancement of DFT-based synchrophasor estimators in off-nominal conditions," IEEE Trans. Instrum. Meas., vol.61, no. 10, pp. 2653-2664, Oct. 2012.

[39] I. Kamwa, A.K. Pradhan, and G. Joos, "Adaptive phasor and frequency-tracking schemes for wide-area protection and control," IEEE Trans. Power Del., vol. 26, no. 2, pp. 1-10, Apr. 2011.

[40] I. Kamwa, S.R. Samantaray, and G. Joos, "Wide frequency range adaptive phasor and frequency PMU algorithms," IEEE Trans. Smart Grid, vol. PP, no. 99, pp.1-11, Aug. 2013.

[41] W. Premerlani, B. Kasztenny, and M. Adamiak, "Development and implementation of a synchrophasor estimator capable of measurements under dynamic conditions, " IEEE Trans. Power Del., vol. 23, no. 1, pp. 109-123, Jan. 2008.

[42] I. Kamwa, S.R. Samantaray, and G. Joos, "Compliance analysis of PMU algorithms and devices for wide-area stabilizing control of large power systems," IEEE Trans. Power Systems, vol. 28, no. 2, pp.1766-1778, May 2013.

[43] R. Mai, Z. He, L. Fu, B. Kirby, and Z. Bo, "A dynamic synchrophasor estimation algorithm for online application, " IEEE Trans. Power Del., vol. 25, no. 2, pp. 570-578, Apr. 2010.

[44] W. Wang, L. Liu, L. He, L. Zhan, H. Qi, and Y. Liu, "Highly Accurate Frequency Estimation for FNET," in Proc. IEEE 2013 Power and Energy Society General Meeting, pp.1-5.

[45] J.A. de la O Serna, "Dynamic phasor Estimates for power system oscillations," IEEE Trans. Instrum. Meas., vol. 56, no. 5, pp.1648-1657, Oct. 2007.

[46] J.A. de la O Serna, "Dynamic phasor estimates for power system oscillations and transient detection," in Proc. 2006 IEEE Power Engineering Society General Meeting, pp. 7.

[47] M. A. Platas-Garza, and J. A. de la O Serna, "Dynamic phasor and frequency estimates through maximally flat differentiators," IEEE Trans. Instrum. Meas., vol. 59, no. 7, pp. 1803-1811, Jul. 2010.

[48] P. Castello, C. Muscas, and P.A. Pegoraro, "Performance comparison of algorithms for synchrophasors measurements under dynamic conditions," in 2011 Applied Measurements for Power Systems Workshop, pp. 25-30, Sept. 2011.

[49] G. Barchi, D. Macii, and D. Petri, "Synchrophasor estimators accuracy: a comparative analysis," IEEE Trans. Instrum. Meas., vol. 62, no. 5, pp. 963-973, May 2013.

[50] A.J., Roscoe, I.F. Abdulhadi, G.M. Burt, "P and M Class Phasor Measurement Unit Algorithms Using Adaptive Cascaded Filters," IEEE Trans. Power Delivery, vol. 28, no. 3, pp. 1447-1459, Jul. 2013.

[51] D. Macii, G. Barchi, and D. Petri, "Design criteria of digital filters for synchrophasor estimation," in Proc. 2013 IEEE Instrumentation and Measurement Technology Conference, pp. 1579-1584, May 2013.

[52] A.J., Roscoe, I.F. Abdulhadi, and G.M. Burt, "P-Class Phasor Measurement Unit algorithms using adaptive filtering to enhance accuracy at off-nominal frequencies," in Proc. 2011 IEEE Smart Measurements for Future Grids Conference, pp. 51-58, Nov. 2011.

[53] A.J., Roscoe, I.F. Abdulhadi, and G.M. Burt, "Filters for M class Phasor Measurement Units," in Proc. 2012 IEEE Applied Measurements for Power Systems Workshop, pp.1-6, Sept. 2012.

[54] Allen Goldstein. (2014, Mar.). National Institute of Standards and Technology. Lessons learned from the NIST assessment of PMUs. [Online]. Available: https://www.naspi.org/meetings

[55] D. Whitehead and G. Zweigle, "System for Synchronous Sampling and Time-of-Day Clocking Using An Encoded Time Signal," U.S. Patent 20050041767, Feb. 24, 2005.

[56] J. Mei and T. Ma, "Synchronous sampling clock closed loop correcting method and system based on FPGA," CN Patent 103616814, Mar. 5, 2014.

[57] X. Li, G. Huang, et al., "Design of High Accuracy Synchronous Sampling Clock in Digital Substations,", Journals of Automation of Electric Power Systems, vol. 33, no. 1, pp. 61-65, Sep. 2009.

[58] IEC Standard for Testing and Measurement Techniques - Power quality measurement methods, IEC 61000-4-30 ed2.0, Oct. 2008.

Appendix

Appendix A

A. Derivation of filter coefficient E_i in (4.10)

Since N_1 is equal to 12, the first angle estimated by (9) is $\widetilde{\emptyset}(6)$. To calculate $\widetilde{\emptyset}(6)$, $\varphi(i)$ $(i = 1, \ldots, 12)$ are divided into four angle groups (m =1, 2, 3, 4) as shown in Fig. A1, then linear interpolation is used to estimate $\emptyset(6)$in each angle group, and the linear function is given by

$$\varphi(i) = \gamma_{j0} + \gamma_{j1}Q,\ j = 1, 2, 3, 4 \tag{A.1}$$

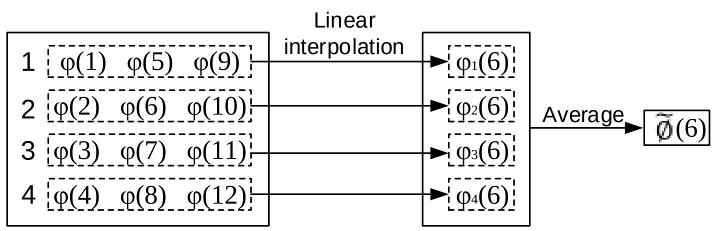

Fig. A1 Illustration of $\widetilde{\emptyset}(6)$ estimation using $\varphi(1)$ to $\varphi(12)$

where j represents the j-th angle group, j=1, 2, 3, 4; γ_{j0} and $\gamma_{j1}$is the coefficient of the linear function; For the three angles in each angle group, Q is equal to -1, 0, 1, respectively. Then we have

$$\begin{bmatrix} \varphi(j) \\ \varphi(j+4) \\ \varphi(j+8) \end{bmatrix} = \begin{bmatrix} 1 & -1 \\ 1 & 0 \\ 1 & 1 \end{bmatrix} \begin{bmatrix} \gamma_{j0} \\ \gamma_{j1} \end{bmatrix},\ j = 1, 2, 3, 4 \tag{A.2}$$

The estimation of γ_{i0} and γ_{i1} in least square terms is

$$\begin{bmatrix} \gamma_{j0} \\ \gamma_{j1} \end{bmatrix} = \left(\begin{bmatrix} 1 & -1 \\ 1 & 0 \\ 1 & 1 \end{bmatrix}' \begin{bmatrix} 1 & -1 \\ 1 & 0 \\ 1 & 1 \end{bmatrix} \right)^{-1} \begin{bmatrix} 1 & -1 \\ 1 & 0 \\ 1 & 1 \end{bmatrix}' \begin{bmatrix} \varphi(j) \\ \varphi(j+4) \\ \varphi(j+8) \end{bmatrix} \tag{A.3}$$

Then we obtain,

$$\begin{cases} \gamma_{j0} = \frac{(\varphi(j)+\varphi(j+4)+\varphi(j+8))}{3} \\ \gamma_{j1} = \frac{-\varphi(j)+\varphi(j+8)}{2} \end{cases},\ j = 1, 2, 3, 4 \tag{A.4}$$

Then $\emptyset(6)$ can be estimated as follows

$$\varphi_j(6) = \gamma_{j0} + \gamma_{j1}\left(\frac{1}{2} - \frac{j}{4}\right),\ j = 1, 2, 3, 4 \tag{A.5}$$

Next, $\varphi_j(6)$ $(j = 1, 2, 3, 4)$ are averaged to estimate $\emptyset(6)$ further,

$$\widetilde{\emptyset}(6) = \frac{\sum_{j=1}^{4} \varphi_j(6)}{4} = \frac{\sum_{j=1}^{4} r_{j0} + \sum_{j=1}^{4} r_{j1}(\frac{1}{2} - \frac{j}{4})}{4} \tag{A.6}$$

Substitute (A.4) to (A.6), we can obtain the coefficient of the filter in (9),

$$E_i = \{-\frac{1}{24}, \frac{1}{12}, \frac{5}{24}, \frac{8}{24}, \frac{1}{12}, \frac{1}{12}, \frac{1}{12}, \frac{1}{12}, \frac{5}{24}, \frac{1}{12}, -\frac{1}{24}, -\frac{4}{24}\} \tag{A.7}$$

B. Derivation of filter coefficient F_i in (4.13)

Similar as derivation of filter coefficient E_i, $\widetilde{\emptyset}(k)$, $\widetilde{\emptyset}(k + 4)$, $\widetilde{\emptyset}(k + 8)$ are interpolated by a linear function,

$$\begin{bmatrix} \widetilde{\emptyset}(k) \\ \widetilde{\emptyset}(k+4) \\ \widetilde{\emptyset}(k+8) \end{bmatrix} = \begin{bmatrix} 1 & -1 \\ 1 & 0 \\ 1 & 1 \end{bmatrix} \begin{bmatrix} \tilde{\beta}_{k0} \\ \tilde{\beta}_{k1} \end{bmatrix} \tag{B.1}$$

where $\tilde{\beta}_{k0}$ and $\tilde{\beta}_{k1}$is the coefficient of the linear function.

Meanwhile,$\emptyset(k)$, $\emptyset(k + 4)$, and$\emptyset(k + 8)$ can also be interpolated by linear function,

$$\begin{bmatrix} \emptyset(k) \\ \emptyset(k+4) \\ \emptyset(k+8) \end{bmatrix} = \begin{bmatrix} 1 & -1 \\ 1 & 0 \\ 1 & 1 \end{bmatrix} \begin{bmatrix} \beta_{k0} \\ \beta_{k1} \end{bmatrix} \tag{B.2}$$

The estimation of $\tilde{\beta}_{k0}$ and β_{k0} in least square terms is,

$$\tilde{\beta}_{k0} = \frac{(\widetilde{\emptyset}(k) + \widetilde{\emptyset}(k+4) + \widetilde{\emptyset}(k+8))}{3} \tag{B.3}$$

$$\beta_{k0} = \frac{(\emptyset(k) + \emptyset(k+4) + \emptyset(k+8))}{3} \tag{B.4}$$

Assuming angles vary linearly with time, we have

$$\beta_{k0} = \frac{(\emptyset(k) + \emptyset(k+4) + \emptyset(k+8))}{3} = \emptyset(k+4) \tag{B.5}$$

$$\tilde{\beta}_{k0} - \beta_{k0} = \frac{\left(\widetilde{\emptyset}(k) + \widetilde{\emptyset}(k+4) + \widetilde{\emptyset}(k+8)\right)}{3} - \emptyset(k+4) \tag{B.6}$$

According to (B.3), (B.4), and (4.11), we obtain

$$\tilde{\beta}_{k0} - \beta_{k0} = \frac{\left(\widetilde{\emptyset}(k) + \widetilde{\emptyset}(k+4) + \widetilde{\emptyset}(k+8)\right)}{3} - \frac{\left(\emptyset(k) + \emptyset(k+4) + \emptyset(k+8)\right)}{3} = \frac{\varepsilon(k) + \varepsilon(k+4) + \varepsilon(k+8)}{3} \tag{B.7}$$

According to (4.12), and assuming the frequency of the errors is equal to $(2i+1)f_0$, we further obtain

$$\tilde{\beta}_{k0} - \beta_{k0} = \frac{\varepsilon(k)+\varepsilon(k+4)+\varepsilon(k+8)}{3} = -\frac{\varepsilon(k+4)}{3} = -\frac{\tilde{\emptyset}(k+4)-\emptyset(k+4)}{3} \tag{B.8}$$

Solving simultaneous (B.6) and (B.8), we obtain

$$\frac{\left(\tilde{\emptyset}(k)+\tilde{\emptyset}(k+4)+\tilde{\emptyset}(k+8)\right)}{3} - \emptyset(k+4) = -\frac{\tilde{\emptyset}(k+4)-\emptyset(k+4)}{3} \tag{B.9}$$

Then, we obtain,

$$\emptyset(k+4) = \frac{\tilde{\emptyset}(k)+2\tilde{\emptyset}(k+4)+\tilde{\emptyset}(k+8)}{4} \tag{B.10}$$

As a result, the coefficient F_i in (4.13) is

$$F_i = \{\frac{1}{4}, \frac{2}{4}, \frac{1}{4}\} \tag{B.11}$$

Appendix B

```
#server program to receive UGA data
import socket
import sys

HOST = None

# UGA port
PORT = 9999

s = None

for res in socket.getaddrinfo(HOST, PORT, socket.AF_UNSPEC,
                              socket.SOCK_STREAM, 0, socket.AI_PASSIVE):

    af, socktype, proto, canonname, sa = res

    try:
        s = socket.socket(af, socktype, proto)
    except socket.error as msg:
        s = None
        continue
    try:
        s.bind(sa)
```

```
        s.listen(1)
    except socket.error as msg:
        s.close()
        s = None
        continue

    break

if s is None:
    print 'could not open socket'
    sys.exit(1)

conn, addr = s.accept()
print 'Connected by', addr

build = False

frame = ''
n = 0
nmax = 30

file_obj=open('UGA_data.txt','w')
while n < nmax:
```

```
    data = conn.recv(80)
    print data
    if not data: break

    ba = bytearray(data)
    for loop, byte in enumerate(ba):
        if byte == 0:
            print frame
            file_obj.write(frame)
            file_obj.write('\n')
            sys.stdout.flush()
        elif byte == 1:
            frame = ''
        else:
            if byte >191 & byte<256:
                frame=frame+hex(ord(data[loop]))
                frame=frame+' '
            else:
                frame += data[loop]
    n += 1
conn.close()
s.close()

file_obj.close()
```

Vita

Lingwei Zhan received his B.S. and M.S. in electrical engineering from Tongji University in 2008 and 2011, respectively. He started his Ph. D study at the University of Tennessee, Knoxville, in August 2011 and his research interests include wide-area power system monitoring, PMUs, synchrophasor measurement, power quality, digital signal processing, embedded system, HVDC, FACTs, renewable energy, application of power electronics in power systems.